

METHODS OF ASTROCHEMICAL MODELING: A MULTIDIMENSIONAL APPROACH

Dominique Maurice Maffucci

Albuquerque, New Mexico

B.S. Chemistry, University of New Mexico, 2014
B.A. Physics & Astrophysics, University of New Mexico, 2014

A Dissertation Presented to the
Graduate Faculty of the
University of Virginia
in Candidacy for the Degree of
Doctor of Philosophy

Department of Chemistry

University of Virginia
December 2019

Committee Members:

Eric Herbst
Robin Garrod
Brooks Pate
Remy Indebetow

© Copyright by
Dominique Maurice Maffucci
All rights reserved
December 17, 2019

ABSTRACT

Astrochemical kinetic models simulate the time-dependent chemical evolution of astrophysical environments by integrating a system of coupled, nonlinear differential rate law equations that describe the chemical reactions of a given molecular constituency. A general modeling method has been developed that varies the free parameters in the chemical model to generate grids of chemical structure that reveal for each species sensitivities to the model free parameters. Additionally, the general model takes as input functional representations of free parameters in the chemical kinetic model to generate a time-dependent chemical structure for systems of arbitrary geometry. Using a three-phase rate equation approach that includes species in the gas phase, on dust grains, and within ice mantles that develop on the grains, we model the chemical evolution for dark molecular cloud conditions observed in the Taurus Molecular Cloud 1 (TMC-1) and for the diffuse and translucent clouds observed toward Sagittarius B2 (Sgr B2). Several methods of fit are compared to determine the extent of the validity of agreement between observed and modeled relative molecular abundances using each method, and server tools have been developed to visualize and analyze the large datasets produced using our method in real time. Finally, the temperature-dependent reaction rate coefficients have been calculated for reactions involving sulfur and chlorine containing species likely to be present in the Venusian atmosphere, and the Arrhenius-Kooij parameters for a large temperature range $T = 10 - 800$ K have been optimized for integration into existing chemical networks.

ACKNOWLEDGEMENTS

During the Fall of 2013, the trajectory of my future was uncertain. Having enjoyed equally my studies of chemistry and astrophysics, I was torn regarding which endeavor I should pursue further as I looked for programs that suited my background and interests. To my surprise, I discovered a discipline which would become the primary focus of the next several years completeing this dissertation in astrochemistry.

The work contained in this document would not have been possible without the investment of a community of individuals spanning nearly three decades and multiple countries. To Hua Guo and John Grey at the University of New Mexico, thank you for introducing me to physical chemistry and providing the classes that would serve as a foundation for my doctoral work. To Sushilla Knottenbelt, thank you for being a great mentor in our teaching family and for your continued support. To Amy Gallagher, thank you for being an inspiring and motivating lab partner. To Ugo Hincelin, thank you for teaching me how to use our chemical model, and to Romane Le Gal, thank you for the reaction network that has been used in my work and for the encouragement, support, and validation. To Kinsuk Acharrya, thank you for checking my first models and for taking an interest in my work, and to Kotomi Taniguchi, thank you for including me in your work while you were a member of the group. To Trey Wenger, thank you for facilitating the development of the grid model script suite in my early days at UVA and for showing me how to code with style. To my committee, Robin Garrod, Brooks Pate, and Remy Indebetow, thank you for your guidance and for your attention to this document so that it can achieve its greatest form. To David Woon, thank you for allowing me to work in collaboration with you on a project that differed from yet complimented my primary research efforts. To Eric Herbst, thank you for taking a risk and granting me the opportunity to continue to follow my dream studying the heavens, for laying the groundwork for and continuing to cultivate our research community, and for your immense patience over the last five years.

Although the individual's journey may seem isolating, it is because of great friendship that I am reminded of the power of camaraderie and the fallacy of separation. To all of my friends, thank you for the late nights, the violent laughter, the intrepid debates, and for guided me back to myself when I lost my way in the darkness, the light, and the aether. I would like to extend a special thank you to Sommer Hen-

derson for your unique companionship and for traveling from there (Albuquerque) to here (Charlottesville) and back again and to Thomas Romano, though he is no longer with us, with whom I shared an uncanny familiarity, faith, and vision.

Finally, I would like to recognize my family. To my brother Andreas (Andre), my first friend, and Mary, the little sister I finally have, thank you for the unconditional love, support, and friendship you have provided me over the years. To my mother Patricia (Tish), I have not forgotten what you once told me when we stopped in a church to admire the stained glass while we were on a walk living in England. You said "in heaven, there are colors you can't even imagine," and although my eyes have remained largely the same in function, the curiosity for the mysterious and acceptance for the unknown, both of which you instilled in me, have come to fruition in my scientific endeavors. Thank you for nurturing my mind and spirit and for inspiring me to dream without limits.

Because of you, I can fly.

Dominique (Niko) Maffucci
Charlottesville, Virginia

for those who dream of heaven

TABLE OF CONTENTS

Abstract	iii
Acknowledgements	v
List of Figures	xii
List of Tables	xiv
1 Introduction and Summary	1
1.1 Interstellar Observations and Molecular Maps	1
1.2 An Astrochemical Kinetic Model	2
1.3 A General Multidimensional Model	4
1.3.1 Type I Grid Models and Variation of Parameters	4
1.3.2 Type II Grid Models and Parameter Mapping	4
1.3.3 Dynamic Models	5
1.4 An Astrochemical Toolbox	5
1.4.1 Current State of the Art	5
1.4.2 Visualization and Analysis	6
2 Dark Cloud Conditions: Taurus Molecular Cloud 1	9
2.1 Introduction	9
2.2 Chemical Model	11
2.2.1 Physical Conditions	11
2.2.2 Chemical Kinetics	13
2.2.3 Reaction Network and Rate Solver	14
2.2.4 Elemental Composition	14
2.2.5 Grid Models	15
2.3 Results and Discussion	17
2.3.1 General Characteristics of the Modeled Abundances	17
2.3.2 Grid Solutions and Agreement	18
2.3.3 Effect of New Mechanisms and Elemental Composition	24

2.3.4	Effect of Reactive Desorption and the Diffusion-binding Energy Ratio	25
2.4	Summary	25
2.5	Acknowledgments	26
3	Diffuse and Translucent Clouds: Sagittarius B2	47
3.1	Introduction	47
3.2	Chemical Model	50
3.2.1	Gas and Dust Temperature	50
3.2.2	Hydrogen Column and the Radiation Field Strength	51
3.2.3	Cosmic Ray Ionization	52
3.2.4	Elemental Composition	53
3.2.5	Reaction Network, Rate Solver, and Grid Models	53
3.2.6	Modeling Methods	54
3.3	Results and Discussion	55
3.3.1	Abundance Profiles	55
3.3.2	Model Agreement and Solution Spaces	63
3.3.3	Minimum Solution Spaces	64
3.3.4	Variation of Parameters	65
3.3.5	Outlier Detection	67
3.4	Conclusion	67
4	Sulfur and Chlorine Chemistry in the Venusian Atmosphere	103
4.1	Introduction	103
4.2	Chemical Dynamics	104
4.2.1	Exothermic Reactions with a Barrier	104
4.2.2	Barrierless Reactions	107
4.3	Results and Discussion	108
4.3.1	Partition Function Contributions and Competition	108
4.3.2	Temperature-dependent rate coefficients for reactions with barriers	109
4.3.3	Temperature-dependent rate coefficients for reactions without barriers	111
4.4	Conclusions	112
5	Conclusions and Future Work	123
5.1	Major Conclusions	123
5.2	Data Repositories	124
5.3	Future Endeavors	124

LIST OF FIGURES

1.1	An Example of a Type I Grid Model	7
1.2	Visualization Tool Example for Molecular Clouds Models	8
2.1	Time-dependent Abundances $\log X(t)$ and Observed Abundances $\log X_{\text{obs}}$ for Model A	27
2.2	Time-dependent Abundances $\log X(t)$ and Observed Abundances $\log X_{\text{obs}}$ for Model B	28
2.3	Time-dependent Abundances $\log X(t)$ and Observed Abundances $\log X_{\text{obs}}$ for Model C	29
2.4	Time-dependent Abundances $\log X(t)$ and Observed Abundances $\log X_{\text{obs}}$ for Model D	30
2.5	$\mathcal{A}(t)$ and $\sigma(t)$ for Group G and Models A, B, C, and D	31
2.6	$\mathcal{A}(t)$ and $\sigma(t)$ for Group C and Models A, B, C, and D	31
2.7	$\mathcal{A}(t)$ and $\sigma(t)$ for Group S and Models A, B, C, and D	32
3.1	Time-dependent Relative Molecular Abundances for Fiducial Models	70
3.2	Time-dependent Relative Molecular Abundances for Cyclopropenylidene	71
3.3	Time-dependent Relative Molecular Abundances for Sulfur Monoxide	72
3.4	Time-dependent Relative Molecular Abundances for Carbon Monosulfide	73
3.5	Time-dependent Relative Molecular Abundances for Dicarbon Monosulfide	74
3.6	Time-dependent Relative Molecular Abundances for the Thioformyl Cation	75
3.7	Time-dependent Relative Molecular Abundances for Thioformaldehyde	76
3.8	Time-dependent \mathcal{A} and r for Kinematic Component $v = -23$ km/s	77
3.9	Time-dependent \mathcal{A} and r for Kinematic Component $v = -40$ km/s	78
3.10	Time-dependent \mathcal{A} and r for Kinematic Component $v = -73$ km/s	79
3.11	Time-dependent \mathcal{A} and r for Kinematic Component $v = -106$ km/s	80
3.12	Minimum \mathcal{A}_{min} and $\mathcal{T}_{\mathcal{A}}$ for $v = -23$ km/s Cloud	81
3.13	Minimum \mathcal{A}_{min} and $\mathcal{T}_{\mathcal{A}}$ for $v = -40$ km/s Cloud	82
3.14	Minimum \mathcal{A}_{min} and $\mathcal{T}_{\mathcal{A}}$ for $v = -73$ km/s Cloud	83
3.15	Minimum \mathcal{A}_{min} and $\mathcal{T}_{\mathcal{A}}$ for $v = -106$ km/s Cloud	84

3.16	Maximum r_{\max} and \mathcal{T}_r for $v = -23$ km/s Cloud	85
3.17	Maximum r_{\max} and \mathcal{T}_r for $v = -40$ km/s Cloud	86
3.18	Maximum r_{\max} and \mathcal{T}_r for $v = -73$ km/s Cloud	87
3.19	Maximum r_{\max} and \mathcal{T}_r for $v = -106$ km/s Cloud	88
3.20	Heat Maps of $\mathcal{A}(p)$, $r(p)$, and Overlap $\mathcal{U}(p)$ at Fiducial Best Fit Time \mathcal{T}_A for $v = -23$ km/s Component	89
3.21	Heat Maps of $\mathcal{A}(p)$, $r(p)$, and Overlap $\mathcal{U}(p)$ at Fiducial Best Fit Time \mathcal{T}_A for $v = -40$ km/s Component	90
3.22	Heat Maps of $\mathcal{A}(p)$, $r(p)$, and Overlap $\mathcal{U}(p)$ at Fiducial Best Fit Time \mathcal{T}_A for $v = -73$ km/s Component	91
3.23	Heat Maps of $\mathcal{A}(p)$, $r(p)$, and Overlap $\mathcal{U}(p)$ at Fiducial Best Fit Time \mathcal{T}_A for $v = -106$ km/s Component	92
3.24	Scatter Plots of $\log(X_{\text{mod}}(t))$ and $\log(X_{\text{obs}}(v))$ at Fiducial Best Fit Time \mathcal{T} for $v = -23$ km/s	93
3.25	Scatter Plots of $\log(X_{\text{mod}}(t))$ and $\log(X_{\text{obs}}(v))$ at Fiducial Best Fit Time \mathcal{T} for $v = -40$ km/s	94
3.26	Scatter Plots of $\log(X_{\text{mod}}(t))$ and $\log(X_{\text{obs}}(v))$ at Fiducial Best Fit Time \mathcal{T} for $v = -40$ km/s	95
3.27	Scatter Plots of $\log(X_{\text{mod}}(t))$ and $\log(X_{\text{obs}}(v))$ at Fiducial Best Fit Time \mathcal{T} for $v = -106$ km/s	96
4.1	Partition Function Contributions, Exponential Factors, Tunneling Corrections, and TST Rate Coefficients	113
4.2	Transition-State-Theory Reaction Rate Coefficients and Arrhenius-Kooij Fits	114
4.3	Capture Theory Reaction Rate Coefficients and Arrhenius-Kooij Fits	115
5.1	Model of Disk around MWC 480	126
5.2	Gas temperatures for Disk Survey	126
5.3	Particle Densities for Disk Survey	127
5.4	Visual Extinctions for Disk Survey	127
5.5	Mass Densities for Disk Survey	128
5.6	Small Dust Grain Densities for Disk Survey	128
5.7	Large Dust Grain Densities for Disk Survey	129

LIST OF TABLES

2.1	Free Parameter Space for Dark Cloud Conditions	33
2.2	Fractional Elemental Abundances for Dark Molecular Clouds	34
2.3	Grid Model Key	35
2.4	Relative Molecular Abundances, Uncertainties, and Characters for TMC-1(CP)	36
2.5	Diagonal $\eta = \log(n) - \log(\zeta)$ Key	37
2.6	$\mathcal{A}_{\min}(\mathcal{T})$ and $\log(\mathcal{T})$ for Groups G, C, and S; Model A	38
2.7	$\mathcal{A}_{\min}(\mathcal{T})$ and $\log(\mathcal{T})$ for Groups G, C, and S; Model B	39
2.8	$\mathcal{A}_{\min}(\mathcal{T})$ and $\log(\mathcal{T})$ for Groups G, C, and S; Model C	40
2.9	$\mathcal{A}_{\min}(\mathcal{T})$ and $\log(\mathcal{T})$ for Groups G, C, and S; Model D	41
2.10	$\sigma_{\min}(\mathcal{T})$ and $\log(\mathcal{T})$ for Groups G, C, and S; Model A	42
2.11	$\sigma_{\min}(\mathcal{T})$ and $\log(\mathcal{T})$ for Groups G, C, and S; Model B	43
2.12	$\sigma_{\min}(\mathcal{T})$ and $\log(\mathcal{T})$ for Groups G, C, and S; Model C	44
2.13	$\sigma_{\min}(\mathcal{T})$ and $\log(\mathcal{T})$ for Groups G, C, and S; Model D	45
3.1	Quantities Calculated for Translucent Clouds toward Sgr B2	97
3.2	Free Parameter Space for Diffuse and Translucent Cloud Conditions	98
3.3	Fractional Elemental Abundances for Diffuse and Translucent Clouds	99
3.4	Relative Molecular Abundances, Uncertainties, and Characters for Sgr B2(N)	100
3.5	Best Fit Parameters for Absorbing Kinematic Components toward Sgr B2(N)	101
4.1	Arrhenius-Kooij Fit Parameters	116
4.2	Rotational Parameters	117
4.3	Reducible Representation of Nuclear Spin States of Molecules with Two $I = 3/2$ Atoms	118
4.4	Nuclear Spin State Degeneracies and Symmetry Considerations for Molecules with Two $I = 3/2$ Atoms	119
4.5	Degeneracies for Possible Nuclear Spin States of Even and Odd Symmetry for Molecules with Two $I = 3/2$ Chlorine Atoms	120
4.6	Vibrational Parameters	121

4.7 Ground State Electronic Properties 122

CHAPTER 1

INTRODUCTION AND SUMMARY

1.1 INTERSTELLAR OBSERVATIONS AND MOLECULAR MAPS

Broadband radio telescopes gather robust data sets that contain the absorption and emission line spectra for large molecular constituencies with unprecedentedly high spectral resolution (Herbst and van Dishoeck, 2009). These spectral line surveys have led to the detection of many molecular species in various astrophysical environments including dark molecular clouds (Soma et al., 2015; Gratier et al., 2016), diffuse and translucent clouds (Corby et al., 2015; Thiel et al., 2018; Corby et al., 2018; Thiel et al., 2019), massive young stellar objects (Taniguchi et al., 2019), and protoplanetary disks (Öberg et al., 2015; Cleeves et al., 2016). Interferometric observations offer similar spectral capabilities while providing spatial resolution allowing for molecular line images to be produced with a single dataset. Because multiple molecular species are observed along a single line of sight, it is necessary to develop a chemical model that accounts for gradients in molecular absorption and emission line intensities as well as for gradients in the physical conditions determined from observations for molecular species. Furthermore, an accurate chemical kinetic model is required to understand the chemical history of material as it is transformed through the star and planet formation processes to describe how prebiotic molecules and life emerged from a cosmic perspective. By developing a general chemical kinetic model, the question of molecular inheritance can be answered by creating a composite model constrained by observations that follows the chemical evolution of interstellar material across the stages of star and planet formation with observed molecular compositions serving as checkpoints along the way. In the following chapters, we model diffuse and translucent clouds as well as dark molecular clouds, which represent the ambient interstellar medium and the quiescent phase, respectively, where a rich molecular constituency is developed.

1.2 AN ASTROCHEMICAL KINETIC MODEL

Chemistry occurs in the gas between colliding atoms, molecules, photons, and cosmic rays as well as on interstellar dust grains as molecules settle onto the dust grain surfaces to develop mantles of ice when the number of deposited molecules becomes sufficiently large. The rate law of a single molecule in all chemical phases appears as a set of coupled, non-linear differential equations; explicitly, for species i in the gas (no subscript), on the grain surface (s), and in the ice mantle (m):

$$\begin{aligned}
 dn(i)/dt = & \sum_{j,l} k_{jl}n(j)n(l) + \sum_h k_h n(h) \\
 & + \sum_{u,v} k_{des}^{rxn} n_s(u)n_s(v) \\
 & + n_s(i) \left[k_{des}^{thermal} + k_{des}^{photo} + k_{des}^{CRP} \right] \\
 & - n(i) \left[\sum_p k_{ip}n(p) + \sum_q k_q + k_{acc} \right]
 \end{aligned} \tag{1.1}$$

$$\begin{aligned}
 dn_s(i)/dt = & \sum_{j,l} k_{jl}n_s(j)n_s(l) + \sum_h k_h n_s(h) \\
 & + k_{acc}n(i) + k_w n_m(i) - k_w n_s(i) \\
 & - n_s(i) \left[\sum_p k_{ip}n_s(p) + \sum_q k_q \right] \\
 & - n_s(i) \left[k_{des}^{thermal} + k_{des}^{photo} + k_{des}^{CRP} \right] \\
 & - \left. \frac{dn_s(i)}{dt} \right|_{s \rightarrow m} + \left. \frac{dn_m(i)}{dt} \right|_{m \rightarrow s}
 \end{aligned} \tag{1.2}$$

$$\begin{aligned}
dn_m(i)/dt = & \sum_{j,l} k_{jl} n_m(j) n_m(l) + \sum_h k_h n_s(h) \\
& + k_w n_s(i) - k_w n_m(i) \\
& - n_m(i) \left[\sum_p k_{ip} n_s(p) + \sum_q k_q \right] \\
& - \left. \frac{dn_m(i)}{dt} \right|_{m \rightarrow s} + \left. \frac{dn_s(i)}{dt} \right|_{s \rightarrow m} .
\end{aligned} \tag{1.3}$$

In each of equations 1.1, 1.2, and 1.3, n is the number density of a species with units of particles per cubic centimeter, and k is the rate coefficient for each type of reaction with units such that the units of each term contributing to the rate become particles per cubic centimeter per second. In equation 1.1, the rate law for gas phase species, the first and second terms represent two-body and one-body production mechanisms, respectively. The third term corresponds to the production of species i in the gas phase via non-thermal desorption from the dust grain surface, and the fourth, fifth, and sixth terms express thermal desorption, photodesorption, and cosmic-ray induced desorption of species i from the dust grain surface. The seventh term expresses two-body reactions involving species i that result in the destruction of species i , and the eighth term expresses the one-body analog, which includes photodestruction and cosmic ray ionization. The final term corresponds to accretion of gas-phase species onto the dust grains. The rate laws for surface and mantle species, equations 1.2 and 1.3, respectively, contain terms similar to those in the gas-phase rate law and additional terms to account for pair-wise swapping (terms 4 and 5 in the surface species rate law and terms 3 and 4 in the mantle species rate law) between molecules on the surface and in the ice mantle. The final two terms in the surface and mantle species rate laws account for the individual transfer between surface and mantle molecules. The chemical network we use for the models discussed in the following chapter is based off of the Kinetic Database for Astrochemistry (Wakelam et al., 2012, 2015) with updates for sulfur chemistry (Vidal et al., 2017), and the reaction rate coefficients for the contributing types of reactions can be found following <http://kida.astrophy.u-bordeaux.fr>.

The models in the following chapters utilize the *Nautilus* code (Ruaud et al., 2015; Ruaud, Wakelam, and Hersant, 2016), which has been used to model dark clouds (Maffucci et al., 2018), PDRs (Le Gal et al., 2017), prestellar cores (Hincelin et al., 2013), and protoplanetary disks (Wakelam et al., 2019), and the scripts suite developed in this work serves as an extension to the existing *Nautilus* code architecture.

1.3 A GENERAL MULTIDIMENSIONAL MODEL

Astrochemical kinetic models incorporate many processes to model accurately how matter transforms in astrophysical environments. Because of the complex nature of these models, there are many free parameters in the model including physical conditions such as temperature and density as well as chemical parameters like desorption energies of specific molecules on water ice and barrier heights between adjacent binding sites on dust grain surfaces. Each molecule has a specific chemistry governed by its own set of rate law equations, and the time-dependent abundance can be sensitive to the many free parameters that affect its rate laws. Furthermore, many reasonable combinations of free parameters differing only slightly from one another can produce abundances that well reproduce abundance observed in interstellar environments, so it is necessary to break these degeneracies and quantify the extent to which the variation of free parameters effects meaningful agreement between single and groups of observed and modeled relative molecular abundances. Finally, interferometric observations reveal gradients in molecular abundances and physical conditions traced by observed molecules, and each of these observations warrants a multidimensional model to accurately simulate the chemical evolution of the observed systems of compounds. To this end, two types of grid models have been developed for this dissertation and serve as the basis of the following chapters.

1.3.1 Type I Grid Models and Variation of Parameters

Type I grid models vary the free parameters in the chemical models to observe the effects different regimes of conditions have on the solutions to the rate law equations, the time-dependent relative molecular abundances (see Figure 1.1) for various interstellar systems. Small changes in the initial conditions have been known to effect large changes on the solutions to the rate law equations in models of interstellar molecular gas (Le Boulton et al., 1993, 1995; Boger and Sternberg, 2006), and Type I grid models help identify regions in the free-parameter space where bistabilities in the rate-law solutions may exist by revealing the ranges over which these differences emerge.

Grid models that vary the free parameters have also been coupled with models of radiative transfer to determine the degree of correlation between the abundances calculated from kinetic models and those determined from observed emission lines (Harada et al., 2019). Type I grid models have also been used to break the degeneracy observed in the solutions to the rate law equations by quantifying the extent to which combinations of free parameters effect abundances that are consistent with molecular line intensities observed in molecular gas (Viti, 2017).

1.3.2 Type II Grid Models and Parameter Mapping

The second type of grid models maps time-dependent relative molecular abundances to a vector (1D) or array (2D) combinations of free parameters that characterize gradients in molecular line intensities and physical conditions for various

interstellar objects. The simplest Type II grid is one in which only one free parameter is varied since the length of the 1D vector in this case would be arbitrary yet defined. A realistic example of the implementation of a simple Type II grid is the mapping of chemical kinetic models to the physical conditions determined using a PDR model like the MEUDON code, which successfully reproduces the abundances observed in the Horsehead Nebula (Le Gal et al., 2017). Type II grid models in 2D have been used to model the chemical evolution in active galactic nuclei (Harada, Thompson, and Herbst, 2013) and protoplanetary disks (Öberg et al., 2015; Cleeves et al., 2016).

1.3.3 Dynamic Models

Physical dynamics are incorporated into chemical kinetic models by integrating the differential rate law equations with physical conditions that change as a function of time. One exemplary dynamic model is that of a hot core in which the density of a dark cloud model increases simulating the collapse process of a cloud with sufficient gravity followed by a warm-up phase to emulate the heating that occurs after contraction, and these “warm-up” models have been shown to be effective at producing large organic species on the grains which then desorb to enrich the gas phase (Garrod and Herbst, 2006; Garrod, 2013; Garrod and Widicus Weaver, 2013). The *Nautilus* code has been used to show that the cyanopolyynes, which initially form in the gas phase, reach peak abundance after warm up and desorption further validating this approach for this class of molecules in massive young stellar objects (Taniguchi et al., 2019).

1.4 AN ASTROCHEMICAL TOOLBOX

1.4.1 Current State of the Art

The current state of the Type I grid models that are executed in our script suite include the free parameters describing the physical conditions of the gas and dust (gas temperature T_{gas} , density n , visual extinction A_V , cosmic ray ionization rate ζ , dust temperature T_{dust} , interstellar radiation field strength factor G_0 , x-ray ionization rate $\zeta_{\text{x-ray}}$), elemental composition (fractional elemental abundances of molecular hydrogen f_{H_2} , atomic hydrogen f_{H} , helium f_{He} , oxygen f_{O} , carbon f_{C} , nitrogen f_{N} , sulfur f_{S} , silicon f_{Si} , phosphorus f_{P} , sodium f_{Na} , magnesium f_{Mg} , chlorine f_{Cl} , and fluorine f_{F}), and chemical parameters (reactive desorption efficiency a and diffusion to binding energy ratios b). Additionally, other parameters in the model like well depths and the number of binding sites on grains can easily be added to the existing scripts to study the variation of these parameters. Type I grid models are used to model dark, diffuse, and translucent molecular clouds in Chapters 2 and 3.

The script to execute Type II grid models currently contains the same free-parameter space as the Type I grid model script, but instead of executing models for all combinations of ranges of free-parameter values like in Type I grids, models are

executed for grids of points onto which free parameter values are mapped. In the disk models discussed in the final chapter, each free parameter has a 2D representation, that is $\bar{p} = [p_1(r, z), p_2(r, z), \dots, p_n(r, z)]$ for the n free parameters in the model that correspond to the cylindrical coordinate system used to define the parametric equations describing the physical structure of the PPDs. While these models are restricted to two dimensions, the current script can run grid models for arbitrary geometries with free parameters defined by $\bar{p} = [p_1(x_1, x_2, \dots, x_m), p_2(x_1, x_2, \dots, x_m), \dots, p_n(x_1, x_2, \dots, x_m)]$ for an m dimensional model of n free parameters.

Dynamic models are also possible with the current architecture, though the free parameters that can be varied in time is limited by the rate solver code, in this case the *Nautilus* code, which currently reads gas temperature T_{gas} , density n , visual extinction A_V , and dust temperature T_{dust} as functions of time. Despite the limitations of the free parameter space, the script suite enables 4D models $\bar{p} = [T_{\text{gas}}(t, x_1, x_2, x_3), n(t, x_1, x_2, x_3), A_V(t, x_1, x_2, x_3), T_{\text{dust}}(t, x_1, x_2, x_3)]$ with higher dimensionality possible if desired. This method allows for direct coupling to physical models where the time-dependent physical structure is available so that the time-dependent chemical evolution can be applied as a post-processing technique, and this method has been used to trace the chemical evolution over magnetohydrodynamics simulations of collapsing molecular clouds and the disk formation processes (Hincelin et al., 2013, 2016).

1.4.2 Visualization and Analysis

The nature of the grid modeling routine described here produces large data sets that can be parsed and utilized by the astrochemical community at large. In order to facilitate the using the data produces in the models described in the following chapters, a tool has been developed using the Bokeh library in Python to visualize and analyze the data in real time. The abundance modules use input forms and slider tools so that users can select specific molecules and abundances as well as the combination of free parameters they wish to visualize in the grid models (see Figure 1.2), and users can also input observed abundances to calculate the root-mean-square log differences \mathcal{A} between the sets of observed and modeled abundances as a function of time. There are currently tools to visualize and analyze the data from the models described in Chapters 2 and 3, but the general structures can be updated to enable more detailed calculations for larger molecular constituencies, to allow data exportation, and to provide data for the reaction data as a function of time.

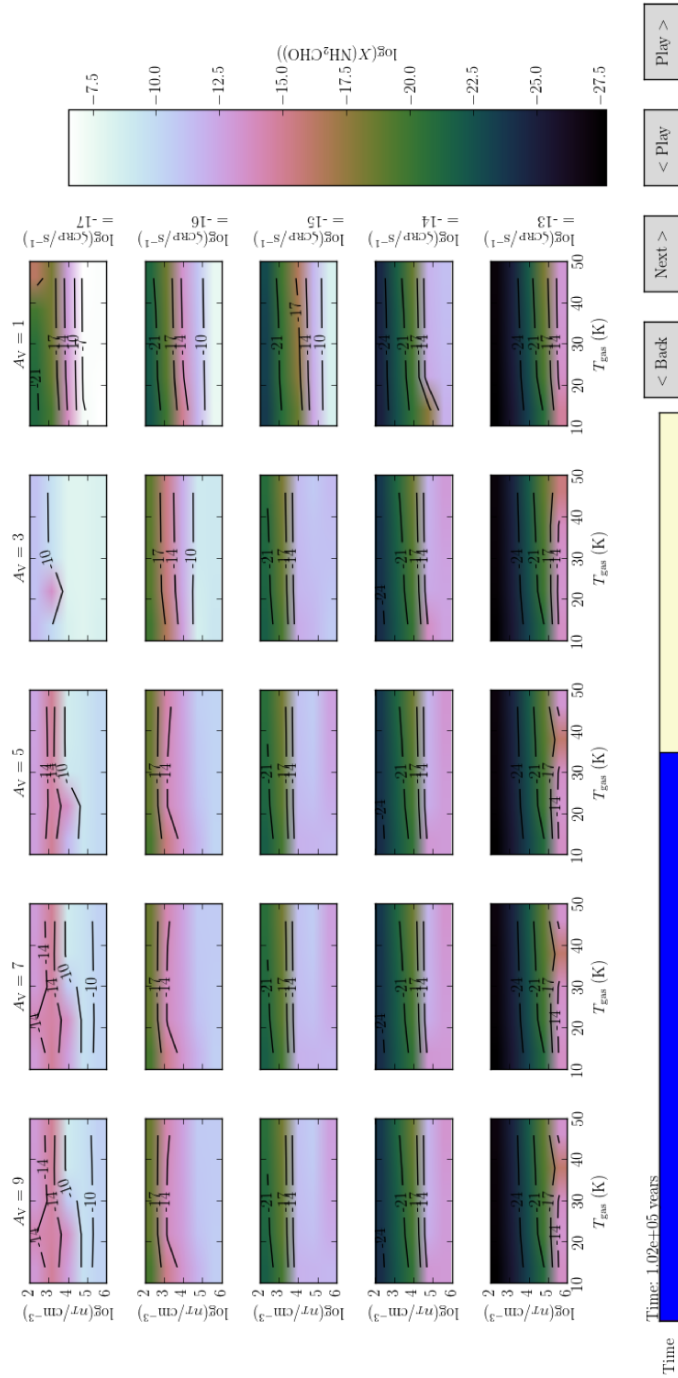


Figure 1.1: An example of a Type I grid model where the abundances of formamide NH_2CHO are shown over a large parameter space at a single time.

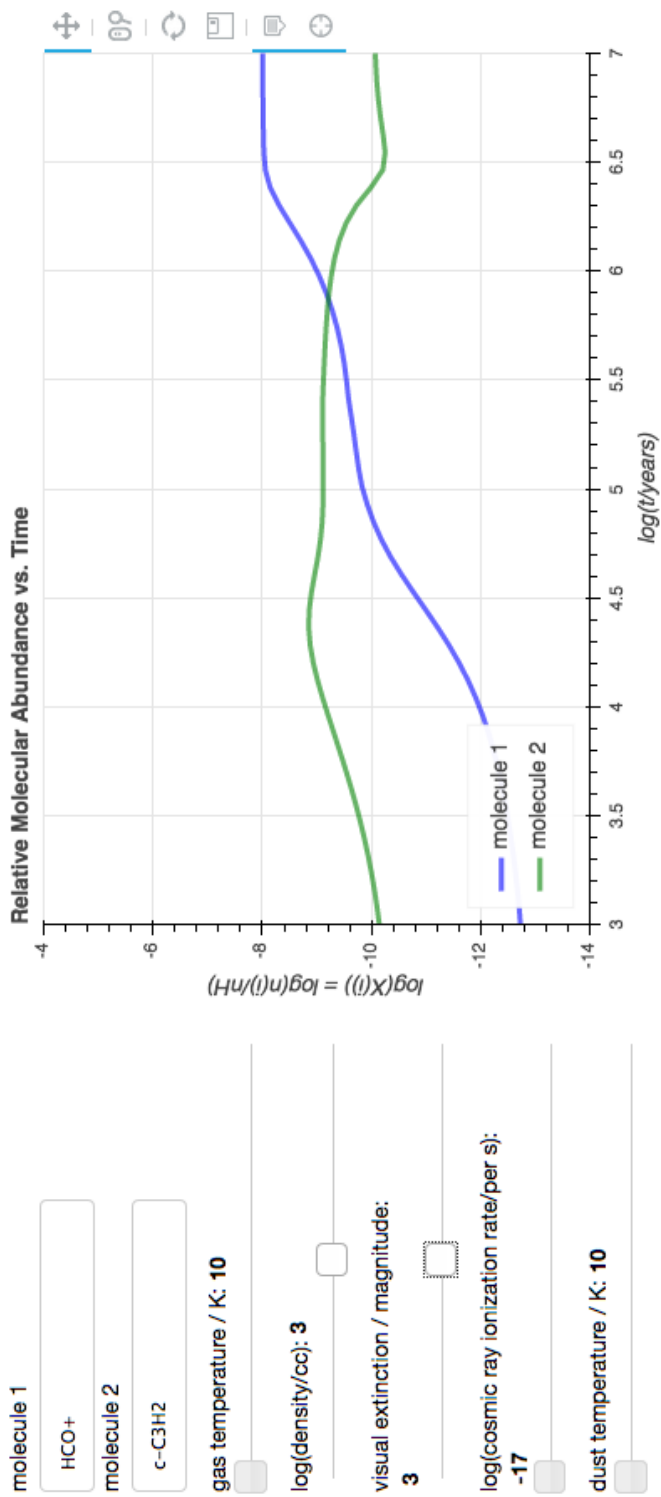


Figure 1.2: An example of the Visualization Tool with sliders and text box inputs to select data slices.

CHAPTER 2

DARK CLOUD CONDITIONS: TAURUS MOLECULAR CLOUD 1

The emission line spectra of cyanoacetylene and methanol reveal chemical and physical heterogeneity on very small (< 0.1 pc) scales toward the peak in cyanopolyne emission in the Taurus Molecular Cloud, TMC-1 (CP). We generate grids of homogeneous chemical models using a three-phase rate equation approach to obtain all time-dependent abundances spanning the physical conditions determined from molecular tracers of compact and extended regions of emission along this line of sight. Each time-dependent abundance is characterized by one of four features: a maximum/minimum, a monotonic increase/decrease, oscillatory behavior, or inertness. We similarly classify the time-dependent agreement between modeled and observed abundances by calculating both the root-mean-square logarithm difference and root-mean-square deviation between the modeled and observed abundances at every point in our grid models for three groups of molecules: (i) a composite group of all species present in both the observations and our chemical network G, (ii) the cyanopolyynes $C = \{HC_3N, HC_5N, HC_7N, HC_9N\}$, and (iii) the oxygen-containing organic species methanol and acetaldehyde $S = \{CH_3OH, CH_3CHO\}$. We discuss how the Bayesian uncertainties in the observed abundances constrain solutions within the grids of chemical models. The calculated best fit times at each grid point for each group are tabulated to reveal the minimum solution space of the grid models and the effects the Bayesian uncertainties have on the grid model solutions. The results of this approach separate the effect different physical conditions and model-free parameters have on reproducing accurately the abundances of different groups of observed molecular species.

2.1 INTRODUCTION

Emission line surveys of the dark molecular gas in the Taurus Molecular Cloud (TMC-1) reveal a large gas-phase molecular constituency containing ionic and neutral species, carbon chain molecules, and oxygen-containing organic species (Pratap et al.,

1997; Ohishi and Kaifu, 1998; Markwick, Millar, and Charnley, 2000; Markwick et al, 2005; Soma et al., 2015; Gratier et al., 2016). Along the ridge of molecular gas extending across $5' \times 15'$ of sky, emission maps obtained with the QUARRY focal plane array and FCRAO 14-m antennae ($\theta_{HPBW}^{14} = 59'' - 45''$ at 86 – 116 GHz) of several species (e.g. SO_2 , NH_3 , and HC_3N) show that the peaks in emission vary in location for each molecule suggesting the existence of chemical and physical heterogeneity on a scale of 0.04 - 0.03 pc at a distance $d = 140$ pc (Pratap et al., 1997; Markwick, Millar, and Charnley, 2000). Toward the peak in cyanopolyne emission, TMC-1 (CP), emission line maps using data collected by the Nobeyama 45-m ($\theta_{HPBW}^{45} = 20''$ at 96 GHz) show the spatial separation of the peaks in molecular emission intensities for methanol and carbon monosulfide, a tracer of the dense molecular clouds, to exist on a smaller scale of 0.01 pc across $150'' \times 150''$ of sky (Soma et al., 2015). The broadband spectral line survey toward TMC-1 (CP) conducted using the Nobeyama 45-m telescope from 8.8 to 50 GHz corresponding to $\theta_{HPBW} = 156'' - 27.5''$ and projected linear scale $s = 0.0187 - 0.106$ pc at a distance $d = 140$ pc provides a rich data set enabling the simultaneous analysis of the emission line spectra of several molecular components (Kaifu et al., 2004). Relative molecular abundances and a corresponding set of uncertainty values has been determined using these data and a Bayesian analysis of an LTE model of radiative transfer that both detects outlier emission lines with respect to assumed prior uncertainty distributions and determines the uncertainties in the calculated column densities (Gratier et al., 2016).

The line of sight toward TMC-1 (CP) has been well studied in several emission line surveys, and homogeneous chemical models with cold ($T = 10$ K), dark ($n \sim 10^5 \text{ cm}^{-3}$, $A_V \sim 10$) molecular cloud conditions reproduce large sets (> 50) of observed relative molecular abundances within an average factor of ten (Wakelam and Herbst, 2006; Garrod, Wakelam, and Herbst, 2007; Agúndez and Wakelam, 2013; Loison et al., 2014; Ruaud et al., 2015; Ruaud, Wakelam, and Hersant, 2016). Homogeneous chemical models worsen, however, for increasingly large sets of observed abundances because within a group of molecular species, the dominant production and destruction reaction mechanism sequences are unique to each molecule and vary in time. For example, species with large energies of desorption or lacking efficient gas-phase formation mechanisms (e.g. methanol, CH_3OH) require additional mechanisms to gas-phase reactions, such as grain-surface processes, to reproduce the observed gas phase abundances in homogeneous models of dark cloud conditions (Garrod, Wakelam, and Herbst, 2007; Vasyunin and Herbst, 2013; Ruaud et al., 2015). With additional gas-grain processes like the Eley-Rideal and van der Waals complex-induced reaction mechanisms (Ruaud et al., 2015), nonthermal desorption mechanisms like that due to the exothermicity of surface reactions (Garrod, Wakelam, and Herbst, 2007; Minissale et al., 2016) enrich the cold, dense gas with large amounts of oxygen-containing organic species methanol and acetaldehyde, so chemical models that incorporate these new mechanisms should benchmark the effects of their addition to the chemical network against both observed molecular abundances and existing chemical models of

cold, dark cloud conditions.

Because different chemical components appear to have dissimilar physical conditions along the line of sight to TMC-1 (CP) and because molecules are sensitive both to grain and ice surface processes and non-thermal desorption, we compute grids of homogeneous chemical models over ranges of free parameters such as the physical conditions density n and cosmic-ray ionization rate ζ as well as the reactive-desorption efficiency a and the diffusion-binding energy ratio b , which control the grain-surface reaction mechanisms. Using two elemental compositions for models with and without activated Eley Rideal and van der Waals complex reaction mechanisms, we create four distinct grid models to reveal the effects these additional parameters have on the model of the time-dependent chemical structure of TMC-1 (CP). Next, we quantify the agreement between each model and sets of observed abundances toward TMC-1 (CP) by calculating the root-mean-square logarithm difference between the observed and modeled abundances (Wakelam and Herbst, 2006; Hincelin et al., 2011; Vidal et al., 2017) at every time and for every combination of free parameters for three groups of molecular abundances: a composite Group G = {NH₃, CH₃OH, *c*-C₃H, *l*-C₃H, *l*-C₃H₂, *c*-C₃H₂, CH₃CCH, H₂CCN, CH₃CN, H₂CCO, CH₃CHO, HCS⁺, H₂CS, C₄H₂, C₃N, HCCNC, C₃O, HC₃NH⁺, CH₂CHCN, C₅H, CH₃C₄H, CH₃C₃N, C₃S, C₆H, HC₃N, HC₅N, HC₇N, HC₉N} of all molecules contained in both the latest benchmark chemical composition of TMC-1 (Gratier et al., 2016) and in our chemical network, Group C = {HC₃N, HC₅N, HC₇N, HC₉N} of the four smallest cyanopolyynes, and Group S = {CH₃OH, CH₃CHO} of methanol and acetaldehyde; all molecular abundance differences contribute equally to the group mean and are weighted equally using this method. Additionally for each group, we calculate the root-mean-squared deviation of the modeled abundances with respect to the observed abundances using the Bayesian uncertainties (Gratier et al., 2016) so that each difference in logarithm abundance is weighted by its observed uncertainty, and we compare these weighted fits with the unweighted fits. Finally, we identify the best models for each group and discuss both the effect the molecular group has on the grid model solution region and how uncertainties in the observed abundances constrain the model fits accordingly.

2.2 CHEMICAL MODEL

2.2.1 Physical Conditions

The dipole-allowed transition selection rules $\Delta J = \pm 1$ and $\Delta K = 0$ (where J and K are quantum numbers for the total angular momentum and its projection on the axis of molecular symmetry) of symmetric top molecules like methyl acetylene CH₃CCH separate the effects of radiative and collisional excitation. The kinetic temperature of the gas is reflected in the relative total populations of all J levels in each K ladder, which is controlled exclusively by collisional excitation (Bergin et al., 1994; Pratap et al., 1997). Toward TMC-1 (CP), the temperature measured using methyl acetylene emission ($J = 6 \rightarrow 5, K = 0, 1, 2$) and a statistical equilibrium analysis

in the LVG approximation is found to be 10 K and is consistent with the temperature determined from other molecular tracers of kinetic temperature like ammonia (Pratap et al., 1997). We adopt this temperature, which has been used in previous TMC-1 (CP) models, as the only value for both the gas and grain temperatures in our chemical model grids. Furthermore, statistical equilibrium analysis of the excitation of cyanoacetylene HC_3N ($J = 4 \rightarrow 3$, $J = 10 \rightarrow 9$, and $J = 12 \rightarrow 11$) constrains the density to $n = 8 \times 10^4 \text{ cm}^{-3}$ at temperature 10 K toward TMC-1 (CP) (Pratap et al., 1997).

The total nuclear spin I of the three hydrogen nuclei contained in the internally rotating methyl group ($-\text{CH}_3$) distinguishes either symmetric A^\pm ($I = 3/2$, *ortho*) or antisymmetric E ($I = 1/2$, *para*) nuclear spin states, each of which combines with rotational states that are antisymmetric or symmetric, respectively, to form a distinct rotational energy level spectrum (Sutton and Herbst, 1988; Rabli and Flower, 2010a,b; Levshakov, Kozlov, and Reimers, 2011). Following the a -type transition selection rules for asymmetric tops $\Delta J = -1$, $\Delta K_A = 0$, and $\Delta K_C = -1$, maps of the spatially resolved transitions $J_{K_A, K_C} = 1_{0,1} \rightarrow 0_{0,0}$, $2_{0,2} \rightarrow 1_{0,1}$, $3_{0,2} \rightarrow 2_{0,1}$ for A^+ states and $J_{K_A, K_C} = 2_{-1,2} \rightarrow 1_{-1,1}$, and $3_{-1,2} \rightarrow 2_{-1,1}$ for E states reveal lower densities $n = 1 - 4 \times 10^4 \text{ cm}^{-3}$ compared with the cyanopolyne emission along the line of sight to TMC-1 (CP) suggesting that methanol emission arises from an extended region of lower density (Soma et al., 2015). Our grid models vary over three densities, $n = 10^4$, $10^{4.5}$, and 10^5 cm^{-3} (see Table 2.1), spanning the values fit to the cyanoacetylene (Pratap et al., 1997) and methanol (Soma et al., 2015) emission toward TMC-1 (CP).

Though the observed molecular emission spectra constrain the kinetic temperatures and densities of each emitting molecular component along the line of sight, other physical conditions like the visual extinction, A_V , and cosmic ray ionization rate, ζ , depend on the total hydrogen column density, $N_{\text{H}} = N(\text{H}) + 2N(\text{H}_2)$, which is usually assumed to be constant with respect to the total column density of another molecular component throughout the emitting column. Imposing a constant ratio of the molecular hydrogen column density with respect to that of a molecular tracer to normalize a set of molecular column densities, however, presupposes each region of molecular emission arises from similar conditions, and this could introduce a systematic error into a set of abundance values scaled by this method (Liszt and Lucas, 2000). For abundances normalized by $N(\text{H}_2) = 10^{22} \text{ cm}^{-2}$ (Gratier et al., 2016), we select typical dark cloud values for the central extinction $A_V = 10$ and cosmic ray ionization rate $\zeta = 10^{-17}$, $10^{-17.5}$, and 10^{-16} s^{-1} (see Table 2.1) for consistency with previous studies of the chemical structure of TMC-1 (CP) (Garrod, Wakelam, and Herbst, 2007; Vasyunin and Herbst, 2013; Ruaud et al., 2015; Ruaud, Wakelam, and Hersant, 2016).

2.2.2 Chemical Kinetics

The ionization of molecular hydrogen by cosmic-ray impact initiates sequences of ion-neutral reactions, neutral-neutral reactions, and dissociative recombinations with free electrons, enriching the gas with several generations of molecular species of increasing complexity (Herbst and Klemperer, 1973; Woon and Herbst, 1996; Smith, Herbst, and Chang, 2004; Woon and Herbst, 2009). As gas-phase species accrete onto dust grain surfaces, light species gain mobility, and grain-surface chemistry proceeds via the Langmuir-Hinshelwood mechanism as species thermally diffuse (Hasegawa, Herbst, and Leung, 1992) or quantum mechanically tunnel (Hasegawa and Herbst, 1993a) from binding site to binding site across the grain surface. Ice mantles develop when the number of accreted molecules exceeds the number of binding sites on the surface, and the species contained within these mantles can further react as they diffuse through the bulk (Hasegawa and Herbst, 1993b; Garrod and Pauly, 2011; Garrod, 2013; Ruaud, Wakelam, and Hersant, 2016). The diffusion barrier (E_{diff}) between adjacent binding sites on the ice surface and within the ice mantle is unique for each molecule and modeled as a fraction of the binding energy of adsorption, $E_{\text{diff}} = bE_{\text{des}}$ where $0 < b < 1$. Several values of the ratio of the surface diffusion barrier to the binding energy, $b_s = E_{\text{diff}}^s/E_{\text{des}}$, have been used in dark cloud models, and we select three ratios corresponding to a low (Hasegawa, Herbst, and Leung, 1992), moderate, and high (Ruaud et al., 2015) value, $b_s = 0.3, 0.4$, and 0.5 , respectively. For the ratio of the bulk mantle diffusion barrier to the binding energy, $b_m = E_{\text{diff}}^m/E_{\text{des}}$, we use a single value of 0.8 for all species (Ruaud, Wakelam, and Hersant, 2016).

In previous dark cloud two-phase models in which only the gas and ice surface were chemically active (Garrod, Wakelam, and Herbst, 2007), the large binding energy of methanol inhibited the liberation of grain-surface methanol back to the gas, and without some non-thermal desorption mechanism, the observed gas-phase abundance of methanol was underproduced by the chemical models. Both photodesorption and desorption via exothermic surface reactions are nonthermal mechanisms by which methanol and other surface-bound species can enrich the gas phase, but the densities and extinctions in dark cloud models make photodesorption inefficient and exemplify situations in which reactive desorption specifically controls a gas-phase interstellar molecular abundance (Garrod, Wakelam, and Herbst, 2007; Vasyunin and Herbst, 2013). This study employs the Rice-Ramsperger-Kessel (RRK) formulation of the reactive desorption probability and parameter a (Garrod, Wakelam, and Herbst, 2007; Vasyunin and Herbst, 2013). A recent semiempirical approach invokes the equipartition of energy and an elastic collision process to model the probability of reactive desorption as seen in experiments (Minissale et al., 2016). In this formulation, the energy loss due to exothermicity is transferred to a component perpendicular to the substrate surface, and the efficiency is scaled by the masses of the product and the surface. This method allows for a greater level of detail to be considered for each reaction of this type within a chemical network.

Gas-phase species that collide with grain ice surfaces can also react upon collision via the Eley-Rideal mechanism or form weakly bound van der Waals complexes, which can then undergo hydrogenation to saturate; these mechanisms enhance the abundances of oxygen-containing organic precursors to methanol and acetaldehyde, which then hydrogenate and sufficiently enrich the gas with nominal reactive desorption efficiency ($a = 0.01$) (Ruaud et al., 2015). Our grid models include nominal, moderate, and high reactive desorption efficiencies $a = 0.01, 0.03,$ and 0.10 (see Table 2.1).

2.2.3 Reaction Network and Rate Solver

The evolution of the time-dependent molecular volume densities $[A]$ of a group of molecules $A = \{A_1, A_2, A_3, \dots, A_n\}$ subject to a system of chemical reactions (the chemical network) is obtained by integrating the corresponding system of differential rate law equations for each species i :

$$\begin{aligned} \frac{d[A_i]}{dt} = & \sum_j \sum_l k_{jl} [B]_j [C]_l + \sum_p k_p [D]_p \\ & - [A_i] \left(\sum_m k_m [F]_m + \sum_q k_q \right) \end{aligned} \quad (2.1)$$

where the first two terms express the two-body and one-body production mechanisms of A and the third and fourth terms represent the two-body and one-body destruction pathways. The abundances are computed by normalizing each time-dependent molecular volume density by the hydrogen volume density. Our chemical network is a combination of the latest gas-phase reactions of the periodically updated and benchmarked KInetic Database for Astrochemistry KIDA (Wakelam et al., 2012, 2015; Ruaud et al., 2015; Ruaud, Wakelam, and Hersant, 2016; Vidal et al., 2017; Le Gal et al., 2017) and a grain-surface-mantle network previously coupled with the KIDA (Garrod, Wakelam, and Herbst, 2007; Ruaud et al., 2015; Ruaud, Wakelam, and Hersant, 2016) to form a composite reaction network for use in three-phase (gas, ice-surface, ice-mantle) chemical models. To integrate the system of coupled, nonlinear differential rate law equations, we use the *Nautilus* code (Hersant et al., 2009; Hincelin et al., 2011, 2013, 2016; Ruaud, Wakelam, and Hersant, 2016), which has recently been updated to include the Eley-Rideal and van der Waals complex induced reaction mechanisms (Ruaud et al., 2015) and three-phase capabilities considering chemistry in the gas, on the ice surface, and throughout the ice mantle (Ruaud, Wakelam, and Hersant, 2016).

2.2.4 Elemental Composition

To account for material that is absent from the gas but still contributes to the total elemental composition of dark molecular clouds, a set of cosmic references abundances,

typically the solar elemental abundances, must be depleted by factors reflecting unobserved ice-phase material as well as the refractory dust grains, which are composed of amorphous olivine in our models (Semenov et al., 2010; Hincelin et al., 2011). For the initial fractional elemental abundances with respect to the total hydrogen density (see Table 2.2), we select the canonical low-metal abundances (Morton, 1974; Graedel, Langer, and Frerking, 1982) and include modifications for helium (Wakelam and Herbst, 2008), carbon and nitrogen (Jenkins, 2009), and fluorine (Neufeld, Wolfire, and Shilke, 2005). Oxygen, which is contained in both ice species and the dust grains of dark clouds, has a depletion factor that has been shown to increase with increasing density over a sample of hundreds of lines of sight with diffuse cloud densities $n(\text{H}) \leq 10 \text{ cm}^{-3}$ (Jenkins, 2009). We use the two values $f_{\text{O}} = 2.4 \times 10^{-4}$ and 1.4×10^{-4} extrapolated for dense cloud conditions (Hincelin et al., 2011) representing intermediate and high depletion cases, respectively. The time-dependent abundances of the cyanopolyynes and small oxygen species are sensitive to the C/O ratio (Wakelam et al., 2010); the values $f_{\text{C}}/f_{\text{O}} = 0.7$ and 1.2 in our models differentiate oxygen-rich, carbon-poor conditions from oxygen-poor, carbon-rich conditions and illustrate the effect oxygen depletion has on models of dark interstellar clouds and the abundances toward TMC-1 (CP).

2.2.5 Grid Models

In general, grids of homogeneous chemical kinetic models demonstrate the effect that variations in the initial parameters of the rate law equations have on the time-dependent abundance solutions. Methods of mapping homogeneous chemical models to arrays of observationally constrained physical conditions have reproduced the chemical structure of Active Galactic Nuclei (Harada, Thompson, and Herbst, 2013) and protoplanetary disks (Öberg et al., 2015; Cleeves et al., 2016), and chemical heterogeneity along a single line of sight warrants a similar approach to model the accompanying physical heterogeneity of the spatially distinct regions of emission. Astrochemical grid models have also been used to determine time-dependent column densities, benchmark chemical networks and models, and predict molecular emission line intensities in starburst galaxies from statistical equilibrium calculations in the LVG approximation (Viti, 2017). We automate the execution of the `Nautilus` code (Ruaud, Wakelam, and Hersant, 2016) over a 7-D parameter space (gas kinetic temperature T_{gas} , density n , visual extinction A_{V} , cosmic ray ionization rate ζ , dust temperature T_{dust} , reactive desorption efficiency a , and diffusion to binding energy ratio b), as shown in Table 2.1, and for each molecule i we construct a 9-D data structure $\{X_i, t, T_{\text{gas}}, n, A_{\text{V}}, \zeta, T_{\text{dust}}, a, b\}$ containing the abundance X_i at every time t and every combination p of free parameters $\{T_{\text{gas}}, n, A_{\text{V}}, \zeta, T_{\text{dust}}, a, b\}$. To obtain solutions that explicitly separate the effects of the new mechanisms and the elemental composition, we compute four grids, Models A, B, C, and D, for two elemental compositions, C/O = 0.7 and 1.2 corresponding to intermediate and high cases of oxygen depletion, and either inactive (N) or active (Y) Eley-Rideal (ER) and van der

Waals (vdW) reaction mechanisms (see Table 2.3).

For each position $(p, t) = (T_{gas}, n, A_V, \zeta, T_{dust}, a, b, t)$ in our grids and for each molecular Group $M = G, C, S$, we calculate the root-mean-square (hereafter rms) log difference

$$\mathcal{A}(p, t) = \left[\frac{1}{n} \sum_i^n [\log(X_{\text{mod}}(p, t)/X_{\text{obs}})]_i^2 \right]^{1/2} \quad (2.2)$$

between the modeled and observed fractional abundances, X_{mod} and X_{obs} , respectively, for the n molecular abundances in each group. The rms log difference $\mathcal{A}(t)$ of each group quantifies the average factor of agreement between the observed and corresponding modeled abundances but neglects uncertainties in both the modeled and observed abundances. Meaningful solutions to the rate law equations exist for the observed abundances when the rms log difference is less than some criterion value $\mathcal{A}_{\text{crit}}$, and we impose $\mathcal{A}_{\text{crit}} = 1$ corresponding to an average factor of agreement between modeled and observed abundances within each group of one order of magnitude. The best fit time \mathcal{T} or chemical timescale of each model with parameters p is calculated by minimizing the rms log difference $\mathcal{A}_{\text{min}} = \mathcal{A}(p, \mathcal{T})$ for each model.

Statistical methods, specifically the Bayesian analysis of emission line spectra, however, produce column densities with uncertainties σ_i that reflect the prior uncertainty distributions of free parameters of the LTE model of the emission spectra of each molecular component (Gratier et al., 2016). As shown in Table 2.4, the uniqueness of each observed molecular emission spectrum results in unequal standard deviations for the LTE column densities, and these uncertainties propagate unchanged to the observed abundances if a constant hydrogen column density is assumed along the regions of integrated emission traced by each of the column densities. For each group of molecules, the agreement between a modeled set of abundances and an observed set of abundances with a corresponding set of uncertainties can be quantified by the mean deviation

$$\sigma(p, t) = \left[\frac{1}{n} \sum_i^n \left(\frac{\log(X_{\text{mod}}(p, t)/X_{\text{obs}})}{\sigma_i} \right)_i^2 \right]^{1/2} \quad (2.3)$$

between the modeled and observed abundances in units of σ_i , the 1σ deviations associated with each of the observed abundances. The rms deviation $\sigma(p, t)$ or weighted fit measure reduces to the unweighted fit measure $\mathcal{A}(p, t)$ when all 1σ deviations σ_i are unity corresponding to a standard deviation of an order of magnitude difference between the modeled and observed relative molecular abundances. Because the 1σ values are reported with the observed abundances, we use $\sigma_{\text{crit}} = 1$ as the solution criterion similar to the rms log difference. The weighted fit measure inaccurately expresses the mean deviation for a group of molecules with individual deviations that largely differ from each other. As terms diverge in value and some begin to domi-

nate the sum while others diminish in contribution, the reduction factor $\frac{1}{\sqrt{n}}$ of the size of the group n no longer represents the number of molecules that meaningfully contribute, and the weighted fit measure $\sigma(p, t)$ underestimates the mean deviation within the group. The same is true for the unweighted fit measure $\mathcal{A}(p, t)$, which lacks the uncertainties as weights. Small uncertainties demand better agreement between the modeled and observed abundances for equal contribution to the mean, and both biases favor the large contributions to the mean. The observed abundances of molecules in each group C and S exhibit uncertainties σ_i that resemble the the rest of the group so that the mean deviation has meaning when grouping in this manner and corresponds to a similar factor of agreement between the observed and modeled abundances within each group.

2.3 RESULTS AND DISCUSSION

2.3.1 General Characteristics of the Modeled Abundances

Figures 2.1, 2.2, 2.3, and 2.4 show the modeled and observed time-dependent abundances $X(t)$ of each molecule represented in both the TMC-1 emission line survey analysis (Gratier et al., 2016) and the chemical network (Group G) for Models A, B, C, and D, respectively. Each panel shows the abundances of a single molecule for different density and ionization rate pairs contained in each restricted model at single values of the reaction desorption efficiency ($a = 0.01$) and the diffusion-binding energy ratio ($b = 0.4$). The linestyle corresponds to the cosmic ray ionization rate (solid for $\zeta = 10^{-17} \text{ s}^{-1}$, dashed for $\zeta = 10^{-16.5} \text{ s}^{-1}$, and dot-dashed for $\zeta = 10^{-16} \text{ s}^{-1}$), while the color indicates the value of density (blue for $n = 10^5 \text{ cm}^{-3}$, cyan for $n = 10^{4.5} \text{ cm}^{-3}$, and red for $n = 10^4 \text{ cm}^{-3}$).

Each time-dependent abundance for each molecule exhibits at least one of four characteristics :

1. Small carbon-containing species c-C₃H, l-C₃H, l-C₃H₂, H₂CCN, HCS⁺ and ammonia NH₃ exhibit abundances that show little variation (*inertness*) between $\sim 10^5$ and 10^6 years and over the densities and ionization rates contained in the chemical model parameter space. The abundances of ammonia NH₃ and of hydrocarbons c-C₃H, l-C₃H, l-C₃H₂ are within an order of magnitude of the observed values for long periods of time ($t = 2 \times 10^4 - 2 \times 10^6$ years) for all Models A, B, C, and D, while the heavier species H₂CCN, HCS⁺ are underproduced except in Model C where, as a result of increased oxygen depletion, the relative increase in the elemental carbon abundance increases the abundances of H₂CCN so that it agrees within an order of magnitude of the observed value for a long period of time.

2. A single peak or trough corresponding to a clear *maximum* or *minimum* abundance is another common feature. Maxima are present in the oxygen-containing organic species CH₃CHO, the cyanopolyne HC₃N, and the carbon-chain molecules CH₃CN, CH₃CCH, H₂CCO, C₄H₂, HCCNC, C₃O, HC₃NH⁺, CH₃C₄H, CH₃C₃N, C₃S. The carbon-chain C₆H presents the only clear minimum between 2×10^4 and 2×10^6

years in Models A and B. The effect of density and cosmic ray ionization rate on the timescale immediately appears in each panel where greater densities and greater ionization rates produce earlier timescales and where lower densities and lower ionization rates effect similar abundance features at later times so that the timescale appears inversely related to both density and ionization rate.

3. Molecules *c*-C₃H₂, CH₃OH, H₂CS, and C₄H₂ show a *monotonic* increase of the time-dependent abundances with no clear maximum or minimum. Two quasi steady-states (periods of time where the abundances change very little) in the time-dependent abundances of CH₃OH, H₂CS, and C₄H₂ appear at early ($t < 10^5$ year) and late ($t > 10^5$ year) times, while the abundances of *c*-C₃H₂ resemble the inert character with a slight positive gradient in time.

4. The abundances of cyanopolyynes HC₅N, HC₇N, and HC₉N in addition to the abundances of both C₃N and C₅H in Model A *oscillate* in time exhibiting large variation in both magnitude and feature character when density and cosmic ray ionization rate vary. The abundances of these molecules vary up to five orders of magnitude, and the oscillatory behavior is exemplified by the larger cyanopolyne abundances $X_{\text{HC}_7\text{N}}(t)$ and $X_{\text{HC}_9\text{N}}(t)$ in Models A and B in which the amplitude of oscillation increases toward low densities and high ionization rates ($n = 10^4 \text{ cm}^{-3}$, $\zeta = 10^{-16} \text{ s}^{-1}$).

The characteristic behaviors for the time-dependent abundances of individual molecules change throughout the grid models as the free parameters vary; Table 2.4 contains a summary of the behavior character types $\mathcal{C} = 1, 2, 3,$ and 4 of the time-dependent abundances for each Model A, B, C and D in the restricted grid space ($a = 0.01$, $b = 0.4$) shown in Figures 2.1, 2.2, 2.3, and 2.4.

2.3.2 Grid Solutions and Agreement

Figures 2.5, 2.6, and 2.7 show the time-dependent rms log difference $\mathcal{A}(t)$ and rms deviation $\sigma(t)$ on appropriate scales over the restricted grids for the three molecular Groups, G, C, and S, respectively, and we apply the aforementioned characteristic behavior types to describe $\mathcal{A}(t)$ and $\sigma(t)$. For single minima \mathcal{A}_{min} with clear concavity, the reasonable span of the chemical timescale depends on the criterion value $\mathcal{A}_{\text{crit}}$ describing the region of reasonable agreement $\{t\}$ when $\mathcal{A}_{\text{min}}(t) < \mathcal{A}_{\text{crit}}$. Model fits exhibiting low mean differences or deviations with little variation over extended timescales place weaker constraints on the solution $\{t\}$ when $\mathcal{A}_{\text{min}}(t) < \mathcal{A}_{\text{crit}}$ since many times would satisfy this condition. When rms differences oscillate, imposing a value of $\mathcal{A}_{\text{crit}}$ will separate the region of solution $\mathcal{A}_{\text{min}}(t) < \mathcal{A}_{\text{crit}}$ into distinct features when $\mathcal{A}(t) > \mathcal{A}_{\text{crit}}$ during the oscillation. Comparing $\mathcal{A}(t)$ and $\sigma(t)$ illustrates the effects the uncertainty type and group sizes have on the agreement between modeled and observed abundances.

We summarize \mathcal{A}_{min} in Tables 2.6, 2.7, 2.8, and 2.9 and σ_{min} in Tables 2.10, 2.11, 2.12, and 2.13 for each point p in the grid by assigning symbols to illustrate the general agreement of each group with respect to the observed abundances and

uncertainties. We classify the model fit measures \mathcal{A}_{\min} into three distinct regions: $\mathcal{A}_{\min} > 1$ (open, \circ), $1 \geq \mathcal{A}_{\min} \geq .5$ (dotted, \odot), $\mathcal{A}_{\min} < 0.5$ (closed, \bullet); the mean deviations follow the same symbolic representation since the 1σ uncertainty values are reported with the observed abundances. We divide the best fit times \mathcal{T} into four regions: $\log(\mathcal{T}) < 5$ (crescent, \mathcal{C}), $5 < \log(\mathcal{T}) < 6$ (open, \circ), $6 < \log(\mathcal{T}) < 7$ (dotted, \odot), $\log(\mathcal{T}) > 7$ (closed, \bullet) (see the bottom halves of Tables 2.6 - 2.13). The symbolic representation shows the degree and extent of model agreement and consistency among molecular groups over the grid spaces, and the trends in the solution space characterize the model with respect to the observed abundances over a large parameter space, naturally benchmarking the chemical network and code in many unique sets of homogeneous conditions.

To visualize the solution space of our four grid Models A, B, C, and D over four varied free parameters, n , ζ , a , and b , we record the minimum fit measures for each point in the grid, $\mathcal{A}_{\min}(p, \mathcal{T})$, the minimum mean deviations $\sigma_{\min}(p, \mathcal{T})$, and the corresponding timescales \mathcal{T} for each grid point $p = \{n, \zeta, a, b\}$ and project the values on inner axes of $n \times \zeta$ and outer axes of $a \times b$. The remaining parameters $\{T_{\text{gas}}, A_V, T_{\text{dust}}\}$, each of which subtends only a single value, maintain that single value throughout the analysis and discussion. The symmetry of the minimum fit measure matrices over the span of densities and ionization rates, $\mathcal{A}_{\min}^{\zeta \times n}$, emerges across the main diagonal $\log(n) + \log(\zeta) = -12$ (top left to bottom right, see note in Table 2.5) producing sets of m degenerate solutions ($\mathcal{A}_{\min}^1 \sim \mathcal{A}_{\min}^2 \sim \dots \sim \mathcal{A}_{\min}^m$) along diagonals of $\eta = \log(n) - \log(\zeta)$ implying η is a natural quantification of solutions $\mathcal{A}_{\min} < 1$ in these particular grids. For the grids of dark cloud conditions, η , as seen in Table 2.5, is defined over the set of half integers between and including the maximum and minimum values of density and ionization rate, $\eta = 22$ when $\log(n) = 5$ and $\log(\zeta) = -17$ and $\eta = 20$ when $\log(n) = 4$ and $\log(\zeta) = -16$, respectively, or $\log(n) - \log(\zeta) = \eta = \{20, 20.5, 21, 21.5, 22\}$ and relates to ζ/n in previous studies by $\eta = -\log(\zeta/n)$ (Lepp and Dalgarno, 1996; Tiné et al., 1997).

The Total Group G

Models A and B show little if any solution $\{t\}$ when $\mathcal{A}(t) < 1$ is satisfied implying a poor fit with average factors of agreement greater than an order of magnitude. The elemental composition $C/O = 1.2$, or the high oxygen depletion case, improves fits and strengthens the minimum character of $\mathcal{A}(t)$ in Models C and D demonstrating the preference of Group G abundances to carbon-rich, oxygen-poor conditions. Because $\mathcal{A}(t) < 1$ is true for short time periods as seen in Figure 2.5, each point model solution is only instantaneously well-constrained in time, and this corresponds to a minimum solution. The oscillatory behavior character of $\mathcal{A}(t)$ and $\sigma(t)$ in Models A and B changes in Models B and D either to functions with clear minima or to those that decrease monotonically in time. This change reflects the time-dependent abundances of HC_7N and HC_9N , which change from oscillatory functions in Models A and B to functions with clear maxima, larger values, and sharper behavior in Models C and D.

The best instantaneous solution, $\mathcal{A}_{\min} = 0.66$, corresponding to an average factor of agreement of 4.6 for the 32 abundances, appears at time $\mathcal{T} = 1.8 \times 10^5$ years in Model D for dense conditions ($n = 10^5 \text{ cm}^{-3}$ and $\zeta = 10^{-17} \text{ s}^{-1}$), a large diffusion-binding energy ratio ($b = 0.5$), and a high reactive desorption efficiency ($a = 0.1$), though many solutions $\mathcal{A}_{\min} < 1$ exist throughout the grid models. The small uncertainties on several of the observed abundances result in large mean deviations $\sigma(t) > 3$ at all times, and the behavior of $\sigma(t)$ is similar to $\mathcal{A}(t)$, though $\sigma(t)$ appears exaggerated over its larger scale.

The timescales associated with the minimum mean deviations for Group G remain relatively consistent with those determined by minimizing the rms log difference $\mathcal{A}(p, t)$ between the observed and modeled abundances, but the range of minimum mean deviations $3.5 < \sigma_{\min}(p, \mathcal{T}) < 7$ reveals the inability of any single homogeneous model within our grids at any time to reproduce successfully a set of 32 observed abundances constrained by the uncertainties σ_i produced by the LTE model and Bayesian analysis of the observed emission. Furthermore, because the observed abundance uncertainties vary in size, the mean deviation does not equivalently quantify the agreement for all species in this group.

The Cyanopolyyne Group C

The new observed abundances of the cyanopolyynes (Gratier et al. (2016), see our Table 2.4) differ by only a factor of a few (≤ 4) when compared to previous values (Smith, Herbst, and Chang, 2004), but earlier large gas-grain kinetic models of TMC-1 (CP) using a low C/O ratio failed to reproduce the cyanopolyyne abundances consistently with the rest of a larger group (Garrod, Wakelam, and Herbst, 2007). In our models, the timescales of maximum abundance for HC_3N and HC_5N vary inversely with both the density and the ionization rate. Increased oxygen depletion and the increased C/O ratio of Model C moves the maximum abundances of HC_3N , HC_5N , and HC_7N of the darkest model $n = 10^5 \text{ cm}^{-3}$ and $\zeta = 10^{-17} \text{ s}^{-1}$ very close to the observed values determined from the TMC-1 (CP) emission, and an instantaneous quasi-steady state, which is exemplified by a critical point where the first time derivative of the abundance is equal to zero, emerges at 10^5 years for these three cyanopolyyne abundances. The abundance of HC_7N exhibits the same behavior as the abundances of the smaller two cyanopolyynes over the restricted grid space ($b = 0.4$ and $a = 0.01$) of Models C and D but oscillates in time in Models A and B. The maximum abundances over the restricted grid space for the first three cyanopolyynes remain within an order of magnitude of the observed values for extended periods throughout Models C and D. The final observed cyanopolyne, HC_9N , exhibits underproduction in Model A, and while the increased C/O ratio of Model C generally induces a shift of the abundances of the restricted grid space to within an order of magnitude of the observed value for extended timescales, significant overproduction of HC_9N skews the average agreement in Model C, where this overproduction increases the modeled abundances beyond an order of magnitude above the observed

value. Furthermore, in contrast to the smaller cyanopolyynes, the abundance of HC_9N in the darkest model $n = 10^5 \text{ cm}^{-3}$ and $\zeta = 10^{-17} \text{ s}^{-1}$ in Model C is no longer as well fit to the observed abundance.

The cyanopolyynes are formed in the gas phase via the dissociative recombination of protonated precursors:



and from reactions



and



between atomic and neutral radicals and other carbon-chain molecules lacking nitrogen. A recent emission line survey of cyanopolyyne carbon isotopologues toward TMC-1 (Burkhardt, et al., 2017) showed by process of elimination that the reactions between hydrocarbon ions and atomic nitrogen must dominate the production of cyanopolyynes HC_5N and HC_7N , but the proposed chemical network lacks reactions between neutral carbon chains and atomic nitrogen similar to equation (2.5) as a possible mechanism of formation. The cyanopolyynes are destroyed through ion-neutral reactions in the gas with abundant ions that produce the protonated precursors and from neutral-neutral reactions of the type



with abundant atomic species such as carbon.

The dissociative recombination of the protonated precursors dominates the production of all of the cyanopolyynes at the best fit times along the restricted main diagonal except for the two larger cyanopolyynes, HC_7N and HC_9N , in the darkest conditions, $\eta = 22$, and the least dark conditions, $\eta = 20$, where the neutral-neutral reactions involving atomic nitrogen and the cyano radical contribute most to their production, respectively, at the chemical timescales. Increasing both oxygen depletion and the carbon-oxygen ratio in Model C to $\text{C}/\text{O} = 1.2$ shifts the dominant production pathways of all of the cyanopolyynes to neutral-neutral reactions at the best times for all η along the restricted main diagonal, and substantial destruction involving the cyano radical also emerges as a results of the elemental composition.

Characteristic of the abundances of the two large cyanopolyynes $X_{\text{HC}_7\text{N}}(t)$ and $X_{\text{HC}_9\text{N}}(t)$, the rms log difference $\mathcal{A}(t)$ for Group C exhibits oscillatory behavior with respect to time in Models A and B where solutions $\mathcal{A}(t) < 1$ appear at long timescales ($t > 5 \times 10^5$ years) and improve with respect to decreasing density and increasing ionization rate. The amplitude of the oscillations increases as the Eley-Rideal and van der Waals complex reaction mechanisms are activated, but the overall behavior

of $\mathcal{A}(t)$ with respect to the models without the new mechanisms is preserved. The small uncertainties in the cyanopolyynes abundances result in large mean deviations ($\sigma(t) > 3$) for all models in grid Models A and B and can be seen in Figure 2.6. A very large solution region with $\mathcal{A}(t) < 1$ emerges in our restricted grid Models C and D with increased oxygen depletion for Group C, and the mean deviations illustrate the exaggeration of the behavior of $\mathcal{A}(t)$ as $\sigma(t)$ sharply changes around its minima. The best solution for Group C, $\mathcal{A}_{\min} = 0.14$, corresponding to an average factor of agreement of 1.4, appears in Model C at a slightly earlier time ($\mathcal{T} = 7.1 \times 10^4$ years) than Group G but with the same dense conditions ($n = 10^5 \text{ cm}^{-3}$ and $\zeta = 10^{-17} \text{ s}^{-1}$), large diffusion-binding energy ratio ($b = 0.5$), and high reactive desorption efficiency ($a = 0.1$).

Similar to Group G, the timescales associated with the minimum deviation of Group C are very similar to those determined using the unweighted fit method. In contrast to the generally good agreement reflected by $\mathcal{A}_{\min}(p, \mathcal{T})$, the range of minimum rms deviations, $1.5 < \sigma_{\min}(p, \mathcal{T}) < 4.5$, reflects the constraining effect several small uncertainties have on the agreement between the chemical kinetic model and the abundances derived from an LTE model of the molecular emission spectra observed toward TMC-1 (CP). Although our models fit the observed abundances often within a factor of a few, we cannot reproduce at any time the cyanopolyynes abundances within a mean standard deviation of the abundances constrained by the prior distributions of observed column densities determined from the Bayesian analysis of the LTE model of the numerous observed emission lines.

The Oxygen-containing Organic Species Group S

Initial models of TMC-1 implementing reactive desorption (Garrod, Wakelam, and Herbst, 2007) showed enhancement of the abundance of gas-phase acetaldehyde over two orders of magnitude, but even with high reactive desorption efficiency ($a = 0.1$), the acetaldehyde abundance $X_{\text{mod}}(\text{CH}_3\text{CHO}) = 1.7 \times 10^{-11}$ did not sufficiently reproduce the observed value $X_{\text{obs}}(\text{CH}_3\text{CHO}) = 6 \times 10^{-10}$. In contrast, these first models sufficiently reproduced the observed abundance of gas-phase methanol $X_{\text{obs}}(\text{CH}_3\text{OH}) = 3 \times 10^{-9}$ at the best fit time for models with moderate reactive desorption efficiency: $X_{\text{mod}}(\text{CH}_3\text{OH}) = 1.1 \times 10^{-9}$ for $a = 0.03$.

The gas-phase abundance of methanol challenged astrochemical kinetic models until nonthermal desorption enabled some of the methanol formed via exothermic surface reactions to return to the gas upon formation following the hydrogenation of lighter species on the grain surfaces,



and



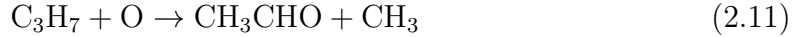
and this mechanism dominates the production at all times \mathcal{T} along the main diagonal

$\eta = 22$ ($n = 10^5 \text{ cm}^{-3}$ and $\zeta = 10^{-17} \text{ s}^{-1}$), 21 ($n = 10^{4.5} \text{ cm}^{-3}$ and $\zeta = 10^{-16.5} \text{ s}^{-1}$), and 20 ($n = 10^4 \text{ cm}^{-3}$ and $\zeta = 10^{-16} \text{ s}^{-1}$). In Model B, fragmentation through dissociative recombination of protonated dimethyl ether



dominates the production in the dark model $\eta = 22$ at time $\mathcal{T} = 2.6 \times 10^5$ years as a result of the additional ice-surface dimethyl ether created from the successive hydrogenation of a carbon-methanol van der Waals complex. Even with low non-thermal desorption efficiency ($a = 0.01$), the gas phase abundance of dimethyl ether is enhanced by several orders of magnitude at all times $t < 3 \times 10^7$ years as a result of the increased ice abundance. The abundance of protonated dimethyl ether, which forms in the gas through the reaction between gas-phase dimethyl ether and abundant ions, successfully fuels the gas-phase dissociative recombination reaction to competitive levels with respect to the other methanol formation mechanisms of Model A. Methanol is destroyed by ion-neutral and neutral-neutral reactions with abundant ions and atoms in the gas, respectively.

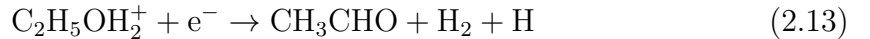
Acetaldehyde exhibits the reverse situation: in Model A without the new mechanisms, the neutral-neutral reactions



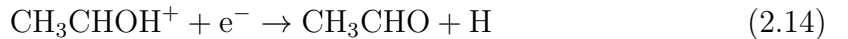
and



between hydrocarbons and atomic oxygen in the gas primarily constitute the overall production along the restricted main diagonals with slight contribution from the dissociative recombination reactions



and



of larger protonated precursors. When the new mechanisms are activated in Model B, nonthermal desorption via the hydrogenation of surface-bound acetyl radical



comes to dominate the gas-phase acetaldehyde production in the darkest model ($\eta = 22$). Similar to the other species, acetaldehyde is destroyed in the gas upon reacting with abundant ionic and neutral carbon, and the abundances for methanol and acetaldehyde, over the restricted grid spaces of Models A and B, show the same dependence on ζ and n as well as the enhancement from the new mechanisms.

The rms log differences $\mathcal{A}(t)$ and deviations $\sigma(t)$ for Group S all appear as distinct minima, with better fits for low densities and high ionization rates. The new mechanisms improve the fit of the densest model ($n = 10^5 \text{ cm}^{-3}$ and $\zeta = 10^{-17} \text{ s}^{-1}$) in Model B, and the greater oxygen abundance of Models A and B results in a minimum solution $\mathcal{A}(t) < 1$ over larger regions of the grids. In contrast to the total group and the cyanopolyynes, the character of the rms deviation $\sigma(t)$ of Group S appears relatively flat in time with $\sigma(t) < 1$ for long time periods in all but the densest conditions, where a minimum fit is seen in Figure 2.7. In oxygen-rich conditions, the combination of new mechanisms and large lower uncertainties on the observed abundance values results in simultaneous good agreement $\mathcal{A}(t) < 1$ and high confidence $\sigma(t) < 1$ for the oxygen-containing organic species in Group S.

Model C contains the best average factor of agreement of 1.06 at time $\mathcal{T} = 3.1 \times 10^5$ years at low density ($n = 10^4 \text{ cm}^{-3}$ and $\zeta = 10^{-17} \text{ s}^{-1}$), small diffusion-binding energy ratio ($b = 0.3$), and high reactive desorption efficiency ($a = 0.1$). All Models A, B, C, and D have best average factors of agreement < 1.2 , and the abundances of methanol and acetaldehyde are well-fit simultaneously in large regions of the grids. At time $\mathcal{T} = 1.5 \times 10^5$ years, the lowest average deviation $\sigma_{\min} = 0.05$ appears in Model B with similar parameters to the best average factor of agreement with a slightly faster cosmic ray ionization rate. The low diffusion-binding energy ratio ($b = 0.3$) of these best fits agrees with the best value in previous three-phase chemical models of methanol (Ruaud, Wakelam, and Hersant, 2016).

2.3.3 Effect of New Mechanisms and Elemental Composition

Many of the carbon-chain molecules including the cyanopolyynes HC_5N , HC_7N , and HC_9N are underproduced in Model A and oxygen-rich conditions ($\text{C}/\text{O} = 0.7$) and appear to oscillate over the restricted grid space ($a = 0.01$ and $b = 0.4$). Activating the Eley-Rideal and van der Waals complex reaction mechanisms (Model B) results in lowered abundances at later times ($t > 10^5$ year) for all cyanopolyynes HC_3N , HC_5N , HC_7N , and HC_9N and many other carbon-containing species, though this effect generally does not result in significant movement from the region of solution for the observed abundances. The two oxygen-containing organic species CH_3OH and CH_3CHO benefit from the additional production from the new mechanisms and increase in abundance at early times creating periods between 2×10^4 and 2×10^6 years within the lower uncertainty limit in the restricted grids. Increasing the elemental oxygen depletion in Model C ($\text{C}/\text{O} = 1.2$) greatly enhances the abundances of many of the carbon-containing molecules leading to better fits for H_2CCN , HC_3N , HCCNC , HC_3NH^+ , CH_2CHCN , $\text{CH}_3\text{C}_4\text{H}$, $\text{CH}_3\text{C}_3\text{N}$, C_3S , C_6H , HC_3N , HC_5N , HC_7N , and HC_9N , but the oxygen-containing species CH_3CHO and H_2CCO suffer decreased peak abundances in this elemental composition. Model D reveals the composite effect of oxygen-poor conditions and active new mechanisms on the modeled abundances of the carbon-chain molecules, which remain good fits to the observed values despite the detrimental effect of the new mechanisms. Similarly, the modeled abundances for

oxygen-containing organic species CH_3OH and CH_3CHO remain good solutions with increased oxygen depletion when the new mechanisms are active.

2.3.4 Effect of Reactive Desorption and the Diffusion-binding Energy Ratio

Moderate to high values $a = 0.03$ and 0.1 of the reactive desorption efficiency produce improved fits in Models A and B for all Groups G, C, and S where solutions following the criterion $\mathcal{A}_{\min} < 1$ emerge for less dense models $\eta \leq 21$. An increase in oxygen depletion ($\text{C/O} = 1.2$) in Models C and D results in overall better fits for Groups G and C at lower reactive desorption efficiencies ($a = 0.01$) while Group S exhibits weaker fits that can be mitigated with increasing reactive desorption efficiency ($a = 0.03, 0.1$). The diffusion-binding energy ratio b has a marginal effect on \mathcal{A}_{\min} , which is fairly constant with respect to b for every group, implying that the best fits and times are not sensitive to this parameter over the grid spaces. Though individual molecules may present large sensitivities to b , each group fit is not significantly impacted by this parameter alone.

2.4 SUMMARY

An astrochemical kinetic grid model is an array of time-dependent abundances $X_i(t)$ for molecules i in a chemical network calculated for different physical conditions and over ranges of free parameters in the chemical model. To solve the rate law equations and obtain the time-dependent abundances for the physical conditions determined from the emission of tracers of both compact, dense material (cyanoacetylene) and an extended region of emission (methanol) along the line of sight to TMC-1 (CP), we parallelize the execution of the rate solver over the span of the representative grid space for dark cloud conditions. For each molecule i in the chemical network, we construct a 9-D grid of abundances, $\{X_i, t, T_{\text{gas}}, n, A_V, \zeta, T_{\text{dust}}, a, b\}$ and attempt to account for chemical and physical heterogeneity along a single line of sight by grouping observed abundances according to similar chemistry and minimizing a measure of the differences between the observed and modeled abundance values. The rms log difference \mathcal{A} between the modeled and observed abundances parametrizes the average factor of agreement, while the rms deviation σ quantifies the average factor of agreement only when the uncertainties in the group resemble each other; we minimize both of these for all *points* p in the grid corresponding to all combinations of free parameters $\{n, \zeta, a, b\}$ and record the resultant timescales. We compare each method by tabulating $\mathcal{A}_{\min}(\mathcal{T})$ and $\sigma_{\min}(\mathcal{T})$ for each of the *points* in each grid, and we juxtapose values for three different groups of molecules to show how reducing a large group of observed molecular abundances to smaller groups with chemical similarity resolves, for the sets of observed abundance values, a solution space throughout the grid models that generally exhibits better agreement than that of the large group. Grid models and an extensive parameter space allow for competing effects in the model to be separated revealing the unique solution profiles for each group.

Some salient features of our calculations are listed below:

- The fits of all Groups G, C, and S are sensitive to the density n , cosmic ray ionization rate ζ , the reactive desorption efficiency a , and the carbon-oxygen elemental abundance ratio, C/O.
- The Eley-Rideal and van der Waals reaction mechanisms enhance the production of the oxygen-containing organic species leading to better fits over the model space.
- The diffusion-binding energy ratio b effects marginal changes in the agreement between our models and the observed abundances toward TMC-1 (CP).
- The oxygen-containing organic species of Group S prefer a low carbon-oxygen elemental abundance ratio (C/O = 0.7) in contrast to the composite Group G and the cyanopolyynes of Group C, both of which show better agreement with TMC-1 (CP) abundances for models utilizing a higher carbon-oxygen ratio (C/O = 1.2).
- The solution space of the cyanopolyynes, Group C, extends to include dense models consistent with the observed abundances in high oxygen depletion conditions, though the dominant chemical pathways at the best fit times shift from dissociative recombination of the protonated precursors to neutral-neutral pathways in the dark conditions given by $\eta = 22$.
- Small observed uncertainties for Group C result in no solution $\sigma_{\min} < 1$ in any model, and this is similarly seen for Group G.
- The character of the time-dependent rms log difference between observed and modeled abundances is preserved, albeit scaled, when calculating the rms deviation, and the quality of agreement reflected by the rms deviation depends on the uncertainties within the group.

As interferometric maps of molecular emission become more widely available and as the physical conditions of each molecular component are determined independently along a single line of sight, grids of chemical models will continue to provide a multi-dimensional approach to mapping chemical structure and will check the consistency among models of molecular emission and the chemical networks used to express the time-dependent chemical structure of groups of molecular components with coupled chemistries.

2.5 ACKNOWLEDGMENTS

E.H. thanks the National Science Foundation for its support of the astrochemistry program at the University of Virginia through grant AST 1514884. T.V.W. is supported by the NSF through the Grote Reber Fellowship Program administered by Associated Universities, Inc./National Radio Astronomy Observatory, the D.N. Batten Foundation Fellowship from the Jefferson Scholars Foundation, the Mars Foundation Fellowship from the Achievement Rewards for College Scientists Foundation, and the Virginia Space Grant Consortium.

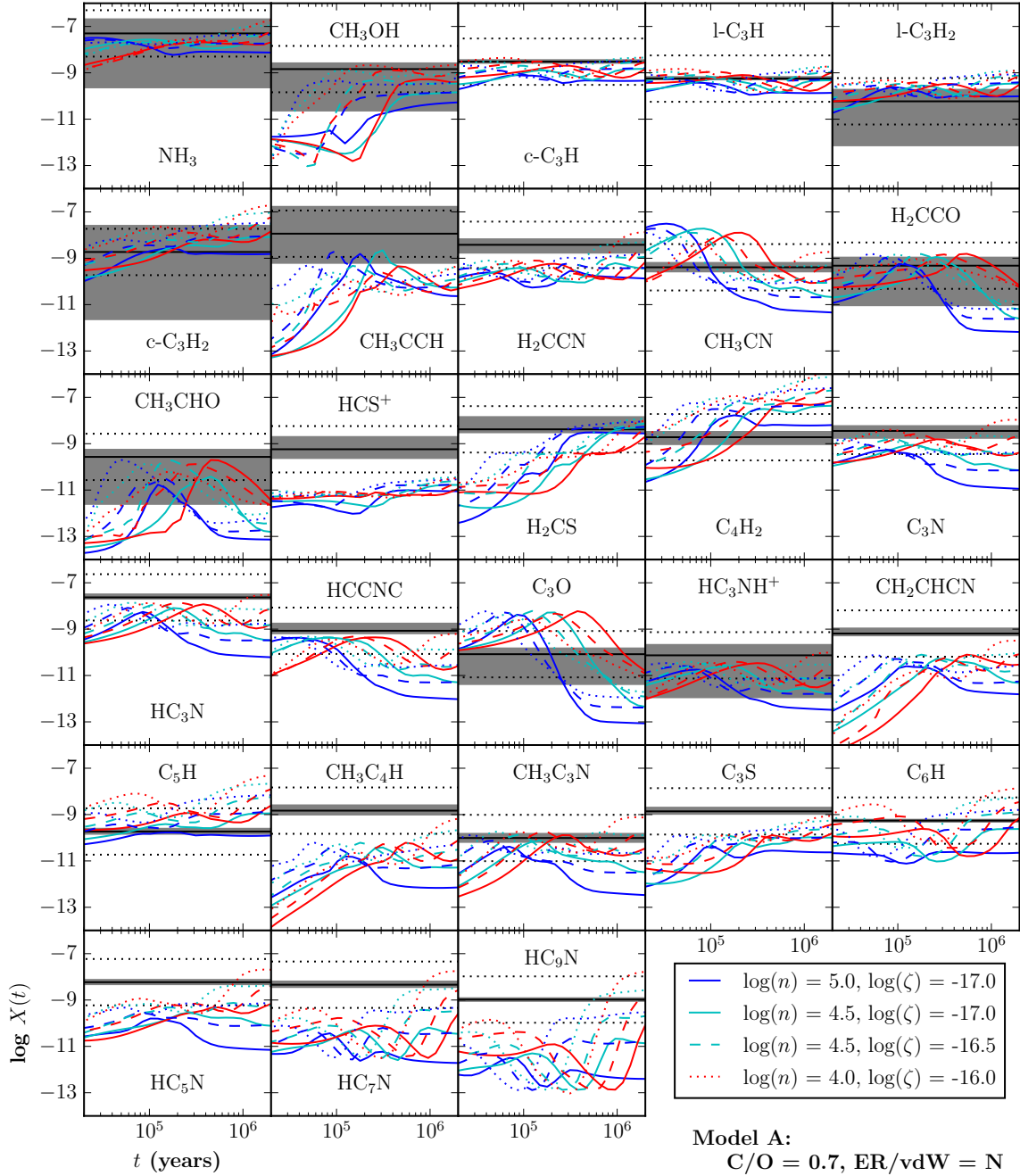


Figure 2.1: Time-dependent abundances $\log X(t)$ for Model A ($C/O = 0.7, ER/vdW = N, a = 0.01, b = 0.4$) with observed abundances $\log X_{\text{obs}}$ in solid black, an order of magnitude difference from the observed abundances $\log X_{\text{obs}} \pm 1$ in dotted black, and the 1σ uncertainties on the observed abundances in gray. The linestyle corresponds to the cosmic ray ionization rate: solid ($\zeta = 10^{-17} \text{ s}^{-1}$), dashed ($\zeta = 10^{-16.5} \text{ s}^{-1}$), and dot-dashed ($\zeta = 10^{-16} \text{ s}^{-1}$), while the color indicates the value of density: blue ($n = 10^5 \text{ cm}^{-3}$), cyan ($n = 10^{4.5} \text{ cm}^{-3}$), and red ($n = 10^4 \text{ cm}^{-3}$).

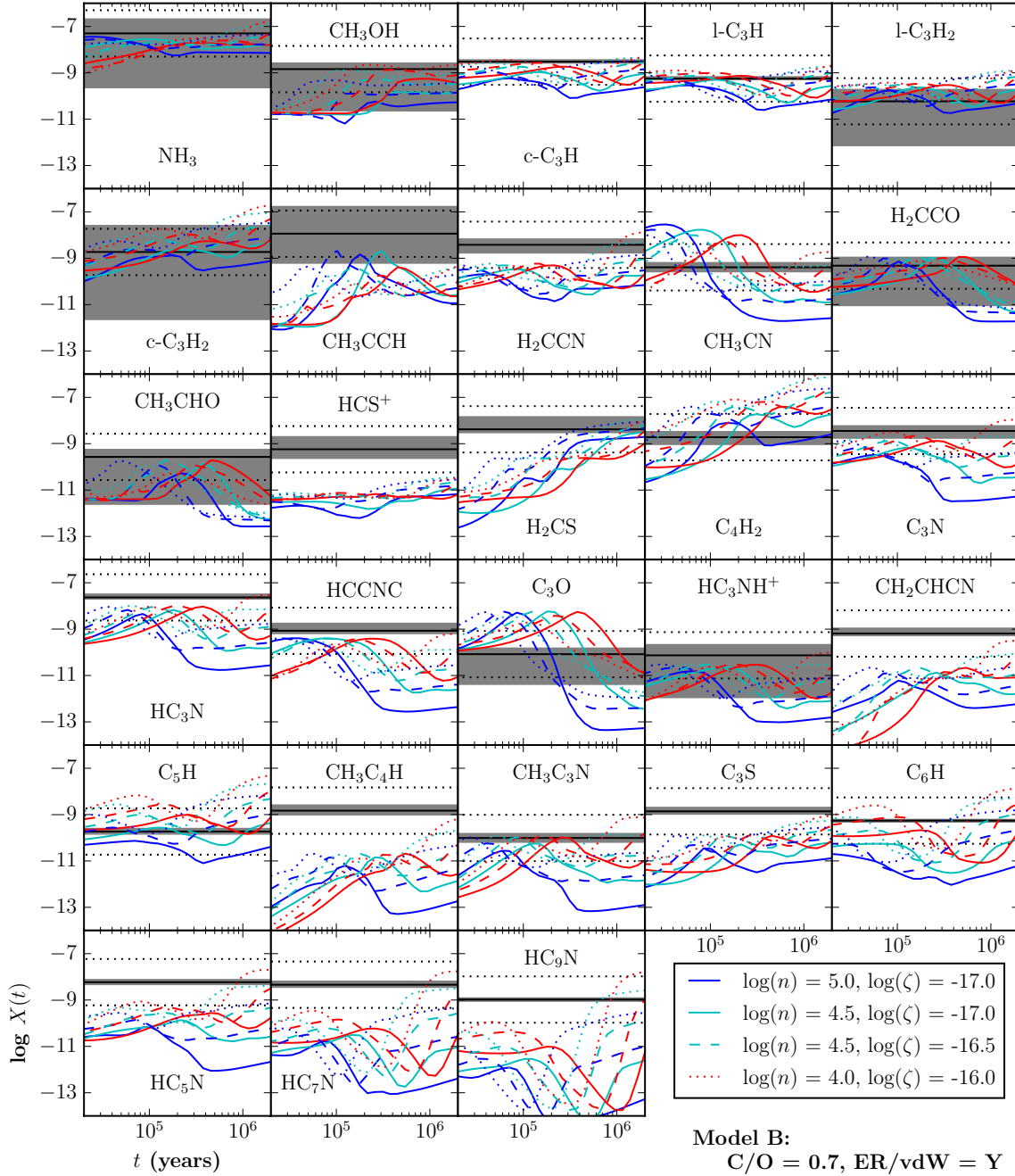


Figure 2.2: Time-dependent abundances $\log X(t)$ for Model B ($C/O = 0.7$, $ER/vdW = Y$, $a = 0.01$, $b = 0.4$) with observed abundances $\log X_{\text{obs}}$ in solid black, an order of magnitude difference from the observed abundances $\log X_{\text{obs}} \pm 1$ in dotted black, and the 1σ uncertainties on the observed abundances in gray. The linestyle corresponds to the cosmic ray ionization rate: solid ($\zeta = 10^{-17} \text{ s}^{-1}$), dashed ($\zeta = 10^{-16.5} \text{ s}^{-1}$), and dot-dashed ($\zeta = 10^{-16} \text{ s}^{-1}$), while the color indicates the value of density: blue ($n = 10^5 \text{ cm}^{-3}$), cyan ($n = 10^{4.5} \text{ cm}^{-3}$), and red ($n = 10^4 \text{ cm}^{-3}$).

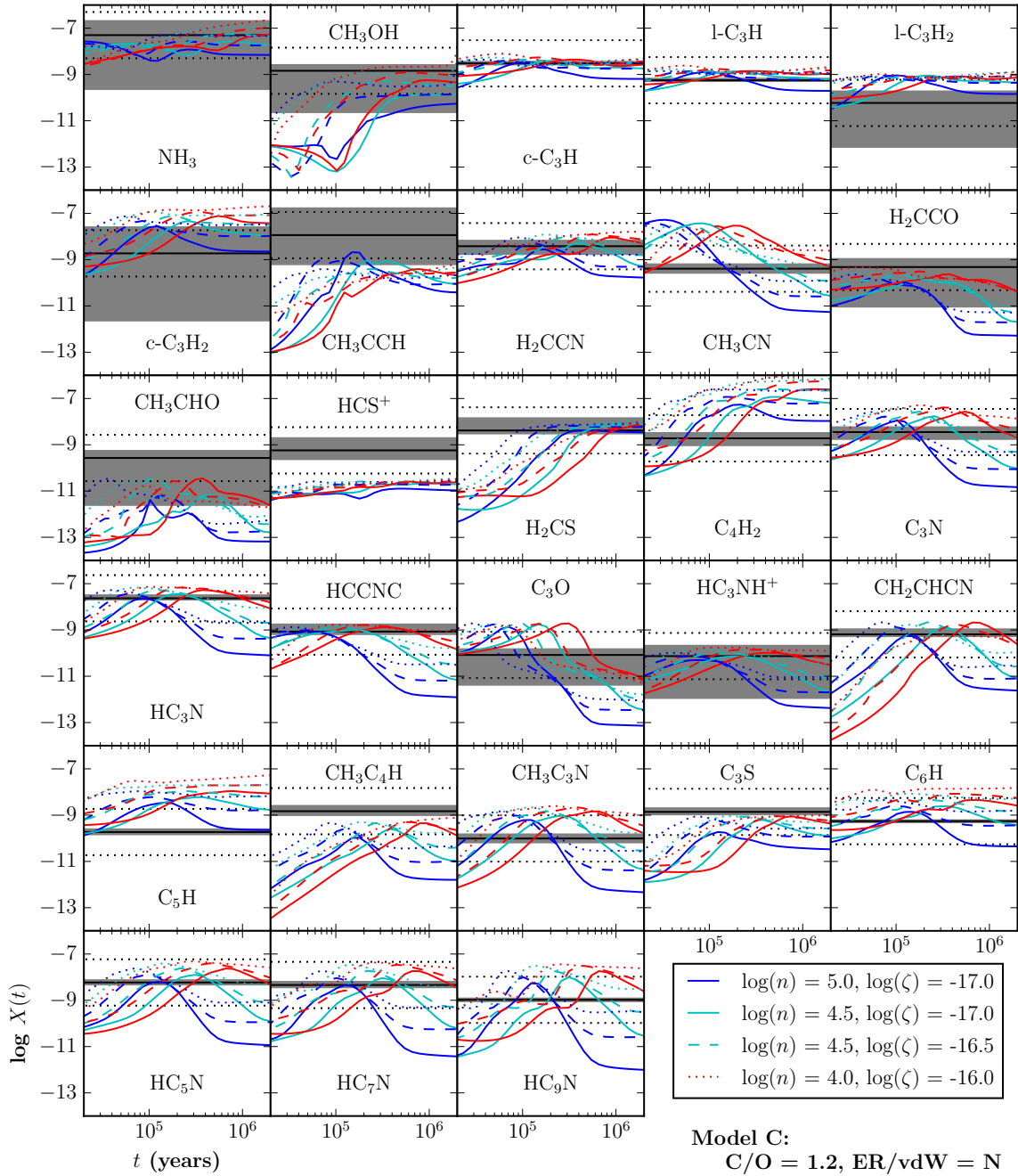


Figure 2.3: Time-dependent abundances $\log X(t)$ for Model C ($C/O = 1.2$, $ER/vdW = N$, $a = 0.01$, $b = 0.4$) with observed abundances $\log X_{\text{obs}}$ in solid black, an order of magnitude difference from the observed abundances $\log X_{\text{obs}} \pm 1$ in dotted black, and the 1σ uncertainties on the observed abundances in gray. The linestyle corresponds to the cosmic ray ionization rate: solid ($\zeta = 10^{-17} \text{ s}^{-1}$), dashed ($\zeta = 10^{-16.5} \text{ s}^{-1}$), and dot-dashed ($\zeta = 10^{-16} \text{ s}^{-1}$), while the color indicates the value of density: blue ($n = 10^5 \text{ cm}^{-3}$), cyan ($n = 10^{4.5} \text{ cm}^{-3}$), and red ($n = 10^4 \text{ cm}^{-3}$).

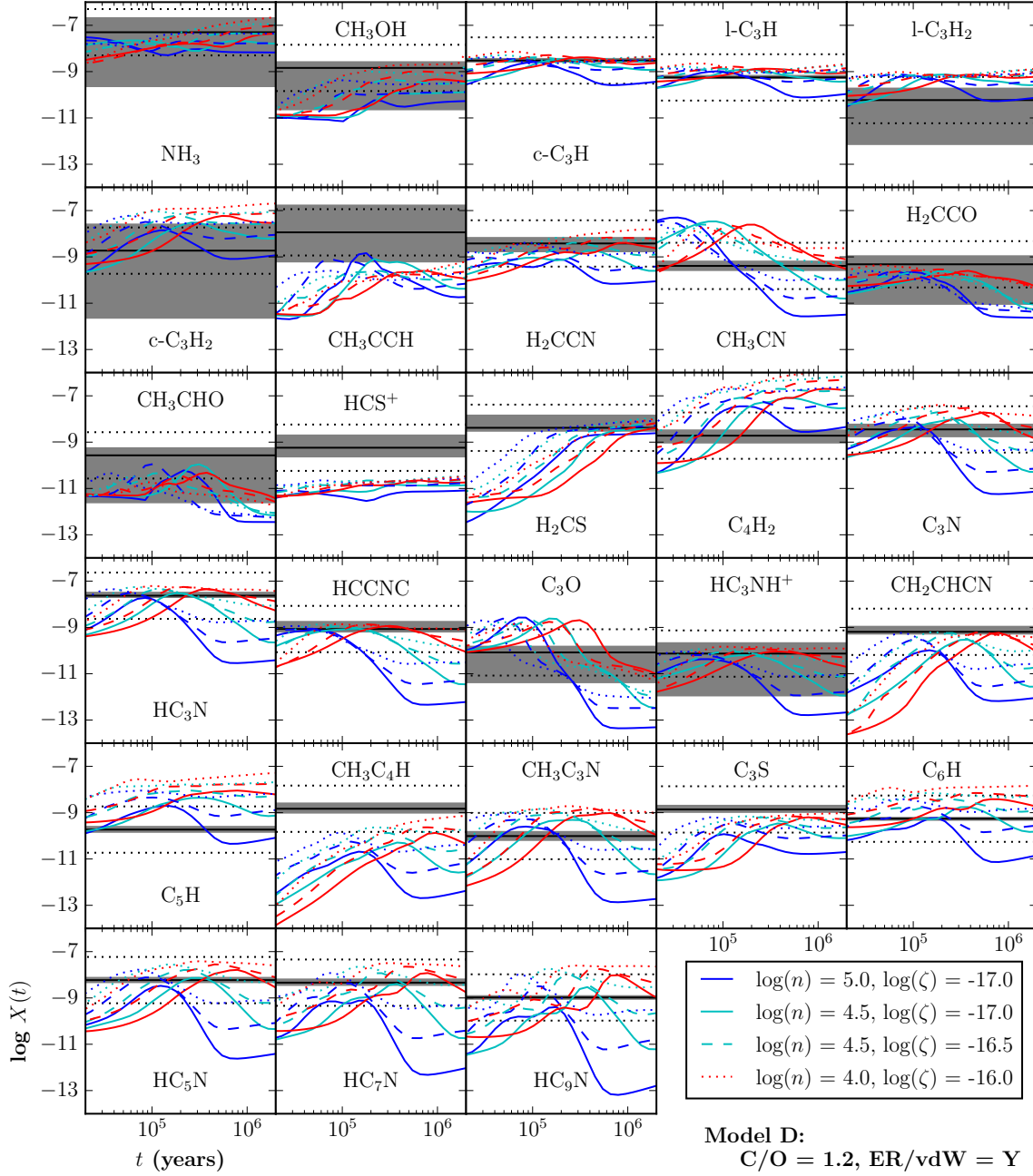


Figure 2.4: Time-dependent abundances $\log X(t)$ for Model D ($C/O = 1.2$, $ER/vdW = Y$, $a = 0.01$, $b = 0.4$) with observed abundances $\log X_{\text{obs}}$ in solid black, an order of magnitude difference from the observed abundances $\log X_{\text{obs}} \pm 1$ in dotted black, and the 1σ uncertainties on the observed abundances in gray. The linestyle corresponds to the cosmic ray ionization rate: solid ($\zeta = 10^{-17} \text{ s}^{-1}$), dashed ($\zeta = 10^{-16.5} \text{ s}^{-1}$), and dot-dashed ($\zeta = 10^{-16} \text{ s}^{-1}$), while the color indicates the value of density: blue ($n = 10^5 \text{ cm}^{-3}$) cyan ($n = 10^{4.5} \text{ cm}^{-3}$), and red ($n = 10^4 \text{ cm}^{-3}$).

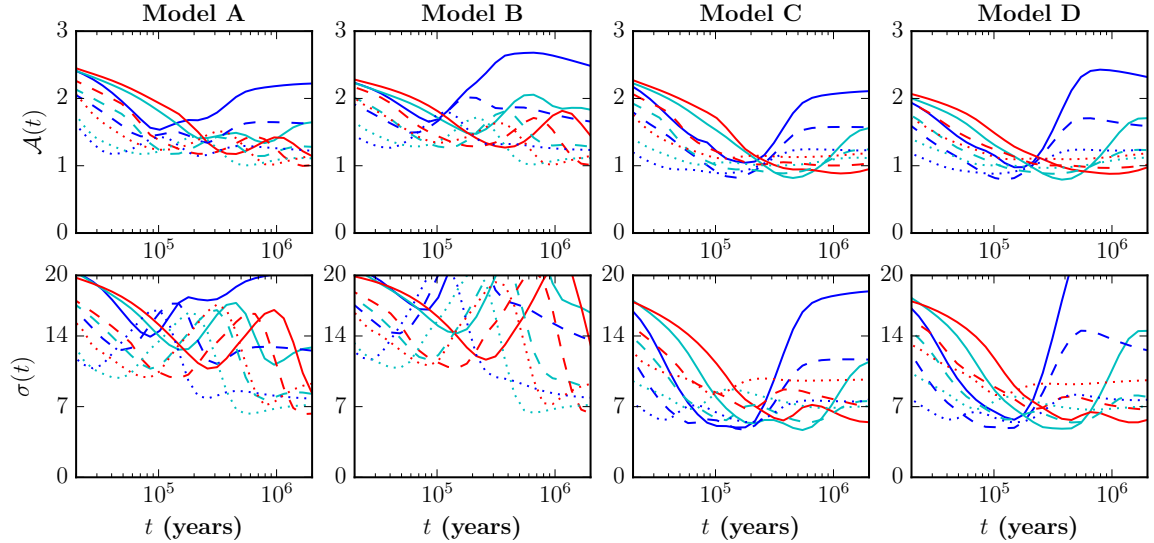


Figure 2.5: Time-dependent rms log abundance differences $\mathcal{A}(t)$ and rms deviations $\sigma(t)$ for Group G and Models A, B, C, and D ($a = 0.01$, $b = 0.4$). The linestyle corresponds to the cosmic ray ionization rate: solid ($\zeta = 10^{-17} \text{ s}^{-1}$), dashed ($\zeta = 10^{-16.5} \text{ s}^{-1}$), and dot-dashed ($\zeta = 10^{-16} \text{ s}^{-1}$), while the color indicates the value of density: blue ($n = 10^5 \text{ cm}^{-3}$), cyan ($n = 10^{4.5} \text{ cm}^{-3}$), and red ($n = 10^4 \text{ cm}^{-3}$).

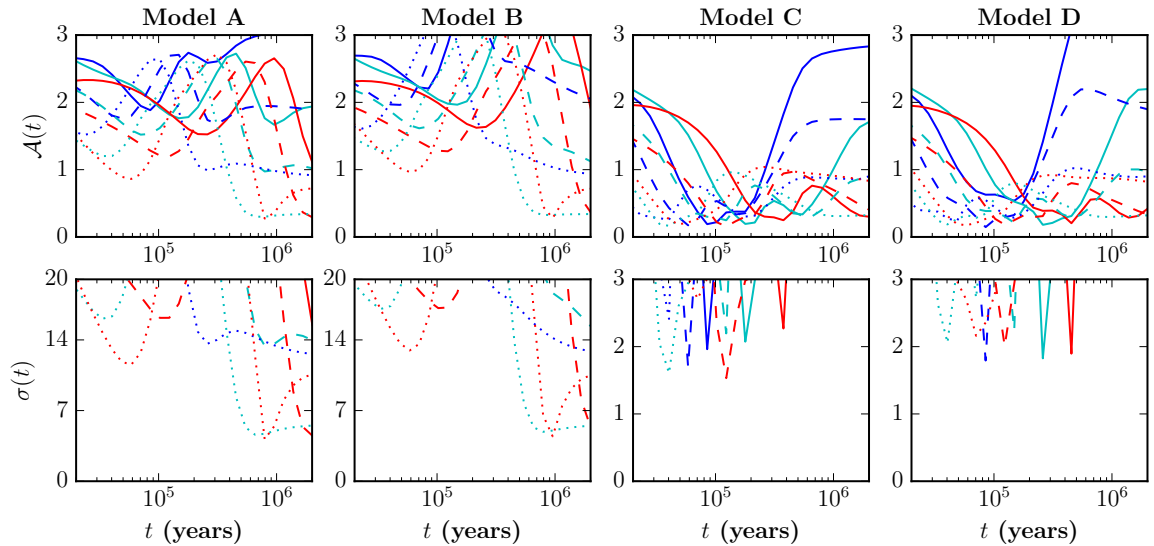


Figure 2.6: Time-dependent rms log abundance differences $\mathcal{A}(t)$ and rms deviations $\sigma(t)$ for Group C and Models A, B, C, and D ($a = 0.01$, $b = 0.4$). The linestyle corresponds to the cosmic ray ionization rate: solid ($\zeta = 10^{-17} \text{ s}^{-1}$), dashed ($\zeta = 10^{-16.5} \text{ s}^{-1}$), and dot-dashed ($\zeta = 10^{-16} \text{ s}^{-1}$), while the color indicates the value of density: blue ($n = 10^5 \text{ cm}^{-3}$), cyan ($n = 10^{4.5} \text{ cm}^{-3}$), and red ($n = 10^4 \text{ cm}^{-3}$).

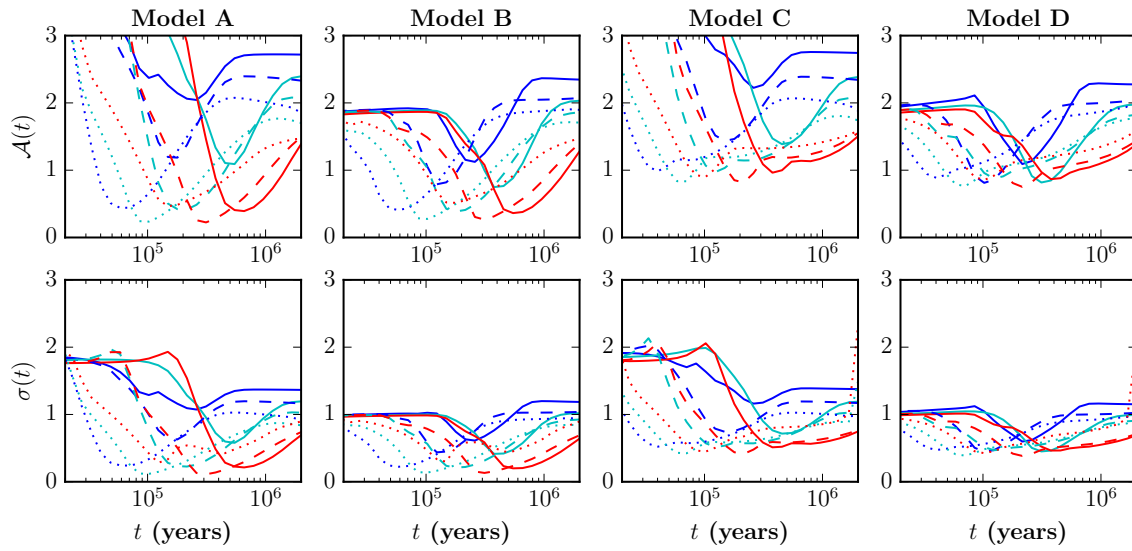


Figure 2.7: Time-dependent rms log abundance differences $\mathcal{A}(t)$ and rms deviations $\sigma(t)$ for Group S and Models A, B, C, and D ($a = 0.01$, $b = 0.4$). The linestyle corresponds to the cosmic ray ionization rate: solid ($\zeta = 10^{-17} \text{ s}^{-1}$), dashed ($\zeta = 10^{-16.5} \text{ s}^{-1}$), and dot-dashed ($\zeta = 10^{-16} \text{ s}^{-1}$), while the color indicates the value of density: blue ($n = 10^5 \text{ cm}^{-3}$), cyan ($n = 10^{4.5} \text{ cm}^{-3}$), and red ($n = 10^4 \text{ cm}^{-3}$).

Table 2.1: Model Parameter Space

Parameter	Value(s)
T_{gas} (K)	10
n (cm^{-3})	$10^5, 10^{4.5}, 10^4$
A_V (mag)	10
ζ (s^{-1})	$10^{-17}, 10^{-16.5}, 10^{-16}$
T_{dust} (K)	10
a	0.01, 0.03, 0.1
b	0.3, 0.4, 0.5

Table 2.2: Fractional Elemental Abundances $f_i = n_i/n_{\text{H}}, n_{\text{H}} = n(\text{H}) + 2n(\text{H}_2)$

Element	Abundance
H ₂	0.5
He	9.0(-2)
O	1.4(-4), 2.4(-4)*
N	6.2(-5)
C ⁺	1.7(-4)
S ⁺	8.0(-8)
Si ⁺	8.0(-9)
Fe ⁺	3.0(-9)
Na ⁺	2.0(-9)
Mg ⁺	7.0(-9)
P ⁺	2.0(-10)
Cl ⁺	1.0(-9)
F	6.68(-9)

* Increasing oxygen abundance corresponds to decreasing oxygen depletion for dark cloud conditions (Hincelin et al., 2011).

Table 2.3: Model Elemental Composition and Reaction Mechanism Spaces

Model	C/O	ER/vdW
A	0.7	N
B	0.7	Y
C	1.2	N
D	1.2	Y

Table 2.4: Relative Molecular Abundances $X_i = N_i/N_{\text{H}}$ and 1σ Uncertainties toward TMC-1 CP (Gratier et al., 2016) for Group(s) M , and Character Type(s) \mathcal{C} for Restricted Grid Models A, B, C, and D

Molecule	$\log(X_i)$	M	$\mathcal{C}(A)$	$\mathcal{C}(B)$	$\mathcal{C}(C)$	$\mathcal{C}(D)$
NH ₃	-7.30 ^{+0.61} _{-2.33}	G	1	1	1	1
CH ₃ OH	-8.84 ^{+0.25} _{-1.79}	G, S	3	3	3	3
c-C ₃ H	-8.52 ^{+0.07} _{-0.05}	G	1	1	1	1
l-C ₃ H	-9.25 ^{+0.07} _{-0.03}	G	1	1	1	1
l-C ₃ H ₂	-10.23 ^{+0.50} _{-1.90}	G	1	1	1	1
c-C ₃ H ₂	-8.73 ^{+1.13} _{-2.90}	G	3	3	2,3	2,3
CH ₃ CCH	-7.94 ^{+1.16} _{-1.26}	G	2	2	2	2
H ₂ CCN	-8.42 ^{+0.24} _{-0.34}	G	1	4	2,3	2,3
CH ₃ CN	-9.39 ^{+0.19} _{-0.18}	G	2	2	2	2
H ₂ CCO	-9.32 ^{+0.35} _{-1.71}	G	2	2	2,3	2,3
CH ₃ CHO	-9.57 ^{+0.31} _{-2.03}	G, S	2	2	2	2
HCS ⁺	-9.24 ^{+0.53} _{-0.38}	G	1	1	1	1
H ₂ CS	-8.38 ^{+0.53} _{-0.13}	G	3	3	3	3
C ₄ H ₂	-8.72 ^{+0.23} _{-0.30}	G	3	2,3	2,3	2,3
C ₃ N	-8.45 ^{+0.21} _{-0.30}	G	1,2,3,4	1,2,3,4	2	2
HC ₃ N	-7.63 ^{+0.13} _{-0.06}	G, C	2	2	2	2
HCCNC	-9.07 ^{+0.31} _{-0.11}	G	2,3,4	2,3,4	2	2
C ₃ O	-10.08 ^{+0.25} _{-1.29}	G	2	2	2	2
HC ₃ NH ⁺	-10.13 ^{+0.45} _{-1.81}	G	2,3,4	2,3,4	2	2
CH ₂ CHCN	-9.19 ^{+0.22} _{-0.08}	G	2,3	2,3	2	2
C ₅ H	-9.73 ^{+0.12} _{-0.10}	G	1,3,4	2,3,4	2,3	2,3
CH ₃ C ₄ H	-8.83 ^{+0.23} _{-0.17}	G	2	4	2,3	2,3
CH ₃ C ₃ N	-10.01 ^{+0.18} _{-0.17}	G	2	2,3,4	2	2
C ₃ S	-8.86 ^{+0.16} _{-0.11}	G	2,3	2,4	2,3	2,3
C ₆ H	-9.26 ^{+0.04} _{-0.05}	G	2	2	2,3	2,3
HC ₅ N	-8.23 ^{+0.10} _{-0.09}	G, C	3,4	4	2,3	2,3
HC ₇ N	-8.34 ^{+0.14} _{-0.10}	G, C	4	4	2,3	2,3
HC ₉ N	-8.98 ^{+0.06} _{-0.06}	G, C	4	4	2,3	2,3

NOTE — Character type $\mathcal{C} = 1$ (inertness), 2 (maximum/minimum), 3 (monotonic increase/decrease), and 4 (oscillatory).

Table 2.5: $\eta = \log(n) - \log(\zeta)$

$\log(\zeta) \setminus \log(n) =$	5	4.5	4
-17	22	21.5	21
-16.5	21.5	21	20.5
-16	21	20.5	20

NOTE — The main diagonal satisfies $\log(n) + \log(\zeta) = -12$

Table 2.6: $\mathcal{A}_{\min}(\mathcal{T})$ and $\log(\mathcal{T})$ for Groups G, C, and S; Model A

db	$\log(\zeta) \setminus \log(n) =$	0.01		0.01		0.03		0.03		0.10		0.10	
		5	4	4.5	4	5	4	4.5	4	5	4.5	4	
0.3	-17	○○○	○○○	○○○	○○●	○○○	○○●	○○○	○○●	○○○	○○○	○○○	○○●
0.3	-16.5	○○○	○○●	○○●	○○●	○○●	○○●	○○●	○○●	○○●	○○●	○○●	○○●
0.3	-16	○○●	○○●	○○●	○○●	○○●	○○●	○○●	○○●	○○●	○○●	○○●	○○●
0.4	17	○○○	○○○	○○○	○○○	○○○	○○○	○○○	○○○	○○○	○○○	○○○	○○○
0.4	-16.5	○○○	○○●	○○●	○○●	○○●	○○●	○○●	○○●	○○●	○○●	○○●	○○●
0.4	-16	○○●	○○●	○○●	○○●	○○●	○○●	○○●	○○●	○○●	○○●	○○●	○○●
0.5	-17	○○○	○○○	○○○	○○○	○○○	○○○	○○○	○○○	○○○	○○○	○○○	○○○
0.5	-16.5	○○○	○○●	○○●	○○●	○○●	○○●	○○●	○○●	○○●	○○●	○○●	○○●
0.5	-16	○○●	○○●	○○●	○○●	○○●	○○●	○○●	○○●	○○●	○○●	○○●	○○●
0.3	-17	○○○	○○○	○○○	○○●	○○○	○○○	○○○	○○○	○○○	○○○	○○○	○○○
0.3	-16.5	○○○	○○○	○○○	○○○	○○○	○○○	○○○	○○○	○○○	○○○	○○○	○○○
0.3	-16	○○○	○○○	○○○	○○○	○○○	○○○	○○○	○○○	○○○	○○○	○○○	○○○
0.4	17	○○○	○○○	○○○	○○○	○○○	○○○	○○○	○○○	○○○	○○○	○○○	○○○
0.4	-16.5	○○○	○○○	○○○	○○○	○○○	○○○	○○○	○○○	○○○	○○○	○○○	○○○
0.4	-16	○○○	○○○	○○○	○○○	○○○	○○○	○○○	○○○	○○○	○○○	○○○	○○○
0.5	-17	○○○	○○○	○○○	○○○	○○○	○○○	○○○	○○○	○○○	○○○	○○○	○○○
0.5	-16.5	○○○	○○○	○○○	○○○	○○○	○○○	○○○	○○○	○○○	○○○	○○○	○○○
0.5	-16	○○○	○○○	○○○	○○○	○○○	○○○	○○○	○○○	○○○	○○○	○○○	○○○

NOTE — Upper nine blocks: $\mathcal{A}_{\min} > 1$ (open, ○), $1 \geq \mathcal{A}_{\min} \geq 0.5$ (dotted, ◐), $\mathcal{A}_{\min} < 0.5$ (closed, ●); lower nine blocks: $\log(\mathcal{T}) < 5$ (crescent, ☾), $5 < \log(\mathcal{T}) < 6$ (open, ○), $6 < \log(\mathcal{T}) < 7$ (dotted, ◐), $\log(\mathcal{T}) > 7$ (closed, ●)

Table 2.7: $\mathcal{A}_{\min}(\mathcal{T})$ and $\log(\mathcal{T})$ for Groups G, C, and S; Model B

db	$\log(\zeta) \setminus \log(n) =$	0.01		0.01		0.03		0.03		0.10		0.10	
		5	4	4.5	4	5	4	4.5	4	5	4.5	4	
0.3	-17	○○	○○○	○○○	○○○	○○○	○○○	○○○	○○○	○○○	○○○	○○○	○○○
0.3	-16.5	○○○	○○○	○○○	○○○	○○○	○○○	○○○	○○○	○○○	○○○	○○○	○○○
0.3	-16	○○○	○○○	○○○	○○○	○○○	○○○	○○○	○○○	○○○	○○○	○○○	○○○
0.4	17	○○○	○○○	○○○	○○○	○○○	○○○	○○○	○○○	○○○	○○○	○○○	○○○
0.4	-16.5	○○○	○○○	○○○	○○○	○○○	○○○	○○○	○○○	○○○	○○○	○○○	○○○
0.4	-16	○○○	○○○	○○○	○○○	○○○	○○○	○○○	○○○	○○○	○○○	○○○	○○○
0.5	-17	○○○	○○○	○○○	○○○	○○○	○○○	○○○	○○○	○○○	○○○	○○○	○○○
0.5	-16.5	○○○	○○○	○○○	○○○	○○○	○○○	○○○	○○○	○○○	○○○	○○○	○○○
0.5	-16	○○○	○○○	○○○	○○○	○○○	○○○	○○○	○○○	○○○	○○○	○○○	○○○
0.3	-17	⊕⊕	⊕⊕	⊕⊕	⊕⊕	⊕⊕	⊕⊕	⊕⊕	⊕⊕	⊕⊕	⊕⊕	⊕⊕	⊕⊕
0.3	-16.5	⊕⊕	⊕⊕	⊕⊕	⊕⊕	⊕⊕	⊕⊕	⊕⊕	⊕⊕	⊕⊕	⊕⊕	⊕⊕	⊕⊕
0.3	-16	⊕⊕	⊕⊕	⊕⊕	⊕⊕	⊕⊕	⊕⊕	⊕⊕	⊕⊕	⊕⊕	⊕⊕	⊕⊕	⊕⊕
0.4	17	⊕⊕	⊕⊕	⊕⊕	⊕⊕	⊕⊕	⊕⊕	⊕⊕	⊕⊕	⊕⊕	⊕⊕	⊕⊕	⊕⊕
0.4	-16.5	⊕⊕	⊕⊕	⊕⊕	⊕⊕	⊕⊕	⊕⊕	⊕⊕	⊕⊕	⊕⊕	⊕⊕	⊕⊕	⊕⊕
0.4	-16	⊕⊕	⊕⊕	⊕⊕	⊕⊕	⊕⊕	⊕⊕	⊕⊕	⊕⊕	⊕⊕	⊕⊕	⊕⊕	⊕⊕
0.5	-17	⊕⊕	⊕⊕	⊕⊕	⊕⊕	⊕⊕	⊕⊕	⊕⊕	⊕⊕	⊕⊕	⊕⊕	⊕⊕	⊕⊕
0.5	-16.5	⊕⊕	⊕⊕	⊕⊕	⊕⊕	⊕⊕	⊕⊕	⊕⊕	⊕⊕	⊕⊕	⊕⊕	⊕⊕	⊕⊕
0.5	-16	⊕⊕	⊕⊕	⊕⊕	⊕⊕	⊕⊕	⊕⊕	⊕⊕	⊕⊕	⊕⊕	⊕⊕	⊕⊕	⊕⊕

NOTE — Upper nine blocks: $\mathcal{A}_{\min} > 1$ (open, ○), $1 \geq \mathcal{A}_{\min} \geq 0.5$ (dotted, ⊕), $\mathcal{A}_{\min} < 0.5$ (closed, ●); lower nine blocks: $\log(\mathcal{T}) < 5$ (crescent, ⊕), $5 < \log(\mathcal{T}) < 6$ (open, ○), $6 < \log(\mathcal{T}) < 7$ (dotted, ⊕), $\log(\mathcal{T}) > 7$ (closed, ●)

Table 2.8: $\mathcal{A}_{\min}(\mathcal{T})$ and $\log(\mathcal{T})$ for Groups G, C, and S; Model C

db	$\log(\zeta) \setminus \log(n) =$	0.01		0.01		0.03		0.03		0.10		0.10	
		5	4	4.5	4	5	4.5	4	5	4.5	5	4.5	4
0.3	-17	○	○	○	○	○	○	○	○	○	○	○	○
0.3	-16.5	○	○	○	○	○	○	○	○	○	○	○	○
0.3	-16	○	○	○	○	○	○	○	○	○	○	○	○
0.4	17	○	○	○	○	○	○	○	○	○	○	○	○
0.4	-16.5	○	○	○	○	○	○	○	○	○	○	○	○
0.4	-16	○	○	○	○	○	○	○	○	○	○	○	○
0.5	-17	○	○	○	○	○	○	○	○	○	○	○	○
0.5	-16.5	○	○	○	○	○	○	○	○	○	○	○	○
0.5	-16	○	○	○	○	○	○	○	○	○	○	○	○
0.3	-17	○	○	○	○	○	○	○	○	○	○	○	○
0.3	-16.5	○	○	○	○	○	○	○	○	○	○	○	○
0.3	-16	○	○	○	○	○	○	○	○	○	○	○	○
0.4	17	○	○	○	○	○	○	○	○	○	○	○	○
0.4	-16.5	○	○	○	○	○	○	○	○	○	○	○	○
0.4	-16	○	○	○	○	○	○	○	○	○	○	○	○
0.5	-17	○	○	○	○	○	○	○	○	○	○	○	○
0.5	-16.5	○	○	○	○	○	○	○	○	○	○	○	○
0.5	-16	○	○	○	○	○	○	○	○	○	○	○	○

NOTE — Upper nine blocks: $\mathcal{A}_{\min} > 1$ (open, ○), $1 \geq \mathcal{A}_{\min} \geq 0.5$ (dotted, ◐), $\mathcal{A}_{\min} < 0.5$ (closed, ●); lower nine blocks: $\log(\mathcal{T}) < 5$ (crescent, ☾), $5 < \log(\mathcal{T}) < 6$ (open, ○), $6 < \log(\mathcal{T}) < 7$ (dotted, ◐), $\log(\mathcal{T}) > 7$ (closed, ●)

Table 2.9: $\mathcal{A}_{\min}(\mathcal{T})$ and $\log(\mathcal{T})$ for Groups G, C, and S; Model D

db	$\log(\zeta) \setminus \log(n) =$	0.01		0.01		0.03		0.03		0.10		0.10	
		5	4	4.5	4	5	4.5	4	5	4.5	4		
0.3	-17	⊙●	⊙●	⊙●	⊙●	⊙●	⊙●	⊙●	⊙●	⊙●	⊙●	⊙●	⊙●
0.3	-16.5	⊙●	⊙●	⊙●	⊙●	⊙●	⊙●	⊙●	⊙●	⊙●	⊙●	⊙●	⊙●
0.3	-16	⊙●	⊙●	⊙●	⊙●	⊙●	⊙●	⊙●	⊙●	⊙●	⊙●	⊙●	⊙●
0.4	17	⊙●	⊙●	⊙●	⊙●	⊙●	⊙●	⊙●	⊙●	⊙●	⊙●	⊙●	⊙●
0.4	-16.5	⊙●	⊙●	⊙●	⊙●	⊙●	⊙●	⊙●	⊙●	⊙●	⊙●	⊙●	⊙●
0.4	-16	⊙●	⊙●	⊙●	⊙●	⊙●	⊙●	⊙●	⊙●	⊙●	⊙●	⊙●	⊙●
0.5	-17	⊙●	⊙●	⊙●	⊙●	⊙●	⊙●	⊙●	⊙●	⊙●	⊙●	⊙●	⊙●
0.5	-16.5	⊙●	⊙●	⊙●	⊙●	⊙●	⊙●	⊙●	⊙●	⊙●	⊙●	⊙●	⊙●
0.5	-16	⊙●	⊙●	⊙●	⊙●	⊙●	⊙●	⊙●	⊙●	⊙●	⊙●	⊙●	⊙●
0.3	-17	○○	○○	○○	○○	○○	○○	○○	○○	○○	○○	○○	○○
0.3	-16.5	○○	○○	○○	○○	○○	○○	○○	○○	○○	○○	○○	○○
0.3	-16	○○	○○	○○	○○	○○	○○	○○	○○	○○	○○	○○	○○
0.4	17	○○	○○	○○	○○	○○	○○	○○	○○	○○	○○	○○	○○
0.4	-16.5	○○	○○	○○	○○	○○	○○	○○	○○	○○	○○	○○	○○
0.4	-16	○○	○○	○○	○○	○○	○○	○○	○○	○○	○○	○○	○○
0.5	-17	○○	○○	○○	○○	○○	○○	○○	○○	○○	○○	○○	○○
0.5	-16.5	○○	○○	○○	○○	○○	○○	○○	○○	○○	○○	○○	○○
0.5	-16	○○	○○	○○	○○	○○	○○	○○	○○	○○	○○	○○	○○

NOTE — Upper nine blocks: $\mathcal{A}_{\min} > 1$ (open, ○), $1 \geq \mathcal{A}_{\min} \geq 0.5$ (dotted, ⊙), $\mathcal{A}_{\min} < 0.5$ (closed, ●); lower nine blocks: $\log(\mathcal{T}) < 5$ (crescent, ☾), $5 < \log(\mathcal{T}) < 6$ (open, ○), $6 < \log(\mathcal{T}) < 7$ (dotted, ⊙), $\log(\mathcal{T}) > 7$ (closed, ●)

Table 2.10: $\sigma_{\min}(\mathcal{T})$ and $\log(\mathcal{T})$ for Groups G, C, and S; Model A

db	$\log(\zeta) \setminus \log(n) =$	0.01		0.01		0.03		0.03		0.10		0.10	
		5	4	4.5	4	5	4	4.5	4	5	4.5	4	
0.3	-17	○○○	○○○	○○○	○○●	○○○	○○●	○○○	○○●	○○○	○○●	○○○	○○●
0.3	-16.5	○○○	○○○	○○○	○○●	○○○	○○●	○○○	○○●	○○○	○○●	○○○	○○●
0.3	-16	○○○	○○○	○○○	○○●	○○○	○○●	○○○	○○●	○○○	○○●	○○○	○○●
0.4	17	○○○	○○○	○○○	○○○	○○○	○○○	○○○	○○○	○○○	○○○	○○○	○○○
0.4	-16.5	○○○	○○○	○○○	○○○	○○○	○○○	○○○	○○○	○○○	○○○	○○○	○○○
0.4	-16	○○○	○○○	○○○	○○○	○○○	○○○	○○○	○○○	○○○	○○○	○○○	○○○
0.5	-17	○○○	○○○	○○○	○○○	○○○	○○○	○○○	○○○	○○○	○○○	○○○	○○○
0.5	-16.5	○○○	○○○	○○○	○○○	○○○	○○○	○○○	○○○	○○○	○○○	○○○	○○○
0.5	-16	○○○	○○○	○○○	○○○	○○○	○○○	○○○	○○○	○○○	○○○	○○○	○○○
0.3	-17	⊕⊕⊕	●●●	●●●	●●●	⊕⊕⊕	●●●	●●●	●●●	⊕⊕⊕	●●●	●●●	●●●
0.3	-16.5	⊕⊕⊕	⊕⊕⊕	⊕⊕⊕	⊕⊕○	⊕⊕○	⊕⊕○	⊕⊕○	⊕⊕○	⊕⊕○	⊕⊕○	⊕⊕○	⊕⊕○
0.3	-16	⊕⊕⊕	⊕⊕⊕	⊕⊕⊕	⊕⊕○	⊕⊕○	⊕⊕○	⊕⊕○	⊕⊕○	⊕⊕○	⊕⊕○	⊕⊕○	⊕⊕○
0.4	17	⊕⊕⊕	⊕⊕⊕	⊕⊕⊕	●●●	●●●	●●●	●●●	●●●	⊕⊕⊕	●●●	●●●	●●●
0.4	-16.5	⊕⊕⊕	⊕⊕○	⊕⊕○	⊕⊕○	⊕⊕○	⊕⊕○	⊕⊕○	⊕⊕○	⊕⊕○	⊕⊕○	⊕⊕○	⊕⊕○
0.4	-16	⊕⊕⊕	⊕⊕⊕	⊕⊕⊕	⊕⊕○	⊕⊕○	⊕⊕○	⊕⊕○	⊕⊕○	⊕⊕○	⊕⊕○	⊕⊕○	⊕⊕○
0.5	-17	⊕⊕⊕	⊕⊕⊕	⊕⊕⊕	⊕⊕○	⊕⊕○	⊕⊕○	⊕⊕○	⊕⊕○	⊕⊕○	⊕⊕○	⊕⊕○	⊕⊕○
0.5	-16.5	⊕⊕⊕	⊕⊕○	⊕⊕○	⊕⊕○	⊕⊕○	⊕⊕○	⊕⊕○	⊕⊕○	⊕⊕○	⊕⊕○	⊕⊕○	⊕⊕○
0.5	-16	⊕⊕⊕	⊕⊕⊕	⊕⊕⊕	⊕⊕○	⊕⊕○	⊕⊕○	⊕⊕○	⊕⊕○	⊕⊕○	⊕⊕○	⊕⊕○	⊕⊕○

NOTE — Upper nine blocks: $\sigma_{\min} > 1$ (open, ○), $1 \geq \sigma_{\min} \geq 0.5$ (dotted, ⊕), $\sigma_{\min} < 0.5$ (closed, ●);
lower nine blocks: $\log(\mathcal{T}) < 5$ (crescent, ⊕), $5 < \log(\mathcal{T}) < 6$ (open, ○), $6 < \log(\mathcal{T}) < 7$ (dotted, ⊕),
 $\log(\mathcal{T}) > 7$ (closed, ●)

Table 2.11: $\sigma_{\min}(\mathcal{T})$ and $\log(\mathcal{T})$ for Groups G, C, and S; Model B

db	$\log(\zeta) \setminus \log(n) =$	0.01		0.01		0.03		0.03		0.10		0.10	
		5	4	4.5	4	5	4.5	4	5	4.5	4		
0.3	-17	○○○	○○●	○○●	○○●	○○●	○○●	○○●	○○●	○○●	○○●	○○●	○○●
0.3	-16.5	○○●	○○●	○○●	○○●	○○●	○○●	○○●	○○●	○○●	○○●	○○●	○○●
0.3	-16	○○●	○○●	○○●	○○●	○○●	○○●	○○●	○○●	○○●	○○●	○○●	○○●
0.4	17	○○○	○○●	○○●	○○●	○○●	○○●	○○●	○○●	○○●	○○●	○○●	○○●
0.4	-16.5	○○●	○○●	○○●	○○●	○○●	○○●	○○●	○○●	○○●	○○●	○○●	○○●
0.4	-16	○○●	○○●	○○●	○○●	○○●	○○●	○○●	○○●	○○●	○○●	○○●	○○●
0.5	-17	○○○	○○●	○○●	○○●	○○●	○○●	○○●	○○●	○○●	○○●	○○●	○○●
0.5	-16.5	○○●	○○●	○○●	○○●	○○●	○○●	○○●	○○●	○○●	○○●	○○●	○○●
0.5	-16	○○●	○○●	○○●	○○●	○○●	○○●	○○●	○○●	○○●	○○●	○○●	○○●
0.3	-17	⊕⊕○	●●○	●●○	●●○	●●○	●●○	●●○	●●○	●●○	●●○	●●○	●●○
0.3	-16.5	⊕⊕○	⊕⊕○	⊕⊕○	⊕⊕○	⊕⊕○	⊕⊕○	⊕⊕○	⊕⊕○	⊕⊕○	⊕⊕○	⊕⊕○	⊕⊕○
0.3	-16	⊕⊕⊕	○○○	○○○	○○○	○○○	○○○	○○○	○○○	○○○	○○○	○○○	○○○
0.4	17	⊕⊕○	●●○	●●○	●●○	●●○	●●○	●●○	●●○	●●○	●●○	●●○	●●○
0.4	-16.5	⊕⊕○	⊕⊕○	⊕⊕○	⊕⊕○	⊕⊕○	⊕⊕○	⊕⊕○	⊕⊕○	⊕⊕○	⊕⊕○	⊕⊕○	⊕⊕○
0.4	-16	⊕⊕⊕	○○○	○○○	○○○	○○○	○○○	○○○	○○○	○○○	○○○	○○○	○○○
0.5	-17	⊕⊕○	●●○	●●○	●●○	●●○	●●○	●●○	●●○	●●○	●●○	●●○	●●○
0.5	-16.5	⊕⊕○	⊕⊕○	⊕⊕○	⊕⊕○	⊕⊕○	⊕⊕○	⊕⊕○	⊕⊕○	⊕⊕○	⊕⊕○	⊕⊕○	⊕⊕○
0.5	-16	⊕⊕⊕	○○○	○○○	○○○	○○○	○○○	○○○	○○○	○○○	○○○	○○○	○○○

NOTE — Upper nine blocks: $\sigma_{\min} > 1$ (open, ○), $1 \geq \sigma_{\min} \geq 0.5$ (dotted, ⊕), $\sigma_{\min} < 0.5$ (closed, ●); lower nine blocks: $\log(\mathcal{T}) < 5$ (crescent, ⊕), $5 < \log(\mathcal{T}) < 6$ (open, ○), $6 < \log(\mathcal{T}) < 7$ (dotted, ⊕), $\log(\mathcal{T}) > 7$ (closed, ●)

Table 2.12: $\sigma_{\min}(\mathcal{T})$ and $\log(\mathcal{T})$ for Groups G, C, and S; Model C

db	$\log(\zeta) \setminus \log(n) =$	0.01		0.01		0.03		0.03		0.10		0.10	
		5	4	4.5	4	5	4.5	4	5	4.5	4		
0.3	-17	○○○	○○○	○○○	○○○	○○○	○○○	○○○	○○○	○○○	○○○	○○○	○○○
0.3	-16.5	○○○	○○○	○○○	○○○	○○○	○○○	○○○	○○○	○○○	○○○	○○○	○○○
0.3	-16	○○○	○○○	○○○	○○○	○○○	○○○	○○○	○○○	○○○	○○○	○○○	○○○
0.4	17	○○○	○○○	○○○	○○○	○○○	○○○	○○○	○○○	○○○	○○○	○○○	○○○
0.4	-16.5	○○○	○○○	○○○	○○○	○○○	○○○	○○○	○○○	○○○	○○○	○○○	○○○
0.4	-16	○○○	○○○	○○○	○○○	○○○	○○○	○○○	○○○	○○○	○○○	○○○	○○○
0.5	-17	○○○	○○○	○○○	○○○	○○○	○○○	○○○	○○○	○○○	○○○	○○○	○○○
0.5	-16.5	○○○	○○○	○○○	○○○	○○○	○○○	○○○	○○○	○○○	○○○	○○○	○○○
0.5	-16	○○○	○○○	○○○	○○○	○○○	○○○	○○○	○○○	○○○	○○○	○○○	○○○
0.3	-17	○○○	○○○	○○○	○○○	○○○	○○○	○○○	○○○	○○○	○○○	○○○	○○○
0.3	-16.5	○○○	○○○	○○○	○○○	○○○	○○○	○○○	○○○	○○○	○○○	○○○	○○○
0.3	-16	○○○	○○○	○○○	○○○	○○○	○○○	○○○	○○○	○○○	○○○	○○○	○○○
0.4	17	○○○	○○○	○○○	○○○	○○○	○○○	○○○	○○○	○○○	○○○	○○○	○○○
0.4	-16.5	○○○	○○○	○○○	○○○	○○○	○○○	○○○	○○○	○○○	○○○	○○○	○○○
0.4	-16	○○○	○○○	○○○	○○○	○○○	○○○	○○○	○○○	○○○	○○○	○○○	○○○
0.5	-17	○○○	○○○	○○○	○○○	○○○	○○○	○○○	○○○	○○○	○○○	○○○	○○○
0.5	-16.5	○○○	○○○	○○○	○○○	○○○	○○○	○○○	○○○	○○○	○○○	○○○	○○○
0.5	-16	○○○	○○○	○○○	○○○	○○○	○○○	○○○	○○○	○○○	○○○	○○○	○○○

NOTE — Upper nine blocks: $\sigma_{\min} > 1$ (open, ○), $1 \geq \sigma_{\min} \geq 0.5$ (dotted, ⊙), $\sigma_{\min} < 0.5$ (closed, ●);
lower nine blocks: $\log(\mathcal{T}) < 5$ (crescent, ☾), $5 < \log(\mathcal{T}) < 6$ (open, ○), $6 < \log(\mathcal{T}) < 7$ (dotted, ⊙),
 $\log(\mathcal{T}) > 7$ (closed, ●)

Table 2.13: $\sigma_{\min}(\mathcal{T})$ and $\log(\mathcal{T})$ for Groups G, C, and S; Model D

db	$\log(\zeta) \setminus \log(n) =$	$a =$		0.01		0.01		0.03		0.03		0.10		0.10	
		5	4	4.5	4	5	4.5	4	5	4.5	4	5	4.5	4	
0.3	-17	○○○	○○●	○○●	○○●	○○●	○○●	○○●	○○●	○○●	○○●	○○●	○○●	○○●	○○●
0.3	-16.5	○○●	○○●	○○●	○○●	○○●	○○●	○○●	○○●	○○●	○○●	○○●	○○●	○○●	○○●
0.3	-16	○○●	○○●	○○●	○○●	○○●	○○●	○○●	○○●	○○●	○○●	○○●	○○●	○○●	○○●
0.4	17	○○○	○○●	○○●	○○●	○○●	○○●	○○●	○○●	○○●	○○●	○○●	○○●	○○●	○○●
0.4	-16.5	○○●	○○●	○○●	○○●	○○●	○○●	○○●	○○●	○○●	○○●	○○●	○○●	○○●	○○●
0.4	-16	○○●	○○●	○○●	○○●	○○●	○○●	○○●	○○●	○○●	○○●	○○●	○○●	○○●	○○●
0.5	-17	○○○	○○●	○○●	○○●	○○●	○○●	○○●	○○●	○○●	○○●	○○●	○○●	○○●	○○●
0.5	-16.5	○○●	○○●	○○●	○○●	○○●	○○●	○○●	○○●	○○●	○○●	○○●	○○●	○○●	○○●
0.5	-16	○○●	○○●	○○●	○○●	○○●	○○●	○○●	○○●	○○●	○○●	○○●	○○●	○○●	○○●
0.3	-17	○○○	○○○	○○○	○○○	○○○	○○○	○○○	○○○	○○○	○○○	○○○	○○○	○○○	○○○
0.3	-16.5	○○○	○○○	○○○	○○○	○○○	○○○	○○○	○○○	○○○	○○○	○○○	○○○	○○○	○○○
0.3	-16	○○○	○○○	○○○	○○○	○○○	○○○	○○○	○○○	○○○	○○○	○○○	○○○	○○○	○○○
0.4	17	○○○	○○○	○○○	○○○	○○○	○○○	○○○	○○○	○○○	○○○	○○○	○○○	○○○	○○○
0.4	-16.5	○○○	○○○	○○○	○○○	○○○	○○○	○○○	○○○	○○○	○○○	○○○	○○○	○○○	○○○
0.4	-16	○○○	○○○	○○○	○○○	○○○	○○○	○○○	○○○	○○○	○○○	○○○	○○○	○○○	○○○
0.5	-17	○○○	○○○	○○○	○○○	○○○	○○○	○○○	○○○	○○○	○○○	○○○	○○○	○○○	○○○
0.5	-16.5	○○○	○○○	○○○	○○○	○○○	○○○	○○○	○○○	○○○	○○○	○○○	○○○	○○○	○○○
0.5	-16	○○○	○○○	○○○	○○○	○○○	○○○	○○○	○○○	○○○	○○○	○○○	○○○	○○○	○○○

NOTE — Upper nine blocks: $\sigma_{\min} > 1$ (open, ○), $1 \geq \sigma_{\min} \geq 0.5$ (dotted, ⊙), $\sigma_{\min} < 0.5$ (closed, ●);
 lower nine blocks: $\log(\mathcal{T}) < 5$ (crescent, ☾), $5 < \log(\mathcal{T}) < 6$ (open, ○), $6 < \log(\mathcal{T}) < 7$ (dotted, ⊙),
 $\log(\mathcal{T}) > 7$ (closed, ●)

CHAPTER 3

DIFFUSE AND TRANSLUCENT CLOUDS: SAGITTARIUS B2

The abundances of sulfur-bearing species sulfur monoxide SO, carbon monosulfide CS, dicarbon monosulfide CCS, the thioformyl cation HCS⁺, and thioformaldehyde H₂CS traced by cyclopropenylidene *c*-C₃H₂ have been calculated using the absorption spectra in the PRIMOS data collected by the Green Bank Telescope (GBT) along the line of sight to Sagittarius B2 North, Sgr B2(N). Using a three-phase rate equation approach, we construct grids of chemical kinetic models with combinations of free parameters spanning the physical conditions characteristic of both spiral arm and Galactic center translucent molecular clouds to model four of the identified absorbing kinematic components ($v = -23, -40, -73, \text{ and } -106 \text{ km s}^{-1}$). We calculate the root-mean-square (rms) logarithm differences $\mathcal{A}(p, t)$ between the modeled and observed abundances as well as the correlation coefficients $r(p, t)$ at all times and combinations of free parameters in the grid models to characterize each cloud. We record the chemical timescales as the best fit times for fiducial models of each kinematic component, determine the optimized free parameters by finding global minima \mathcal{A}_{min} within the grid models for each kinematic component, and determine the minimum solution space in the grid models for each set of abundances. The results of this method separate the effect varying each free parameter in the kinetic model has on the time-dependent abundances and constrains the parameter space to combinations that accurately reproduce the abundances of the observed species.

3.1 INTRODUCTION

Sagittarius B2 (Sgr B2) is a giant molecular cloud complex of $10^7 M_{\odot}$ (Lis and Goldsmith, 1990) located 8.34 ± 0.16 kpc from the Sun (Reid et al., 2014) that extends across 40 pc (Lis and Goldsmith, 1990) and has a projected distance from the Galactic Center Sagittarius A* of $43.4'$ or 107 pc (Schmiedeke et al., 2016). Molecular line surveys conducted along the line of sight toward Sgr B2 reveal the absorption spectra of myriad molecular constituents in multiple kinematic components including the 3

kpc arm for velocities $v = -55$ to -35 km/s, the 4 kpc arm for velocities $v = -35$ to -10 km/s as well as Galactic Center clouds within 1 kpc of the Galactic Center for velocities $v = -130$ to -55 km/s (Whiteoak and Gardner, 1979; Wirström et al., 2010). These kinematic components are believed to be associated with molecular gas characterized by the translucent cloud conditions of low visual extinctions $1 < A_V < 2.5$, temperatures $15 < T < 30$ K slightly warmer than dark clouds, and densities $n \leq 10^4$ cm $^{-3}$ (Greaves and Nyman, 1996; Snow and McCall, 2006; Corby et al., 2018; Thiel et al., 2019).

State-of-the-art single-dish and interferometric instruments enable users to collect the absorption and emission line spectra for a variety of molecules in a single observational data set (Corby et al., 2015; Thiel et al., 2018; Corby et al., 2018; Thiel et al., 2019). Because many molecular lines are available simultaneously, the physical quantities typically calculated from molecular absorption lines (eg. temperatures, densities, extinctions, etc.) can be performed for each of the observed species. In practice, the population analysis of a single *tracer* molecule is used to determine a physical condition; rotation-inversion lines of ammonia (NH₃) can be used to determine kinetic temperatures (Tieftrunk et al., 1994), and the molecular hydrogen column density along the line of sight can be estimated from a single line-to-continuum ratio of an optically thin *tracer* HCO⁺ (Greaves and Nyman, 1996) or more recently *c*-C₃H₂ (Corby, J., 2016). The physical conditions of a single molecular component can be reasonably extended to other molecules with similar line shapes and kinematic profiles within the single-dish surveys because the observed region must be interpreted as an homogeneous column if column densities are determined by integrating the optical depths over the line shape. Relative molecular abundances calculated under this assumption for single dish observations, then, effectively average any phase segregation and all spatial gradients inherent to the absorbing region, while the same averaging applies for each resolution element in interferometric images of molecular absorption. Nevertheless, astrochemical kinetics models well account for the relative abundances of both simple and complex molecules in a multitude of phases within the interstellar medium (ISM): dark clouds (Herbst and Klemperer, 1973; Maffucci et al., 2018), diffuse clouds (Hersant et al., 2009), hot cores (Garrod, Wakelam, and Herbst, 2007), and active galactic nuclei (AGN) (Harada, Herbst, and Wakelam, 2010).

The line-of-sight to the star-forming region Sagittarius B2 has a very complex molecular spectrum (Herbst and van Dishoeck, 2009), and continued analysis of the Green Bank Telescope’s 1 - 50 GHz PRIMOS data (Neill et al., 2012) evidences first detections of exotic molecules within the central hot core including propenylidyne (1-C₃H) (McGuire et al., 2013), ethanimine (CH₃CHNH) (Loomis et al., 2013), and E-cyanomethanimine (HNCHCN) (Zaleski et al., 2013). Translucent clouds along this line-of-sight have also been studied using molecular tracers: kinetic temperatures have been constrained using both ammonia and water lines (Tieftrunk et al., 1994);(Cernicharo et al., 1997), molecular hydrogen columns have been estimated using the formyl ion and cyclopropenylidene (Greaves and Nyman, 1996);(Corby, J.,

2016), and visual extinctions have been determined using HI 21-cm maps (Indriolo et al., 2015) and molecular hydrogen column estimations (Corby, J., 2016). Although broadband spectra have been obtained for this line-of-sight by many telescopes including the IRAM 30-m (Belloche et al., 2013);(Belloche et al., 2014), ALMA (Belloche et al., 2016), the HIFI instrument on *Herschel* (Neill et al., 2014), the Green Bank Telescope (Neill et al. 2012), the Atacama Large Telescope Array (ATCA) (Corby et al., 2015), and the Swedish ESO Telescope (Greaves and Nyman, 1996), few large sets of molecular abundances have been calculated (Greaves and Nyman, 1996; Corby, J., 2016) for the absorbing regions. To complicate the situation, the physical conditions determined from molecular tracers span ranges characteristic of the translucent phase of the molecular ISM, but inconsistencies between the exact hydrogen columns of the absorbing regions can introduce biases in sets of abundances that contain molecules with chemical sensitivities over the representative parameter space or for abundances that do not arise from similar regions.

In this second part of our study on the chemical composition of molecular gas in the Galaxy, we model the time-dependent relative molecular abundances of a selection of species observed in the PRIMOS data set obtained using the Green Bank Telescope. The PRIMOS survey was conducted using the Robert C. Byrd Green Bank Telescope (GBT) toward the Large Molecular Heimat (LMH), a source containing hot cores in the southwest region of the north part of the Sagittarius B2 molecular cloud complex, Sgr B2(N), with coordinates $\alpha = 17^{\text{h}}47^{\text{m}}19.8^{\text{s}}$, $\delta = -28^{\circ}22'17''$ (Corby et al., 2018). Absorption lines of cyclopropenylidene $c\text{-C}_3\text{H}_2$, sulfur monoxide SO, carbon monosulfide CS, dicarbon monosulfide CCS, the thioformyl cation HCS^+ , and thioformaldehyde H_2CS have been observed in the PRIMOS survey, and relative molecular abundances have been calculated by normalizing the observed column densities by imposing a constant hydrogen column density with respect to cyclopropenylidene, $X_{c\text{-C}_3\text{H}_2} = N_{c\text{-C}_3\text{H}_2}/N_{\text{H}_2} = 2.5 \times 10^{-9}$ (Liszt et al., 2012; Corby et al., 2018). We use the grid modeling method developed in the first paper (Maffucci et al., 2018) to model the sulfur-containing species observed in the PRIMOS survey while varying free parameters in the chemical kinetic model to show how varying each parameter over ranges characteristic of translucent cloud conditions affects the time-dependent relative molecular abundances. We model the agreement by calculating the rms log differences between the sets of observed and modeled abundances (Maffucci et al., 2018) for four kinematic components $v = -23, -40, -73, \text{ and } -106$ km/s as well as the correlation coefficients (Harada et al., 2019) to quantify the absolute and relative agreement, respectively, between the observations and our models. Finally, the best models are identified by minimizing the rms log differences with respect to time for each combination of free parameters, and we discuss the effects the variation of parameters has on the abundances and the translucent cloud model fits.

3.2 CHEMICAL MODEL

Astrochemical kinetic models require knowledge of both the initial conditions and the physical histories of each astrophysical system to model accurately the chemical evolution of observed relative molecular abundances. The physical conditions determined from absorption line analysis depend on the assumptions used to model the radiative transfer and typically include a continuum source and an absorbing gas in local thermodynamic equilibrium with a particular excitation temperature describing the relative population of states. The excitation temperatures are used to constrain kinetic gas temperatures and densities, while column densities can be determined by integrating the optical depths of the absorption lines over the kinematic components that represent the absorbing columns. The ratios of column densities or integrated optical depths, then, can be used to calculate the relative abundances of a medium in LTE and chemical equilibrium.

In light of what is known, we strive to represent accurately the physical parameter space for translucent clouds within the context of what is justified from observational evidence. The values reported in Table 3.1 describe the homogeneous physical conditions we adopt for our first grid models describing possible combinations of translucent cloud conditions.

3.2.1 Gas and Dust Temperature

The $2_{12}-1_{01}$ absorption transition of *ortho*-water (*o*-H₂O) at 179.5 μ m was measured with the Long Wavelength Spectrometer (LWS) on the ISO satellite, and models of the first several transitions of *o*-H₂O and a 30 K dust continuum produced upper limits on the temperature and molecular hydrogen densities $T_k = 35$ K when $n(\text{H}_2) = 10^5 \text{ cm}^{-3}$ and $T_k = 30$ K when $n(\text{H}_2) = 10^6 \text{ cm}^{-3}$ for the star forming region with positive velocities Cernicharo et al. (1997). The observed widespread absorption over the negative velocity range associated with translucent clouds along the line of sight was included in the previous model as a shell of gas with $N(\text{H}_2) = 10^{21} \text{ cm}^{-2}$, but the statistical equilibrium calculations for this phase were not reported.

In a survey of many absorbing objects using the Effelsburg 100-m telescope, the ammonia rotation-inversion transitions NH₃(1,1) were used to determine the kinetic temperatures of each of the specific absorbing components centered at negative velocities along the line of sight (Tieftrunk et al., 1994). We record these temperatures and their uncertainties in Table 1 and use them to place limits on the temperature range of our grid models.

Models of the thermal dust continuum emission can be used to constrain the dust temperature for molecular clouds and in particular the star forming region Sgr B2(N) (Cernicharo et al., 1997; Liu and Snyder, 1999; Thiel et al., 2019). Models of the absorption lines in the translucent clouds along the line of sight to the star forming regions Sgr B2, however, use the cosmic microwave background as the continuum against which the molecular component absorb (Greaves and Nyman, 1996; Corby

et al., 2018; Thiel et al., 2019) as a result of the diffuse nature of the translucent gas, which requires a strong continuum background source for observation. A PDR model of the Horsehead Nebula using the MEUDON code (Le Petit et al., 2006) shows the grain temperatures remain around 20 K for molecular clouds with low hydrogen fractions $f_{\text{H}_2} < 1$, low densities $n < 5 \times 10^4 \text{ cm}^{-3}$, and low extinctions $A_V < 3$ (Le Gal et al., 2017), while Galactic Center clouds with densities $n \sim 10^5 \text{ cm}^{-3}$ exhibit slightly higher dust grain temperatures $T_{\text{dust}} \sim 25 \text{ K}$ (Immer et al., 2016). We set the grain temperatures in our grid model to 20 K for clouds with gas temperatures $T_{\text{gas}} \geq 20 \text{ K}$ except in the case when the kinetic temperature is 10 K, for which we use $T_{\text{gas}} = T_{\text{dust}} = 10 \text{ K}$.

3.2.2 Hydrogen Column and the Radiation Field Strength

The hydrogen column for absorbing regions is often expressed as a constant by imposing an assumed value on an observation. These assumptions are guided systematic studies of many objects known to have similar conditions, and carbon monoxide (Irvine et al., 1987), the formyl ion (Greaves and Nyman, 1996), and cyclopropenylidene (Corby, J., 2016) have all been used to estimate the molecular hydrogen column and scale the calculated abundances. For any tracer molecule tr , the relative column densities for a set of i molecules can be written

$$\frac{N(i)}{N(\text{H}_2)} = \frac{N(i)}{N(tr)} \frac{N(tr)}{N(\text{H}_2)} \quad (3.1)$$

where the first ratio of column densities on the right-hand side is determined from line analysis and the second ratio is the constant molecular hydrogen column density assumption expressed as a ratio with respect to a single molecule. In chemical equilibrium, the constant density column ratios are equivalent to the abundance ratios, and the relative abundances X can be written

$$X(i) = \frac{n(i)}{n(\text{H}_2)} = \frac{N(i)}{N(tr)} \frac{N(tr)}{N(\text{H}_2)}. \quad (3.2)$$

The visual extinction of each kinematic component is linearly related to the total nuclear hydrogen column density $A_V \propto N_{\text{H}} = N(\text{H}) + N(\text{H}_2)$, but the exact proportionality varies among studies. A sample of supernova remnants (SNRs) has been used to constrain this value by determining the hydrogen columns of the observed 0.2 - 8.0 keV spectra with intrinsic source spectra under various X-ray source models (blackbody, power-law, thermal plasma, etc.) and by using reddening measurements with nearby stars to parametrize the visual extinction A_V in terms of the atomic and molecular hydrogen columns (Güver and Özel, 2009):

$$\frac{A_V}{\text{mag}} = \frac{N(\text{H}) + 2N(\text{H}_2)}{(2.21 \pm 0.09) \times 10^{21} \text{ cm}^{-2}}. \quad (3.3)$$

The molecular hydrogen columns for the absorbing regions toward Sgr B2(N) vary by up to factors of 10 when traced by both the formyl ion (HCO^+) (Greaves and Nyman, 1996) and cyclopropenylidene ($c\text{-C}_3\text{H}_2$) (Corby, J., 2016), and the resulting extinctions ($A_V \sim 1 - 5$) subtend a range intermediate to the dark and diffuse phases of the molecular ISM (Snow and McCall, 2006). For our fiducial models, we adopt the visual extinctions that are reported with the molecular abundances; these extinctions were determined from the hydrogen column estimations using the PRIMOS data (Corby, J., 2016) and atomic HI 21-cm emission spectra (Indriolo et al., 2015).

Imposing a hydrogen column density N and a particle density n constrains a path length by $l = \frac{N}{n}$ and because the visual extinction, an integrated quantity in molecular line models and a local quantity chemical kinetic models, depends on the hydrogen column, clouds with low column densities can exhibit large densities that appear to contradict the visual extinctions for regions with small path lengths.

The relative strength of the radiation field depends on the local stellar environment and the density of the absorbing region (Harada, Thompson, and Herbst, 2013; Cleeves et al., 2016). Because images of the absorbing molecular kinematic components toward SgrB2 are relatively new and reveal heterogeneous environments (Corby et al., 2015; Thiel et al., 2018, 2019), we vary the local interstellar radiation field (ISRF) of our models using the parameter G_0 and values of 1, 10 and 100 to determine the effect of ISRF's of greater intensity on the time-dependent relative molecular abundances in translucent cloud conditions.

3.2.3 Cosmic Ray Ionization

The absorption spectra of OH^+ and $o\text{-H}_2\text{O}^+$ observed along the line of sight toward SgrB2 have been analyzed using a steady-state chemical model resulting in very low hydrogen fractions ($f_{\text{H}_2} < 0.1$) and large cosmic ray ionization rates for atomic hydrogen ($\zeta_{\text{H}} \sim 10^{-16} - 10^{-14} \text{ s}^{-1}$) for broad, negative kinematic components ($v = [-130, -60], [-60, -31], [-31, -7] \text{ km/s}$) corresponding to extended regions of molecular absorption (Indriolo et al., 2015). The hydrogen columns determined from cyclopropenylidene absorption observed in the PRIMOS survey reveal more distinct kinematic components and larger molecular hydrogen fractions when compared with the broad absorption of OH^+ and $o\text{-H}_2\text{O}^+$ seen in *Herschel* survey suggesting the translucent clouds traced by $c\text{-C}_3\text{H}_2$ exist as compact regions within an extended diffuse medium of molecular ions (Corby et al., 2015, 2018). Furthermore, chemical models of active galactic nuclei implement molecular hydrogen cosmic ray ionization rates greater than those identified for diffuse clouds by several orders of magnitude: $\zeta_{\text{H}_2} \sim 10^{-13} \text{ s}^{-1}$ at a distance of 1 pc from the galactic center and $\zeta_{\text{H}_2} \sim 10^{-15} \text{ s}^{-1}$ at a distance of 100 pc (Harada, Thompson, and Herbst, 2013). To account for the wide range of values of cosmic ray ionization rates in these previous studies, we vary the cosmic ray ionization rate of molecular hydrogen by several orders of magnitude $\log(\zeta/\text{s}^{-1}) = -17, -16, -15, -14, -13$ spanning the conditions characteristic of quiescent and Galactic center molecular gas in quiescent and to observe

the effect it has on the time-dependent relative molecular abundances of the kinetic model and the observed molecular abundance fits of sulfur species observed toward SgrB2.

3.2.4 Elemental Composition

For each absorbing kinematic component, the molecular hydrogen fraction differs depending on the environment from which the absorption arises; we implement three combinations of the fractional abundances of molecular and atomic hydrogen (see Table 3.3) corresponding to the values tabulated for each of the kinematic components observed in the PRIMOS survey (Corby et al., 2018). We vary the fractional elemental abundance of sulfur using four log-spaced points between the “low-metal” value $f_S = 8.0 \times 10^{-8}$ (Graedel, Langer, and Frerking, 1982) and the enhanced value $f_S = 1.5 \times 10^{-5}$ (Vidal et al., 2017) recommended with our chemical network to show how each of the abundances of the sulfur species in translucent cloud conditions responds to the elemental abundance of sulfur and to show how well each of the models of the group of abundances are fit by each value. Similar to the previous chapter, we implement two values of the fractional elemental abundance of oxygen corresponding to an intermediate and high depletion cases, $f_O = 2.4 \times 10^{-4}$ and 1.4×10^{-4} (Hincelin et al., 2011; Maffucci et al., 2018). The fractional elemental abundances for helium (Wakelam and Herbst, 2008), carbon and nitrogen (Jenkins, 2009), fluorine (Neufeld, Wolfire, and Shilke, 2005), and other metals follow from the first part of our study (Maffucci et al., 2018).

3.2.5 Reaction Network, Rate Solver, and Grid Models

The chemical network and numerical integration package we use to solve the system of differential rate law equations and compute the time-dependent relative molecular abundances follows from the first part of the study (Maffucci et al., 2018). We implement a composite reaction network based off of the KInetic Database for Astrochemistry (KIDA) (Harada, Herbst, and Wakelam, 2010; Wakelam et al., 2012, 2015; Ruaud et al., 2015; Ruaud, Wakelam, and Hersant, 2016; Le Gal et al., 2017; Vidal et al., 2017) and contains ice-mantle and ice-surface species (Hasegawa, Herbst, and Leung, 1992; Hasegawa and Herbst, 1993a,b; Garrod, Wakelam, and Herbst, 2007; Ruaud et al., 2015; Ruaud, Wakelam, and Hersant, 2016) for a three-phase chemical network. To solve the system of differential rate law equations, we use the latest version of the NAUTILUS code which has been updated to include Eley Rideal and van der Waal’s complex reaction mechanisms and three-phase capabilities (Ruaud et al., 2015; Ruaud, Wakelam, and Hersant, 2016).

Because many of the physical conditions are not well-constrained for the multiple molecular components seen in several absorbing kinematic components toward SgrB2, we implement the grid modeling technique described in the first part of the study (Maffucci et al., 2018) to separate explicitly the effect varying each free parameter in the chemical model has on the time-dependent relative molecular abun-

dances and the agreement between our model abundances and the abundances observed in several translucent clouds toward SgrB2. We construct 12D structures $\{X_i, t, T_{\text{gas}}, n, A_V, \zeta, T_{\text{dust}}, G_0, f_{\text{H}_2}, f_{\text{H}}, f_{\text{O}}, f_{\text{S}}\}$ for each molecular abundance X_i at each time t and combination p of free parameters $\{T_{\text{gas}}, n, A_V, \zeta, T_{\text{dust}}, G_0, f_{\text{H}_2}, f_{\text{H}}, f_{\text{O}}, f_{\text{S}}\}$ for a composite grid model with 36,000 combinations of free parameters.

3.2.6 Modeling Methods

To quantify the agreement between our models and the observed abundances of each of the translucent clouds, we calculate the root-mean-square (rms) log difference

$$\mathcal{A}(p, t) = \left[\frac{1}{n} \sum_i^n [\log(X_m(p, t)/X_o)]_i^2 \right]^{1/2} \quad (3.4)$$

between the modeled abundances X_m and the observed abundances X_o for each kinematic component. The rms log difference $\mathcal{A}(p, t)$ provides a measure of the absolute agreement between the two sets of abundance values as a function of time and physical conditions and quantifies the average factor of agreement between a given modeled and observed abundance within each kinematic component group using equal weights among molecular constituents (Maffucci et al., 2018).

Additionally, we calculate the correlation coefficients

$$r(p, t) = \frac{\sum_i \log\left(\frac{X_{i,m}(p,t)}{X_m(p,t)}\right) \cdot \log\left(\frac{X_{i,o}}{X_o}\right)}{\sqrt{\sum_i \log\left(\frac{X_{i,m}(p,t)}{X_m(p,t)}\right)^2 \cdot \sum_i \log\left(\frac{X_{i,o}}{X_o}\right)^2}} \quad (3.5)$$

to measure the linearity of the relation between the sets of observed and modeled abundances for each kinematic component (Harada et al., 2019). Calculating the correlation coefficient $r(p, t)$ is a simple way to determine systematic errors in both the chemical model free parameters and in the hydrogen column or other normalization factor that relates observed molecular line intensities and the associated column densities to a set of relative molecular abundances. A scatterplot of the modeled abundances versus the observed abundances can reveal the deviation from linearity reflected in the correlation coefficient, any constant error emerging among all abundances as an identical shift, and clear abundance outliers in each model.

The rms log difference \mathcal{A} and the correlation coefficient r express different types of agreement between the modeled and observed abundances, and we impose two criteria, one for each quantity, to express the degree of fit. For the rms log differences \mathcal{A} , models where $\mathcal{A}(p, t) < 1$ are considered solutions where the average factor of agreement between a given modeled and observed abundance in the group is no greater than ten, or one order of magnitude (Maffucci et al., 2018). When the correlation coefficient has been used to determine the degree of agreement between modeled modeled and emission line intensities observed toward the molecular cloud W51, regions

of high correlation ($r \gtrsim 0.7$) are identified to determine models with good agreement, but not all values of the correlation coefficient in those solution regions follow that criterion strictly; implementing this method in the same study to determine good models for the M51 molecular cloud complex, correlation coefficients subtend a range with values as low as $r = 0.43$ (Harada et al., 2019). Because of the large number of models in our grid simulations, we strictly impose the criterion $r(p, t) > 0.66$ to determine which models are well correlated with the observed abundances in each of the absorbing kinematic components toward SgrB2.

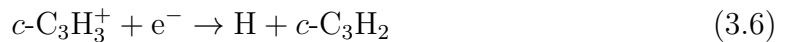
3.3 RESULTS AND DISCUSSION

3.3.1 Abundance Profiles

Table 3.4 shows the observed abundances (Corby et al., 2018) for each species in each kinematic component as well as the associated abundance character \mathcal{C} , which follows from the first part of the study (Maffucci et al., 2018) where (1) represents inertness, (2) characterizes a maximum or minimum, (3) corresponds to a monotonic increase or decrease, and (4) indicates oscillatory behavior. The character can be used to guide fitting analytical expressions to the time-dependent relative molecular abundances, but we leave that analysis for a future study. In the following sections, we discuss the reactions that dominate the production and destruction of each species in the fiducial model of the kinematic component $v = -23$ km/s (see Table 3.5, top block) because it has physical conditions that characterize the transition between dark and translucent molecular gas and to show the effect deviation from this model into diffuse cloud conditions affects the chemistry of each species as relevant free parameters are varied. Figure 3.1 shows the modeled time-dependent abundances $X(t)$ where each row corresponds to a unique species and each column shows the fiducial models for each of the four kinematic components. In each panel, the fractional elemental abundance of sulfur f_{S} is varied to show the effect on the abundances of each species for each fiducial model.

Cyclopropenylidene

In the fiducial model, cyclopropenylidene is mainly produced by the dissociative recombination reaction



of protonated cyclopropenylidene and by the neutral-neutral, cyclization reaction



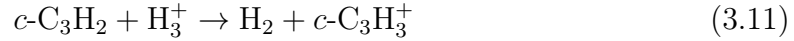
of the linear isomer propadienylidene with atomic hydrogen. At early times $t \sim 10^5$ years, the destruction of cyclopropenylidene occurs mainly via the neutral-neutral mechanisms



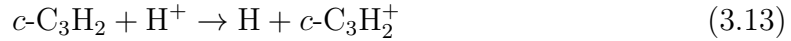
and by the ion-molecule reaction



While reaction 3.6 dominates the production at early times, both it and 3.7 come to contribute equally at times $t > 10^6$ years, and these later times also effect a shift in the dominant destruction mechanisms to ion-molecule reactions



with protonated molecular hydrogen to produce protonated isomers of cyclopropenyli-dene. In low density models, the production remains similar to the mechanisms for the fiducial model, and destruction at early times is dominated by ion-reactions



with ionic hydrogen while later times give rise to the efficiency of the neutral-neutral reaction



which contributes equally to the destruction with reactions 3.11 and 3.13, in addition to the destruction reaction



as well as the reactions



with ionic carbon. The change in chemistry is observed in the models as the minimum character of the cyclopropenyli-dene abundances transforms into a very broad minimum feature several orders of magnitude below the fiducial model values (see

Figure 3.2). An increased cosmic ray ionization rate produces a chemistry similar to the fiducial model at early and late times, but a change in character is observed as the minimum feature observed in the fiducial model transforms into a monotonic increase with inflection around $t \sim 10^6$ years. While decreasing the visual extinction has little impact on the production fractions of reactions that create cyclopropenylidene, photodissociation reactions



each contribute significantly ($\sim 15\%$ at early times and $\sim 25\%$ at later times) to the destruction fraction. The minimum character also disappears at lower values of the visual extinction, where a very slight monotonic increase emerges for all fractional elemental abundances of sulfur $f_{\text{S}} < 1.5 \times 10^5$.

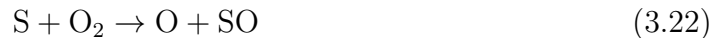
The constant abundance $X_{c\text{-C}_3\text{H}_2} = 2.5 \times 10^{-9}$ of cyclopropenylidene used to trace the molecular abundances in the absorbing components along the line of sight is relatively consistent with the abundance determined from the molecular line survey toward the peak in cyanopolyne emission of the Taurus Molecular Cloud TMC-1 CP using the Nobeyama 45m dish (Kaifu et al., 2004; Gratier et al., 2016), $\frac{X_{c\text{-C}_3\text{H}_2}^{\text{trans}}}{X_{c\text{-C}_3\text{H}_2}^{\text{dark}}} = 1.3$, supporting the claim that the cyclopropenylidene abundances are insensitive to the environment when observed in molecular line surveys (Liszt et al., 2012; Corby et al., 2018). Because the modeled abundances change in time, cyclopropenylidene can be an unbiased tracer of the relative molecular abundances for species observed along the same line of sight with similar kinematic profiles by placing constraints on the age of the absorption features.

Sulfur monoxide

Sulfur monoxide is produced by neutral-neutral reactions



and



where reaction 3.22 almost reaches the production fraction of 3.21 between $\sim 10^5$ and 10^6 years as the abundance of molecular oxygen surpasses that of the hydroxyl radical during that period. Destruction occurs as a result of reactions between sulfur monoxide and abundant ions



where the dominant channel depends on the dominant gas-phase ion. In low density conditions ($n = 10^3 \text{ cm}^{-3} \text{ s}^{-1}$), molecular oxygen falls short of the fiducial model abundance by about an order of magnitude, and the reaction



dominates production along with reaction 3.21, while reaction 3.23 dominates the destruction of sulfur monoxide in low density models. In the case of a higher cosmic ray ionization rate ($\zeta = 10^{-15} \text{ s}^{-1}$), the hydroxyl radical exists in greater abundance than molecular oxygen shifting the dominance shared between reactions 3.21 and 3.22 to the reaction with the hydroxyl radical at times $t > 10^5$ years, while reaction 3.24 overtakes destruction of sulfur monoxide by reaction 3.23 after $\sim t = 10^5$ years. When extinctions reach the low value $A_V = 2$, photodissociation of sulfur monoxide becomes so efficient that abundances barely breach the 10^{-11} threshold, and an increase in the fractional elemental abundance of sulfur to $f_S = 1.0 \times 10^{-5}$, where the abundance exhibits little change with increasing sulfur abundances, is necessary to mitigate the photodissociation efficiency (see Figure 3.3).

The neutral-neutral reactions 3.21 and 3.21 responsible for the production of sulfur monoxide in our models are consistent with the dominant mechanisms in gas-phase models of dense molecular cloud conditions (Prasad and Huntress, 1982; Millar and Herbst, 1990), while destruction through abundant ions is also similar among the models. The translucent cloud abundances of sulfur monoxide are slightly lower than the dark cloud values toward TMC-1 CP (Gratier et al., 2016), but $0.21 < \frac{X_{\text{SO}}^{\text{trans}}}{X_{\text{SO}}^{\text{dark}}} < 0.54$ suggesting only slight deviations from the dark-abundances for the translucent-cloud abundances.

Carbon monosulfide

The primary production reactions for carbon monosulfide are the dissociative recombination reaction

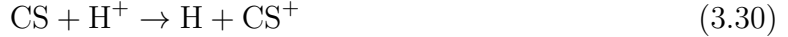


of the thioformyl cation and the neutral-neutral reactions

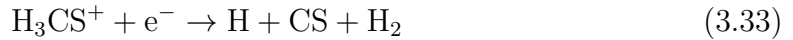




between the thioformyl radical and atomic hydrogen and between atomic sulfur and diatomic carbon, Carbon monosulfide undergoes destruction in a similar manner to sulfur monoxide via the ion-neutral reactions



with abundant ions in the gas. In low density conditions, carbon monosulfide production continues to be dominated by reactions 3.27 and 3.28, but the dissociative recombination reactions



contribute almost equally to the production around $t = 10^5$ years. Destruction, in this case, results almost exclusively from reaction 3.30 until $t = 2 \times 10^6$ years, when reaction 3.31 comes to full dominance ($\sim 80\%$) of the destruction fraction. Low density conditions result in low carbon monosulfide abundances (see Figure 3.4), and the highest fractional elemental abundance of sulfur, $f_S = 1.5 \times 10^5$, still slightly underproduces CS in the gas. Increased cosmic ray ionization rates shift the dominant production mechanism of carbon monosulfide to the neutral-neutral reaction 3.29 between atomic sulfur and diatomic carbon, though only by a small margin as the electron density significantly diminishes around $t \sim 10^5$ years, later than when an analogous electron density decrease occurs in the fiducial model, resulting in a lower production fraction of the dissociative recombination reaction 3.27 at later times, while reaction 3.31 dominates the destruction. In this model, a very sharp inflection can be seen around $t = 10^5$ years where the models that best fit the observed CS abundances shift from those with high $f_S = 1.5 \times 10^5$ to the low-metal value $f_S = 8.0 \times 10^8$. Similar to sulfur monoxide, the photodissociation of carbon monosulfide dominates its destruction in models with low visual extinctions. The large abundances of CS, however, compensate for the increased efficiency of photodissociation, and the abundances exhibit only small changes such as slight decreases at times $t < 10^5$ years and slight increases at times $t > 10^5$ years.

The translucent-cloud abundances of carbon monosulfide are substantially larger than the dark-cloud values, $2.5 < \frac{X_{\text{CS}}^{\text{trans}}}{X_{\text{CS}}^{\text{dark}}} < 8.7$, but the formation and destruction mechanisms are similar to previously run dark-cloud models (Prasad and Huntress,

1982; Millar and Herbst, 1990) reflecting a lower degree of sulfur depletion in translucent-cloud conditions compared with dark-cloud conditions (Ruffle et al., 1999; Gratier et al., 2016; Corby et al., 2018).

Dicarbon monosulfide

The chemical reactions that chiefly contribute to the production of dicarbon monosulfide are the dissociative recombination reaction



and the neutral-neutral reaction



both of which resemble analogs to the reactions producing carbon monosulfide. Destruction of CCS occurs via the neutral-neutral reaction



at early times ($t \sim 10^5$ years) and via the ion-molecule reactions



in the gas. Decreasing the density from the fiducial model value results in production of CCS by reaction 3.35 with near absolute dominance until $t \sim 10^6$ years, when the production fraction falls below 90%. Destruction in the low density model is also almost completely dominated by reaction 3.38 until $t \sim 10^6$ years, when reaction 3.39, the neutral-neutral reaction



and the ion molecule reaction



contribute near equally. In contrast to carbon monosulfide, the abundance of dicarbon monosulfide is not sufficiently mitigated by the increased fractional elemental abundances of sulfur in this study to model effectively the observed abundances of CCS at low densities (see Figure 3.5). For the model with increased cosmic ray ionization rate, the chemistry of CCS is very similar to that of the low density case, and an inflection similar to the one observed for carbon monosulfide appears around $t = 10^5$ years. Decreasing the extinction from the fiducial value appears to have less

of an impact on the abundances of CCS when compared to the effect this change has on the abundances of CS. The abundances of CCS appear to have greater monotonic character generally, so the emergence of this character is less pronounced when compared to the clear change observed in CS. The dominant production mechanism in the low extinction model for CCS shifts from reaction 3.35 to reaction 3.36 around $t = 10^6$ years, while notably the neutral-neutral reaction 3.41 dominates destruction for early and late times with smaller contributions from ion-molecular reactions in the gas.

Dicarbon monosulfide exhibits the largest difference between the abundances observed in dark and translucent-cloud conditions $0.01 < \frac{X_{\text{CCS}}^{\text{trans}}}{X_{\text{CCS}}^{\text{dark}}} < 0.03$ (Gratier et al., 2016; Corby et al., 2018) suggesting either that the radicals, which were previously thought not to be very reactive in dark-cloud conditions (Millar and Herbst, 1990) undergo less production or more destruction to the extent of depleting dicarbon monosulfide by up to two orders of magnitude in translucent clouds (Corby et al., 2018). Increasing the fractional elemental abundance of sulfur beyond the low-metal value could mitigate this discrepancy, but the differences indicate that CCS and longer sulfur-containing carbon-chain molecules could be used to distinguish between dark and translucent cloud conditions in observations.

Thioformyl cation

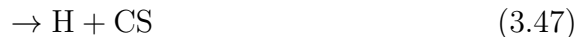
The thioformyl cation is produced primarily through ion-molecule reactions



between carbon monosulfide and abundant ions in the gas and by



while destruction occurs via dissociative recombination reactions



where the destruction fractions of reactions 3.46 and 3.47 is 4:1. In the low density model, the destruction fractionation remains the same as in the fiducial model, but the production fraction is dominated by reaction 3.44 until $t \sim 10^6$ years, when reaction 3.45 achieves the greatest production fraction, $\sim 60\%$. High cosmic ray ionization rate conditions yield a similar chemistry as the low density conditions with a slightly larger production fraction of reaction 3.45 ($\sim 80\%$) at later times. In contrast to the

low density HCS^+ abundances, which achieve observed values for increased f_S , the high cosmic ray ionization abundances emerge as sigmoidal features with inflection around $t = 10^6$ years and fit the observed values better with high f_S at early times $t < 10^6$ years and low f_S at later times $t > 10^6$ years (see Figure 3.6). Lower values of the visual extinction effect a similar chemistry as the low density and high cosmic ray ionization models, but the overall effect, despite similar fractionations, is apparent in the variation in abundance character among the three models, where low visual extinctions decrease the early time abundances of HCS^+ without exhibiting as significant of a change from the fiducial model abundances as in the other two models.

The thioformyl cation exhibits similar abundances in translucent and dark cloud observations $0.22 < \frac{X_{\text{HCS}^+}^{\text{trans}}}{X_{\text{HCS}^+}^{\text{dark}}} < 0.49$ (Gratier et al., 2016; Corby et al., 2018), though the translucent cloud abundances are slightly smaller than the dark cloud values and are often within the uncertainty of the dark-cloud value. This result is anomalous since molecular ions typically trace extended regions of absorption and emission (Cernicharo et al., 1997; Indriolo and McCall, 2012; Indriolo et al., 2015; Soma et al., 2015; Corby et al., 2018), though this ratio could arise as a result of differences in models of radiative transfer used to model the molecular lines as well as from differences in the normalization of the column densities determined from observations, specifically using molecular hydrogen versus cyclopropenylidene.

Thioformaldehyde

At very early times $t < 10^5$ years, the production of thioformaldehyde is dominated by the dissociative recombination reaction



until $t = 10^5$ years when the neutral-neutral reaction



usurps control of the production with 80% of the production fraction. Around $t = 3 \times 10^5$ years, both reactions maintain about 50% of the production fraction for about ten thousand years, though shortly after ($t = 4 \times 10^5$ years), the production fraction ratio of 4:1 for reactions 3.48 and 3.49, respectively, is restored. The destruction of thioformaldehyde is shared equally among ion-molecule reactions



and to a slightly lesser extent by the photodissociation reaction



and the neutral-neutral reaction



At later times $t > 10^6$ years, reaction 3.51 dominates the destruction fraction contributing 60%, and the production mechanisms remain relatively unchanged. In low density conditions, a similar chemistry as in the fiducial model accounts for the production of thioformaldehyde, but the timescale of dominance inversion shifts to $t \sim 2 \times 10^6$ years, while ion-molecule reactions with ionic hydrogen dominate the destruction at early times before destruction of thioformaldehyde is comprised of the aforementioned reactions at later times. Increased cosmic ray ionization rates have little effect on the particular mechanisms and production fractions resulting in the production and destruction of thioformaldehyde, but the inflection observed in the same model for the other abundances also emerges here (see Figure 3.7). Decreased extinctions induce an increase in the efficiency of photodissociation of thioformaldehyde resulting in its emergence as the dominant destruction mechanism, and moderate values of f_S mitigate the overall decrease in the thioformaldehyde abundances in these models.

The ratios of the translucent-cloud abundances to the dark-cloud values for thioformaldehyde $0.03 < \frac{X_{\text{HCS}^+}^{\text{trans}}}{X_{\text{HCS}^+}^{\text{dark}}} < 0.13$ (Gratier et al., 2016; Corby et al., 2018) are significantly small indicating that thioformaldehyde could, like dicarbon monosulfide, could serve as a tracer that distinguishes between dark and translucent-cloud conditions. In contrast to the typical dissociative recombination reactions leading to the production of thioformaldehyde in the gas-phase (Prasad and Huntress, 1982), our models have significant production via the neutral-neutral mechanism of reaction 3.49 indicating the impact of the addition into chemical networks of gas-phase neutral-neutral reactions, which can sufficiently reproduce the abundances of larger molecules like acetaldehyde CH_3CHO and formamide NH_2CHO in the gas phase (Barone et al., 2015).

3.3.2 Model Agreement and Solution Spaces

In Table 3.5, we present the minimum rms log differences \mathcal{A}_{\min} , the best fit times $\mathcal{T}_{\mathcal{A}}$, the correlation coefficient at these times $r(\mathcal{T}_{\mathcal{A}})$, the maximum correlation coefficients r_{\max} , the time corresponding to the maximum correlation coefficients \mathcal{T}_r , and the rms log differences at these times $\mathcal{A}(\mathcal{T}_r)$. The time of maximum correlation appears earlier than the best fit time for each of the fiducial models, but in the case of the $v = -73$ km/s component where $\log(\mathcal{T}_r) = 2.101$, the method of determining the chemical timescale by maximizing the correlation coefficient yields an unfeasible result that is further evidenced by the large rms log different $\mathcal{A}(\mathcal{T}_r) = 3.813$. This

result suggests a reasonable correlation coefficient alone is not a sufficient criterion for determining the agreement between modeled and observed abundances, though if the time were reasonable, it would suggest a systematic error such as an inaccurate estimation of the hydrogen column used to normalize the observed abundances. The abundances of each of the fiducial models exhibit good agreement with the observed abundances in each of the kinematic components except when $v = -40$ km/s, where $\mathcal{A}_{\min} = 1.024$ and temperatures $T_{\text{gas}} = T_{\text{dust}} = 10$ K are colder compared to the others.

Global solutions are also recorded in Table 3.5 where the rms log differences \mathcal{A}_{\min} and correlation coefficients r_{\max} are independently minimized and maximized, respectively, over the entire parameter spaces of each kinematic component for each set of observed abundances, and the corresponding values of the free parameters are also presented in Table 3.5 as the optimized model parameters within the uncertainties of the observed conditions.

3.3.3 Minimum Solution Spaces

The minimum solution spaces, the set of combinations of free parameters that yield a single, reasonable time t when $\mathcal{A} < 1$ (Maffucci et al., 2018), for each kinematic component are explored in the vicinity of the fiducial model parameters in Figures 3.12, 3.13, 3.14, 3.15, which show heat maps of the minimum rms log differences \mathcal{A}_{\min} (left column) and the best fit times $\mathcal{T}_{\mathcal{A}}$ (right column) for each combination of free parameters in the chemical model.

These heat maps are analogous to the symbolic Tables 6-13 in the first part of the study (Maffucci et al., 2018) but show the exact values of \mathcal{A}_{\min} and $\mathcal{T}_{\mathcal{A}}$ for each free parameter combination. This method shows the extent to which varying multiple free parameters simultaneously affects the model fits (Harada et al., 2019). Using this method, the boundaries in the parameters space that result in possible solutions to the model abundances as well as the minimum solution space become readily apparent.

Similarly, Figures 3.16, 3.17, 3.18, and 3.19 use the same method for the correlation coefficients, but we abstain from using the correlation coefficient criterion $r > 0.66$ as a sole measure of a reasonable solution since in the fiducial models strong correlation between observed and modeled abundances did not always result in good absolute agreement between the two abundance sets and because without a reasonable degree of absolute agreement between the observed and modeled abundances, the chemical kinetic model is meaningless. Furthermore, maximum correlation often emerges at very early times also suggesting the necessity of an additional method in determining good models for each set of observed abundances.

Combining the Methods of Fit

While the rms log difference has been the paradigm for determining the agreement between modeled and observed abundances in many chemical kinetic studies (Hincelin et al., 2011; Ruaud et al., 2015; Vidal et al., 2017; Maffucci et al., 2018), stronger

constraints can be placed on the large solution spaces produced by this method by also imposing a criterion of fit on the correlation coefficient. To explore this method, we present in Figures 3.20, 3.21, 3.22, and 3.23 heat maps that show the rms log differences \mathcal{A}_{\min} (left column) for models with free parameters in the vicinity of the fiducial model parameters at the best fit times of the fiducial model $\mathcal{T}_{\mathcal{A}}$, the correlation coefficients at these times $r(\mathcal{T}_{\mathcal{A}})$ (middle columns), and the overlap of the criteria of fit for the two methods \mathcal{U} (right columns) where $\mathcal{U} = 1$ when $\mathcal{A} < 1$, $\mathcal{U} = 2$ when $r > 0.66$, and $\mathcal{U} = 3$ when $r > 0.66$ and $\mathcal{A} < 1$. The value of \mathcal{U} is somewhat arbitrary to the extent that we use the values only to map colors to the heat map images. The fiducial models of the $v = -23$ km/s and $v = -106$ km/s kinematic components show $\mathcal{U} = 3$ for the fiducial models at the best fit times, but the fiducial model for $v = -40$ km/s shows only good correlation in the fiducial model at the best fit time, while the $v = -73$ km/s component only shows good absolute agreement with correlation slightly below the critical value. Although both criteria are not simultaneously satisfied by the fiducial models at the best fit times, the stronger constraints placed on the chemical models by the two fit criteria further restrict the large solution spaces and facilitate the identification of the best models within the uncertainties of the observed quantities used as physical and chemical free parameters in the chemical kinetic model.

3.3.4 Variation of Parameters

While each panel in Figure 3.1 shows variation among the fiducial model abundances, the abundances of the $v = -23$ km/s component with a modeled visual extinction $A_V = 4$ exhibit distinctly different characters from the other three. To explore the effect varying each free parameter has on the time-dependent abundances, we construct Figures 3.2, 3.3, 3.4, 3.5, 3.6, and 3.7 that show for each species the variation of one free parameter in the chemical model across each row. The second column contains identical panels to show how the fiducial models are the intersection around which each row expands for one free parameter. These figures reveal explicitly the effect each free parameter value has on the modeled abundances. Figures 3.8, 3.9, 3.10, and 3.11 are set up in the same manner but show the time-dependent rms log differences and correlation coefficients for each kinematic component.

The Effect of Density

The rates of bimolecular reactions depend on the product of the densities of the two reactant species, and density emerges as one parameter that has a significant impact on the time-dependent relative molecular abundances for all species in this study. Each molecular species is severely underproduced for densities $n \leq 10^4$ cm⁻³ s⁻¹ at times $t \lesssim 10^6$ years suggesting that tenuous translucent and diffuse cloud conditions require longer times to reproduce the observed abundances in chemical kinetic models evolving from an initial gas composed of atomic and ionic species and molecular hydrogen. This shift of the chemical timescale to later times for decreasing densities

is consistent with models of decreasing densities of dark cloud conditions and the relative molecular abundances of the cyanopolyynes and methanol and acetaldehyde toward TMC-1 (Maffucci et al., 2018), though in some cases models with densities $n = 10^3 \text{ cm}^{-3} \text{ s}^{-1}$ and below fail to reproduce the observed abundances toward SgrB2 (see Figures 3.12, 3.13, 3.14, and 3.15).

The Effect of Visual Extinction and Radiation Field Strength

Photodissociation reactions become more efficient with lower visual extinctions A_V and increased radiation field strengths G_0 , and the minimum solution space contains fewer models as parameters tend toward these conditions. The impact is most notable in the heat maps of \mathcal{A}_{\min} and \mathcal{T}_A of the $v = -40$ and -73 km/s components (see Figures 3.13 and 3.14) where large values of the interstellar radiation field strength $G_0 \geq 100$ and low extinctions $A_V = 1$ show no solutions $\mathcal{A}_{\min} < 1$, though increasing the fractional elemental abundance of sulfur above the low-metal value has a mitigating effect over other regions of the parameter space for all kinematic components. If observational constraints on the hydrogen column become stronger in future studies of the absorbing columns of the species considered in this study, accurate local visual extinctions and interstellar radiation fields can place stronger constraints on the fractional elemental abundance of sulfur. Furthermore, additional modeling efforts such as dynamics models or models starting with a larger molecular constituency could provide possible solutions to the low abundances we observe in our grid models for low extinctions.

The Effect of Cosmic Ray Ionization

Because the cosmic ray ionization of molecular hydrogen fuels the chemical evolution of molecular gas, decreasing its value in our grid model spaces generally results in earlier chemical timescales as seen in Figures 3.12, 3.13, 3.14, and 3.15 of each kinematic component, and this trend is consistent with the same impact lower values of ζ had for models of dark cloud conditions and the abundances in TMC-1 (Maffucci et al., 2018). Low cosmic ray ionization rates in the models of translucent clouds appear to alter the character of the time-dependent relative molecular abundances of all species in this study when $\zeta < 10^{-16} \text{ s}^{-1}$, and although this effect is mitigated by increasing f_S , models with these low ionization rates generally have no solution $\mathcal{A}_{\min} < 1$.

The Effect of Elemental Composition

Varying the fractional elemental abundance of oxygen from the intermediate depletion value $f_O = 2.4 \times 10^4$ which we use in the fiducial models to a high depletion value $f_O = 1.4 \times 10^4$ generally results in slightly larger abundances when compared to the fiducial models of the $v = -23$ km/s component, but sulfur monoxide is unique in that it exhibits slightly lower abundances in oxygen poor conditions as it contains oxygen in its composition. The high depletion case also effects less pronounced character features for all compounds in this study, though cyclopropenylidene shows the

greatest change going from a clear minimum to an inert character seen in Figure 3.2.

Increasing the fractional elemental abundance of sulfur beyond the low-metal value $f_S = 8.0 \times 10^{-8}$ mitigates the relative underproduction of sulfur species that arises as a result of low densities, low extinctions, high ionization rates, and strong radiation fields, but it also has the potential to overproduce sulfur-containing species. The abundances of the tracer molecule cyclopropenylidene appear inversely related to the fractional elemental abundance of sulfur, so although its abundance has been measured to be relatively constant for many translucent and diffuse molecular clouds, further studies are required to show whether or not it effectively traces all species without bias.

3.3.5 Outlier Detection

Each molecular species exhibits a unique abundance profile as a result of the competing effects of chemical reactions of various types that dominate the production and destruction at different times in each model. Imposing a single set of time-independent physical conditions on all species undermines the physical and chemical history of the objects in question, though this approach is often necessary to model the time-dependent chemistry of multiple molecular components along a single line of sight when models of the absorption lines of each individual species do not account for the unique physical conditions traced by each absorbing species. Because of this inaccuracy, it is necessary to have a method to detect outliers in the chemical model to guide future observations and kinetic simulations.

Scatter plots that show the modeled abundances X_{mod} versus the observed abundances X_{obs} at the best fit times \mathcal{T}_A of the fiducial models are presented in Figures 3.24, 3.25, 3.26, and 3.27 with rows that each vary one free parameter. Each panel contains the rms log differences \mathcal{A} and correlation coefficients r to show how the two measures of agreement are not necessarily related. Dashed black diagonals represent perfect correlation, while dotted black diagonals show the extent of the region where the fit criterion $\mathcal{A} < 1$ is satisfied. Outliers in the set of modeled abundances, then, appear as points outside of the region constrained by the dotted black lines. While this method of determining outliers is not statistically rigorous, it can be used to guide chemical models that attempt to fit multiple molecular abundances with a single set of free parameters at a single time. At the best fit times in the fiducial models for $v = -23, -40,$ and -106 km/s, HCS^+ appears as an outlier, though for the $v = -73$ km/s component, HCS^+ is within the fit criterion at \mathcal{T}_A , though SO is underproduced to the extent of existing as an outlier at the best fit time.

3.4 CONCLUSION

The rich absorption spectra of broadband single-dish and interferometric instruments enables a consistent treatment of many molecular columns. The column densities obtained from single-dish measurements, however, demand a homogeneous interpretation where gradients have been averaged over the beam; interferometric maps

mitigate this limitation to the extent of the spatial resolution and sensitivity each instrument allows. In anticipation of an evolving image of the molecular ISM, we have established a chemical model that subtends multiple combinations of translucent cloud conditions to examine how the relative molecular abundances of sulfur-containing species as well as the fits to sets of observed abundances toward Sgr B2(N) change with the variation of the free parameters. Additionally, we have identified shifts in the dominant chemical pathways as a function of multiple free parameters in the chemical kinetic model and time to show explicitly when and the extent to which specific reactions influence the evolving chemistry in molecular cloud conditions.

Some prominent aspects of our calculations are listed below:

1. The effect of varying density n and cosmic-ray ionization rate ζ on the agreement between the modeled and observed abundances is consistent with the results found in the first part of this study (Maffucci et al., 2018). Lower densities and lower ionization rates generally results in later timescales while larger densities and higher ionization rates generally results in earlier best fit times. Both n and ζ effect transformations in the character of the time-dependent abundances of all species in this study.

2. Gas temperature T_{gas} has little impact on the magnitude and character of the modeled abundances X_{mod} , the time-dependent rms log differences $\mathcal{A}(t)$, the best fit times \mathcal{T} , and the time-dependent correlation coefficients $r(t)$.

3. Increasing the fraction elemental abundance of sulfur above the low-metal value $f_{\text{S}} > 8 \times 10^{-8}$ generally mitigates the increased efficiency of photodissociation reactions for all sulfur-containing species, but the abundance of the tracer molecule cyclopropenylidene exhibits the opposite effect where its abundance is inversely related to f_{S} . The abundances of SO, CCS, HCS⁺, and H₂CS exhibit diminishing enhancements as the fractional elemental abundance increases beyond $f_{\text{S}} = 2.6 \times 10^{-6}$.

4. The method of maximizing the correlation coefficient $r(t)$ as a function of time is not a strong measure of agreement between the modeled and observed abundances as it often optimizes to very early times, though it provides an additional constraint on meaningful solutions when combined with the method of calculating the rms log difference $\mathcal{A}(t)$, which remains a good measure of absolute agreement.

5. The time-dependent abundance of the tracer molecule cyclopropenylidene, $X_{\text{c-C}_3\text{H}_2}(t)$ shows inert character for low extinction values $A_{\text{V}} < 2$, in which case it can well serve as a normalization constant converting observed column densities to abundances without placing strong constraints on the age of the abundance features.

6. The kinematic component $v = -40$ km/s has a small solution space with longer timescales characteristic of dark clouds suggesting the increased dust temperature $T_{\text{dust}} > 10$ used for the other kinematic components characterizes the translucent cloud abundances, which are similar among the four clouds.

7. Heat maps of the grid models show how the simultaneous variation of multiple free parameters in the chemical model affect the model solutions to the observed abundances while drawing boundaries in the parameter space to determine thresholds

of reasonable fits in the solution space.

8. Scatterplots of the modeled versus observed abundances provide a simple method to determine outliers in each set of modeled abundances for a given combination of free parameters in the chemical model.

Interferometric images will provide spatially-resolved images of molecular absorption toward Sgr B2(N) enabling the calculation of accurate gradients in the observed relative molecular abundances of absorbing species, and the grid models constructed in this study can be used to map time-dependent abundances to spatially-resolved absorption profile images or to guide future studies of abundance gradients observed in various phases of the molecular interstellar medium.

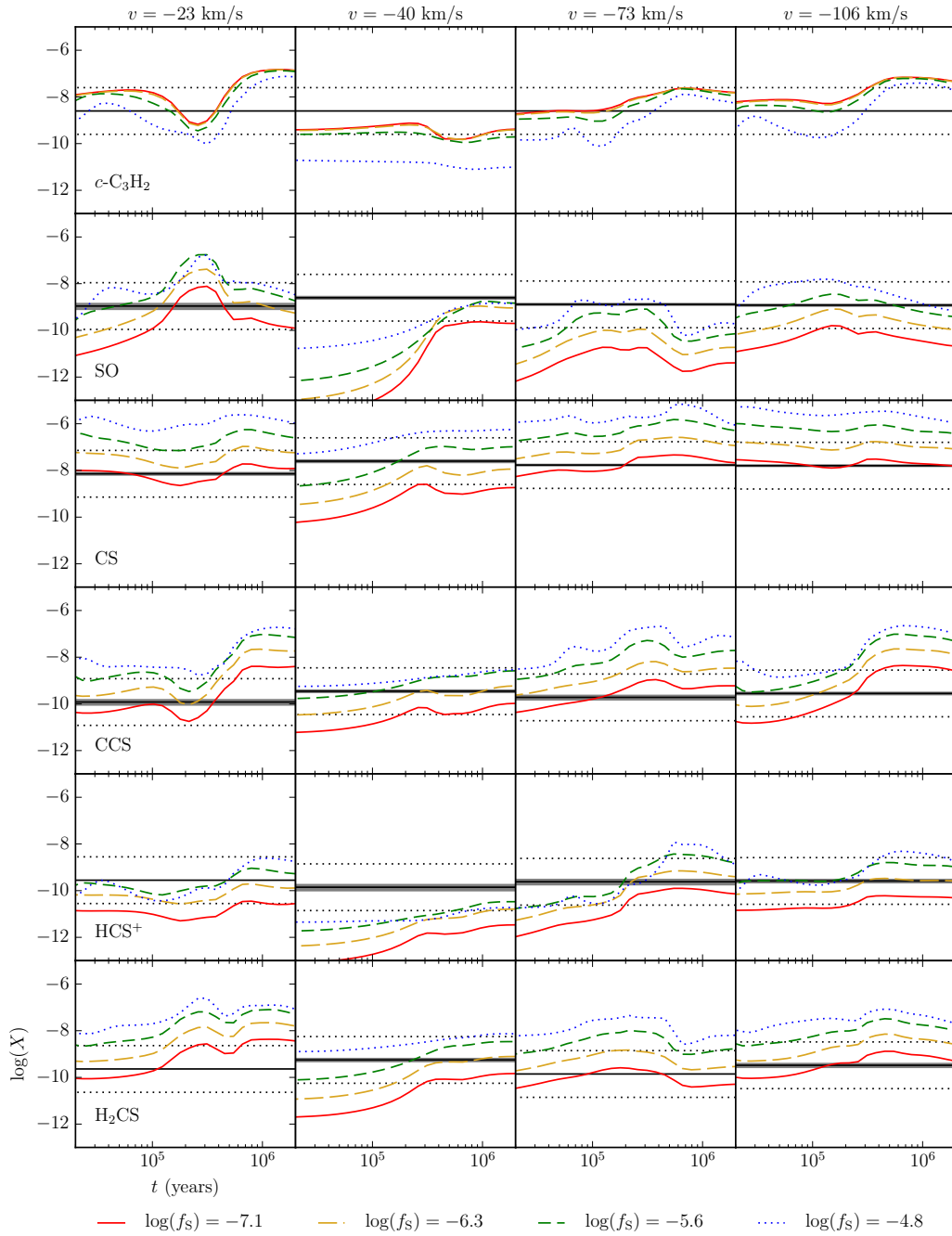


Figure 3.1: Time-dependent abundances $\log(X_{\text{mod}}(t))$ for each species in the fiducial models of each kinematic component. The fractional elemental abundance of sulfur, f_S , varies with dashed line style: solid ($f_S = 8 \times 10^{-8}$), long-dashed ($f_S = 5.1 \times 10^{-8}$), medium-dashed ($f_S = 1.0 \times 10^{-8}$), and short-dashed ($f_S = 1.5 \times 10^{-5}$). Observed abundances $\log(X_{\text{obs}}(t))$ appear as horizontal solid black lines.

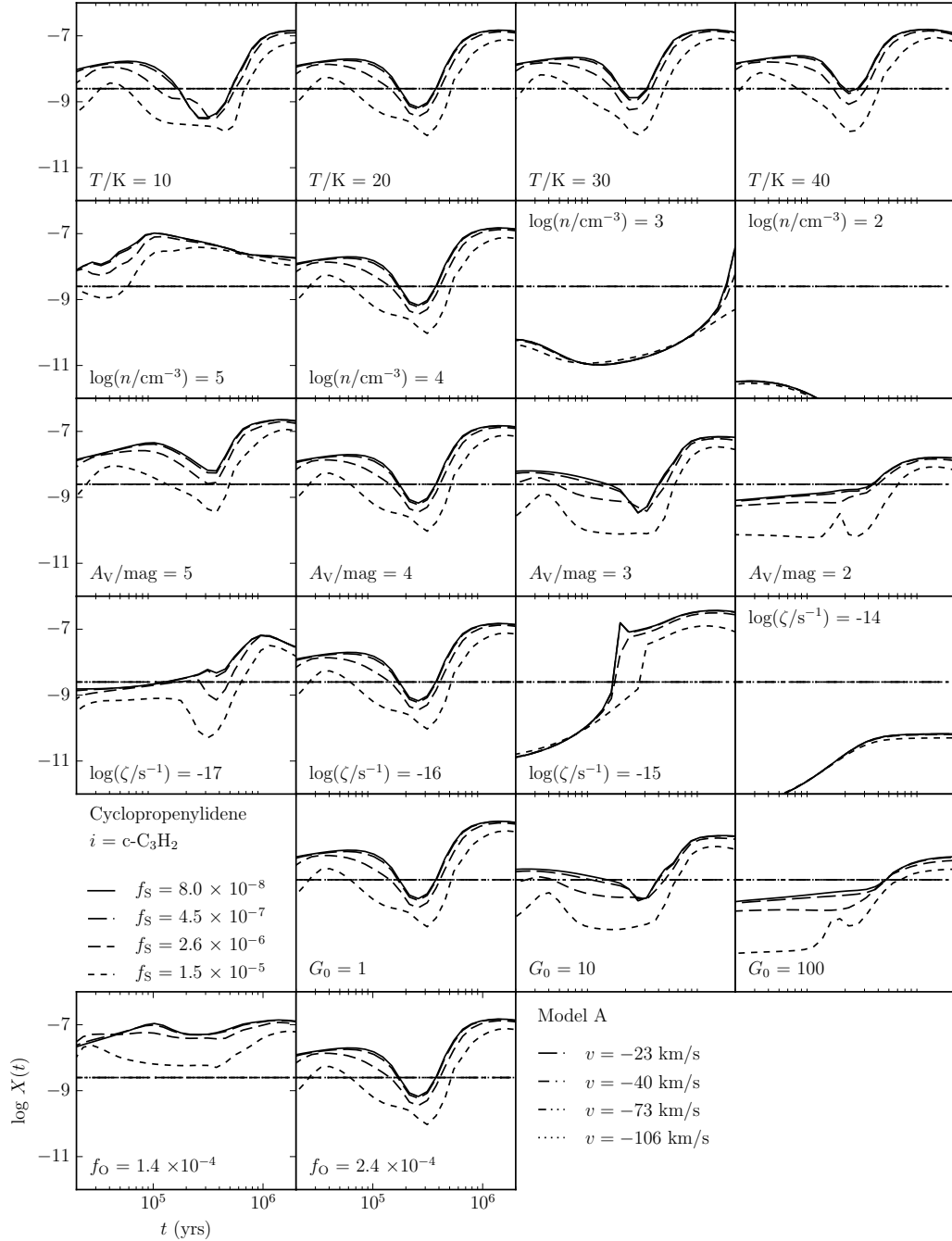


Figure 3.2: Time-dependent abundances $\log(X_{\text{mod}}(t))$ for cyclopropenylidene ($c\text{-C}_3\text{H}_2$). The fractional elemental abundance of sulfur, f_S , varies with dashed line style: solid ($f_S = 8 \times 10^{-8}$), long-dashed ($f_S = 5.1 \times 10^{-8}$), medium-dashed ($f_S = 1.0 \times 10^{-8}$), and short-dashed ($f_S = 1.5 \times 10^{-5}$). Observed abundances $\log(X_{\text{obs}}(t))$ appear as horizontal lines in black with dotted line style corresponding to absorption feature velocities: dot-dashed ($v = -23 \text{ km/s}$), dot-dot-dashed ($v = -40 \text{ km/s}$), dot-dot-dot-dashed ($v = -73 \text{ km/s}$), and dotted ($v = -106 \text{ km/s}$). Each row varies a single free parameter in the chemical model, and panels in the second column contain the same image to emphasize the fiducial model as the intersection around which each row expands.

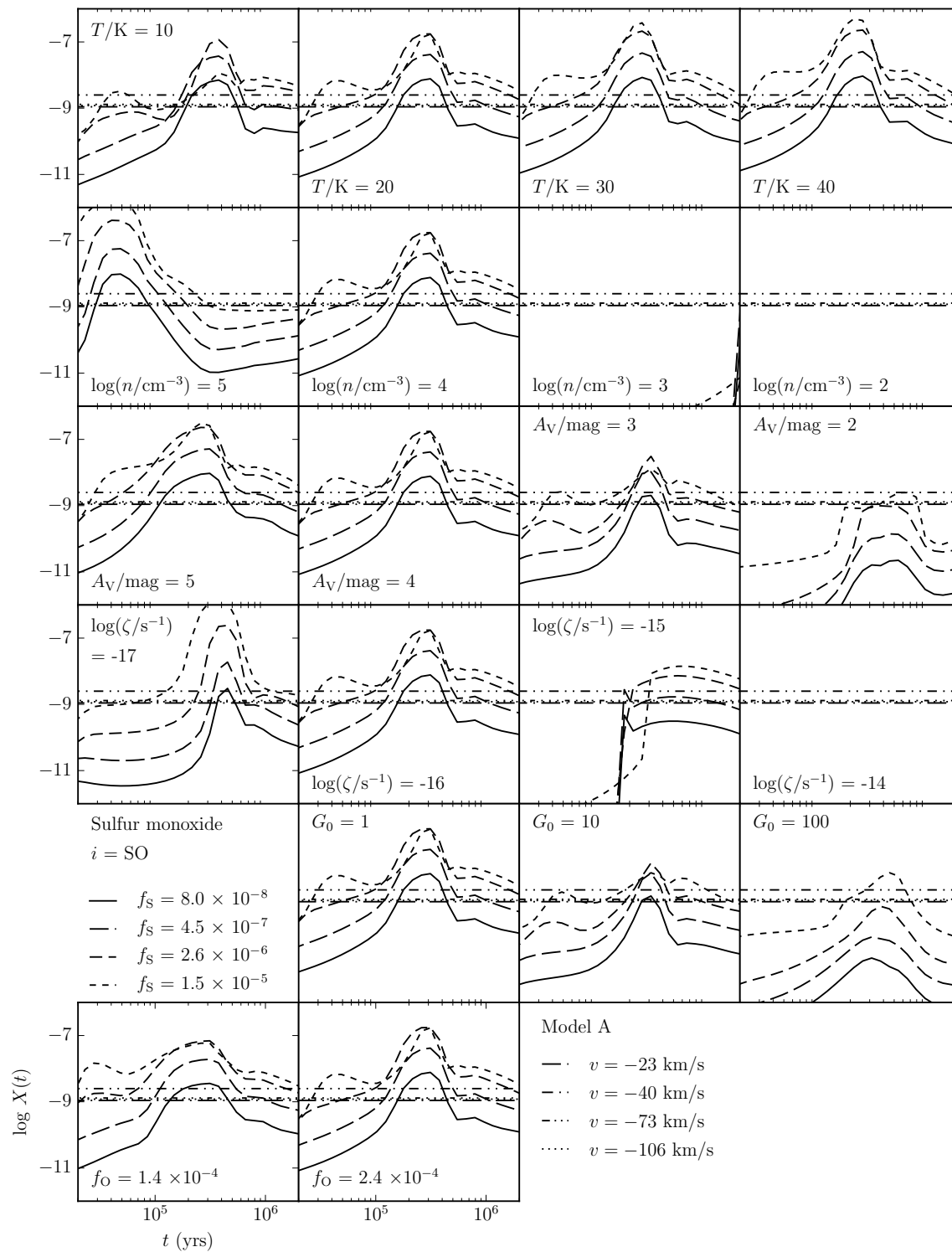


Figure 3.3: Same as Figure 3.2 but for sulfur monoxide, SO.

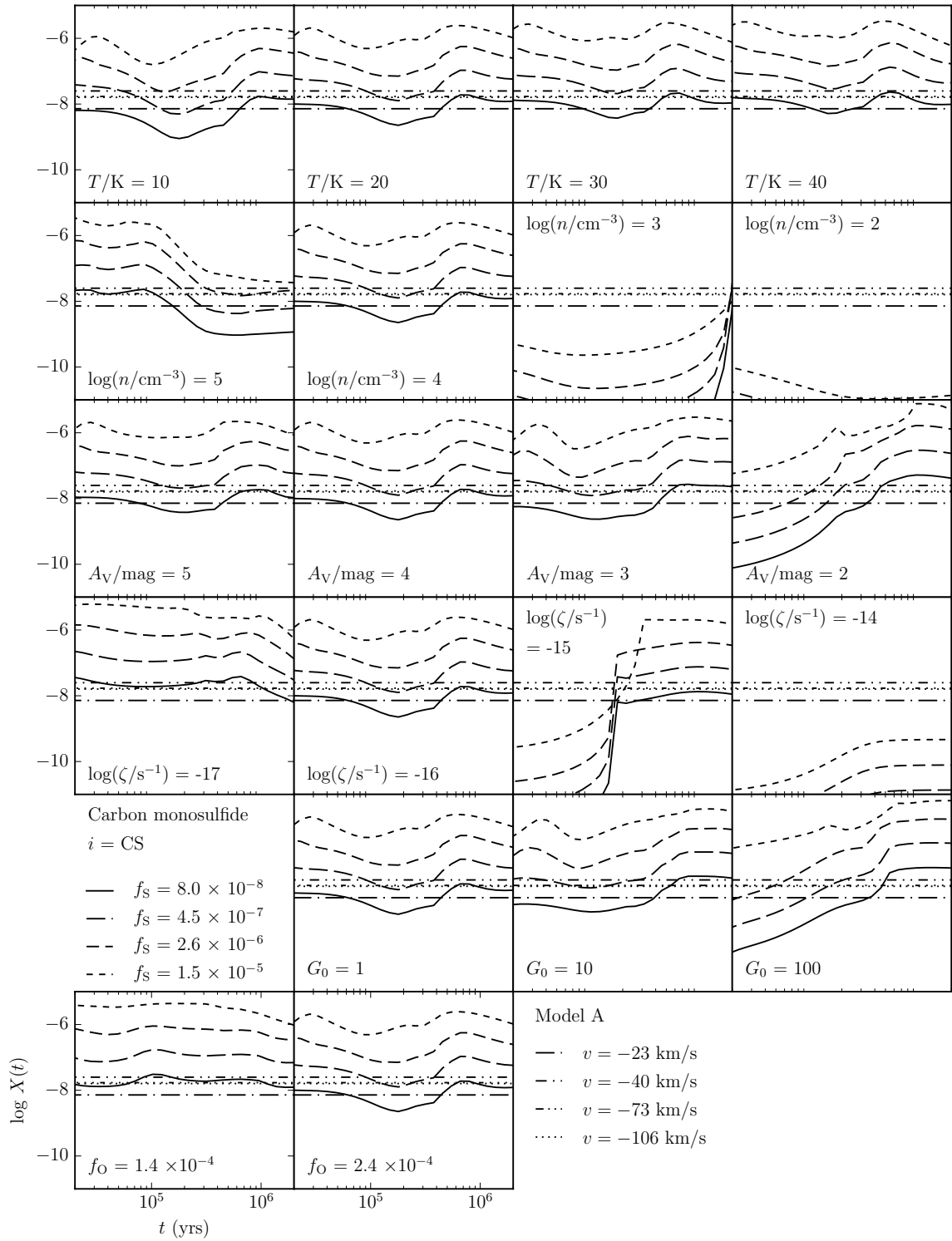


Figure 3.4: Same as Figure 3.2 but for carbon monosulfide, CS.

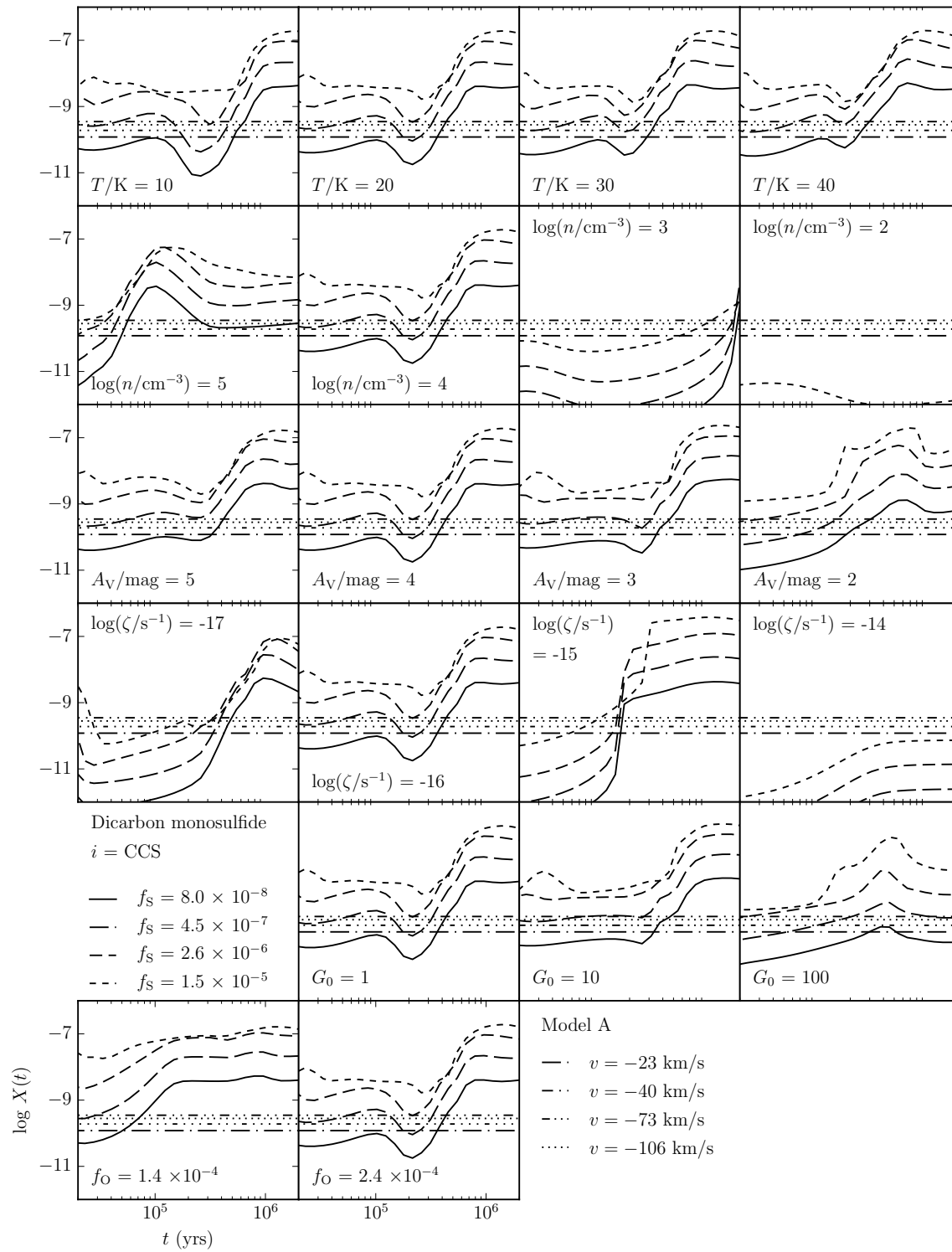
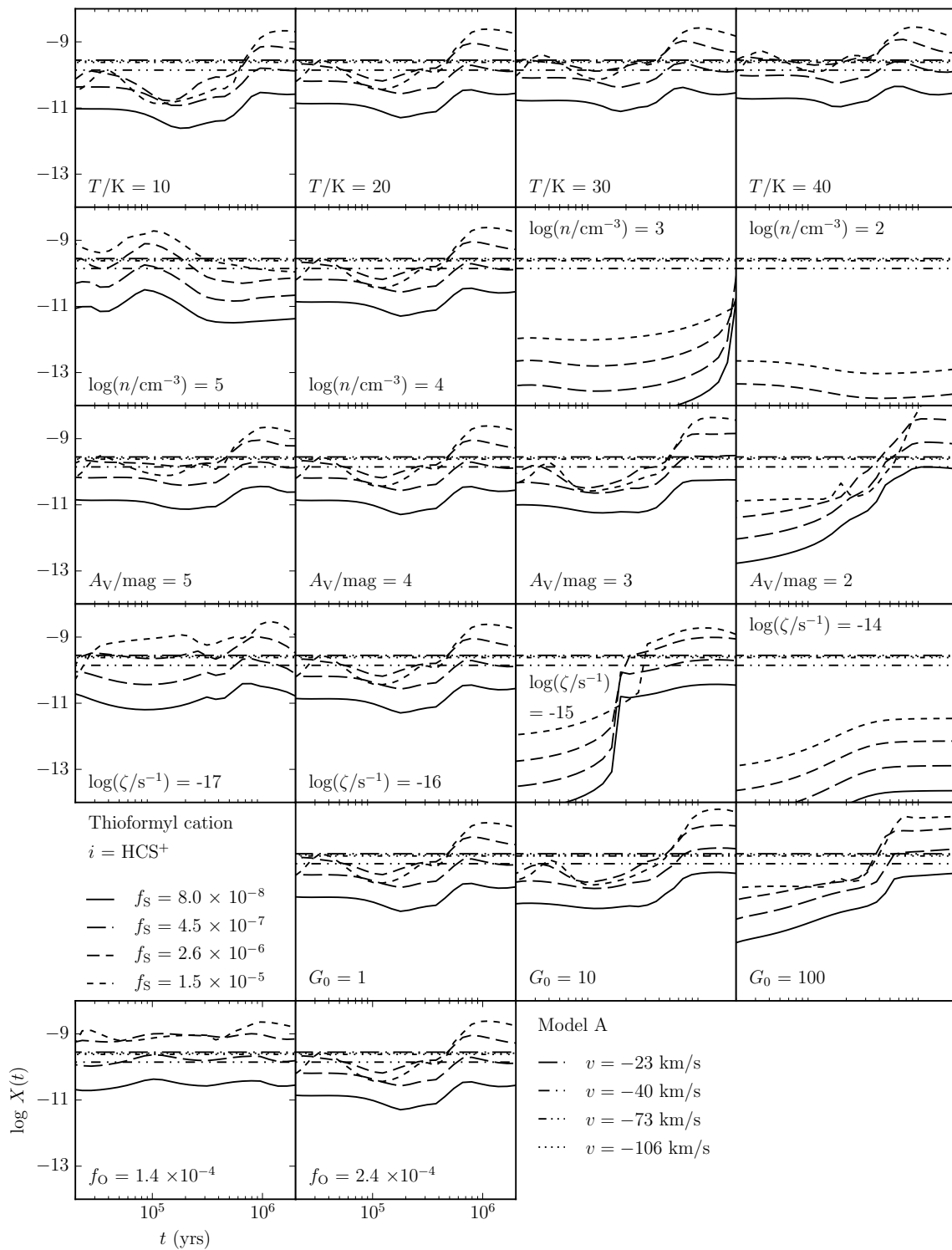
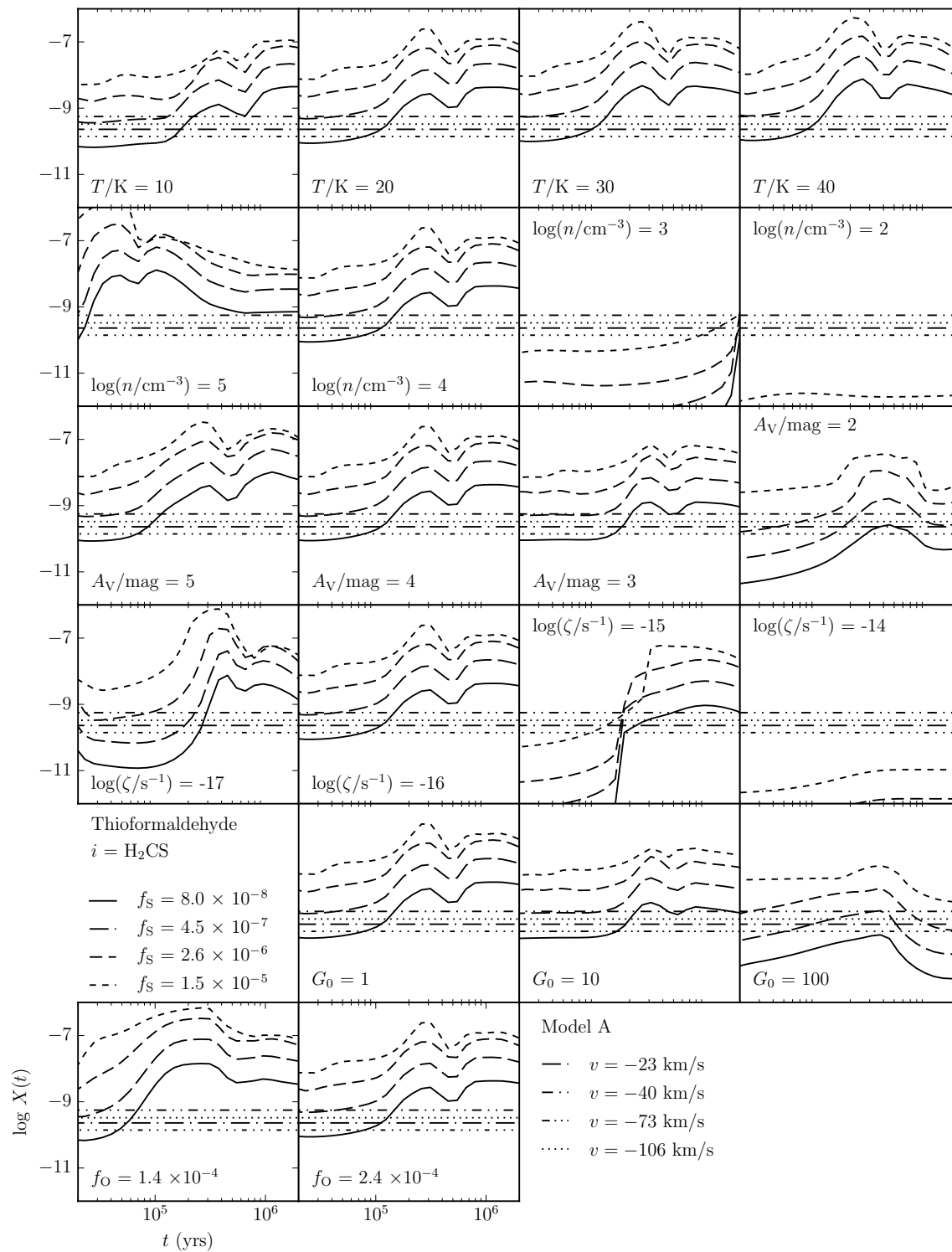


Figure 3.5: Same as Figure 3.2 but for dicarbon monosulfide, CCS.


 Figure 3.6: Same as Figure 3.2 but for the thioformyl cation HCS^+ .

Figure 3.7: Same as Figure 3.2 but for thioformaldehyde, H_2CS .

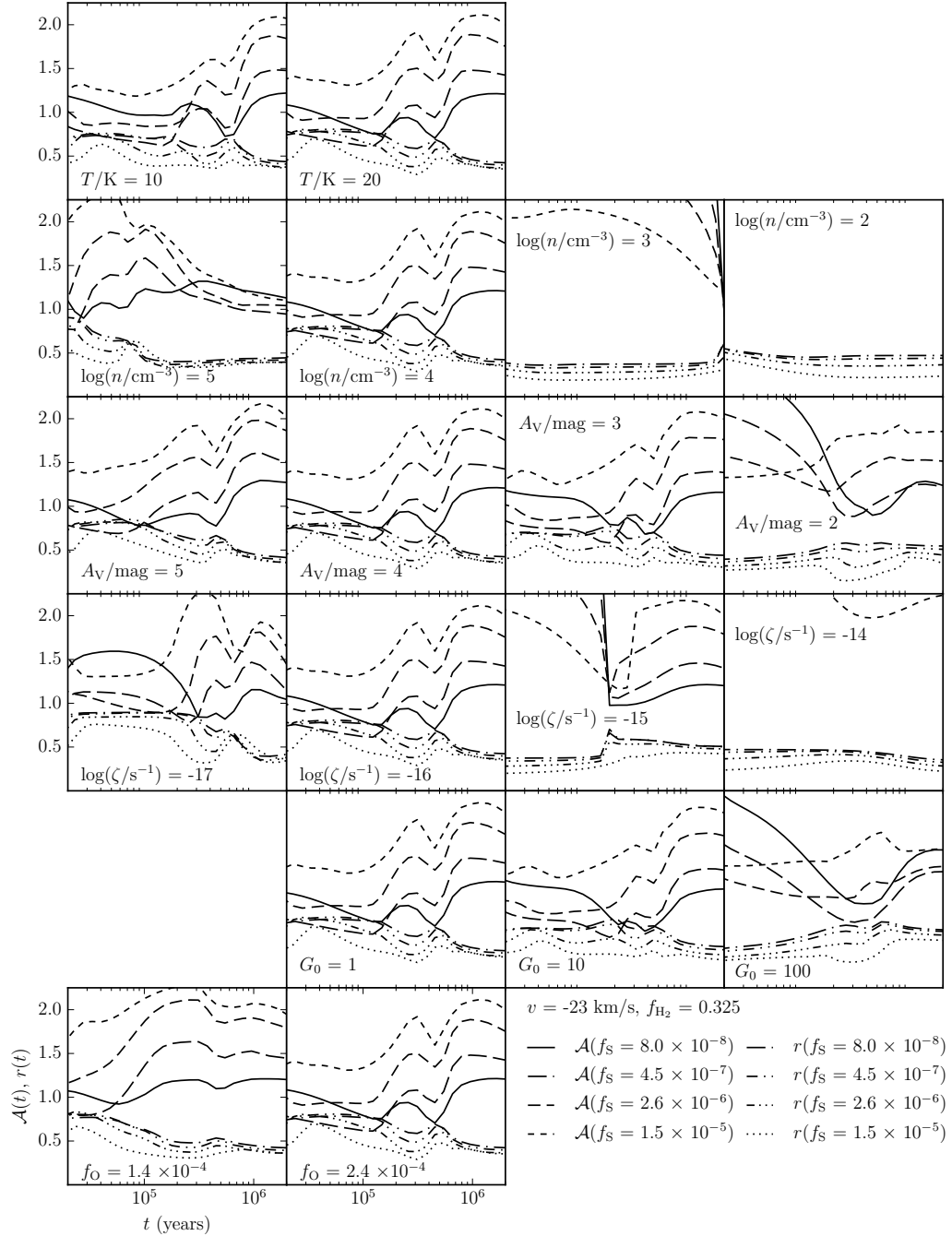
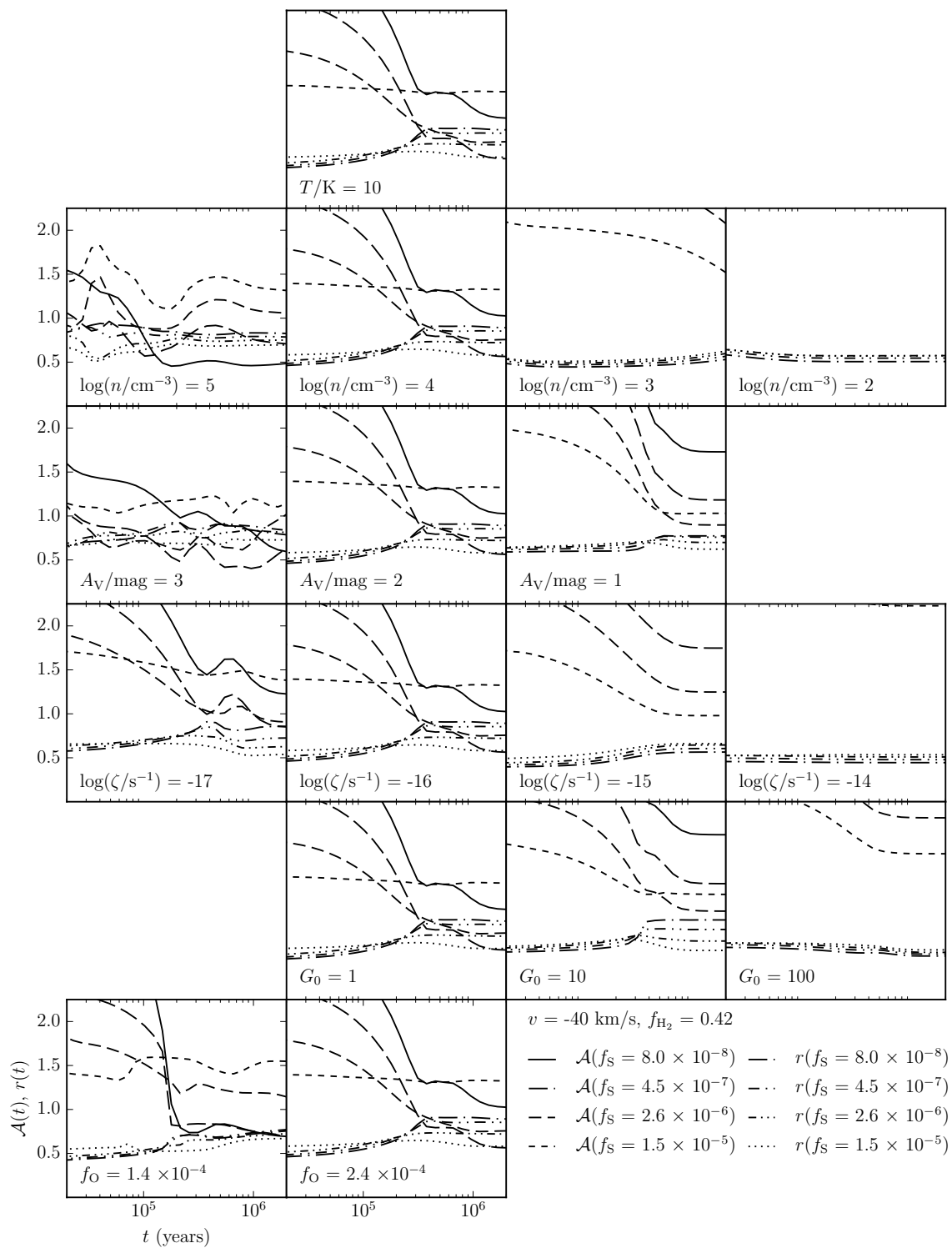


Figure 3.8: Time-dependent root-mean-squares $\mathcal{A}(t)$ and correlation coefficients $r(t)$ corresponding to the fiducial model of kinematic component $v = -23 \text{ km/s}$ with line style corresponding to fit type and fractional elemental abundance of sulfur: $\mathcal{A}(f_{\text{S}} = 8.0 \times 10^{-8})$ (solid), $\mathcal{A}(f_{\text{S}} = 5.0 \times 10^{-6})$ (long-dashed), $\mathcal{A}(f_{\text{S}} = 1.0 \times 10^{-5})$ (medium-dashed), $\mathcal{A}(f_{\text{S}} = 1.5 \times 10^{-5})$ (short-dashed), $r(f_{\text{S}} = 8.0 \times 10^{-8})$ (dot-dashed), $r(f_{\text{S}} = 5.0 \times 10^{-6})$ (dot-dot-dashed), $r(f_{\text{S}} = 1.0 \times 10^{-5})$ (dot-dot-dot-dashed), and $r(f_{\text{S}} = 1.5 \times 10^{-5})$ (dotted). Each row varies a single free parameters in the chemical model, and panels in the second column contain the same image to emphasize the fiducial model as the intersection around which each row expands.

Figure 3.9: Same as Figure 3.8 but for $v = -40$ km/s.

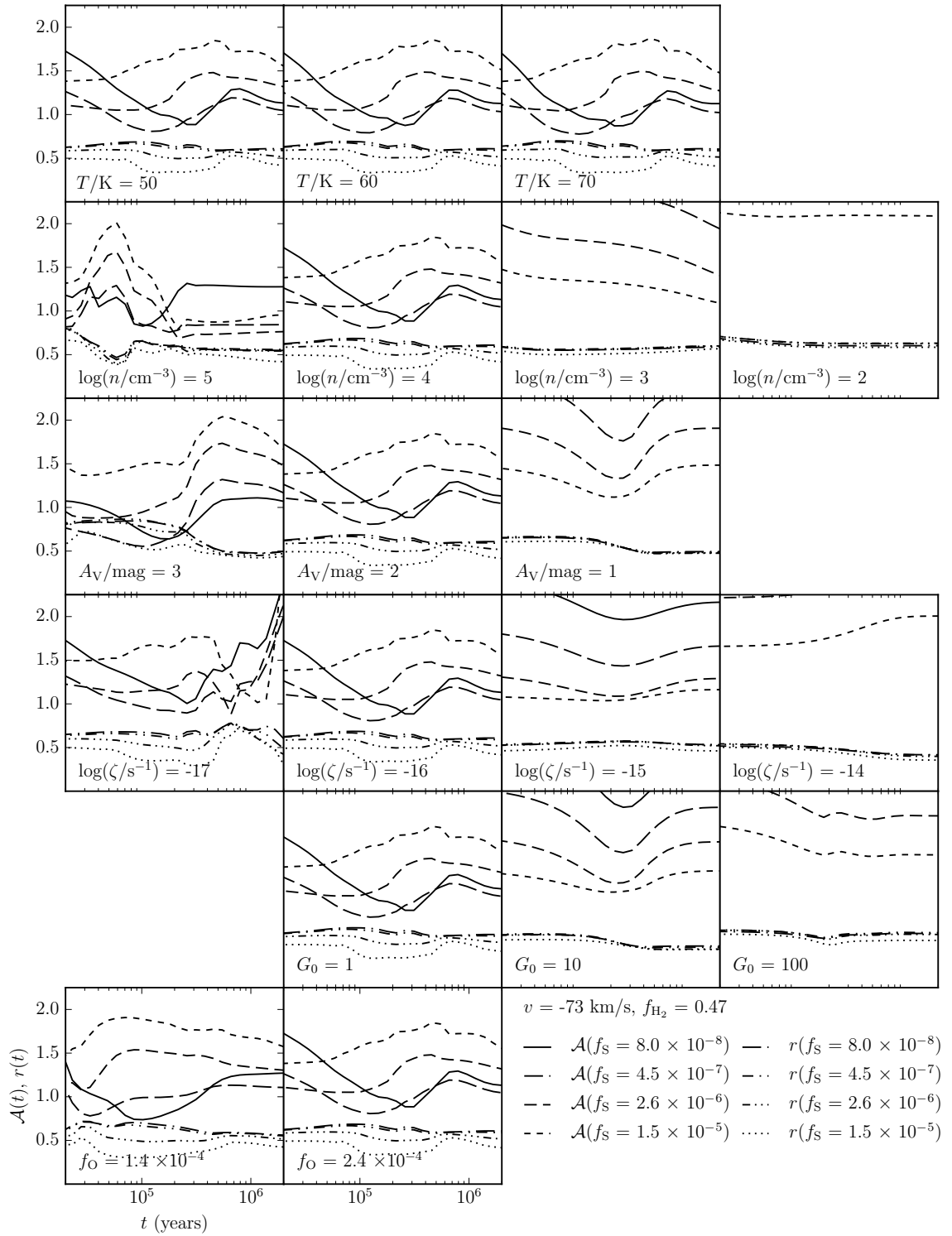
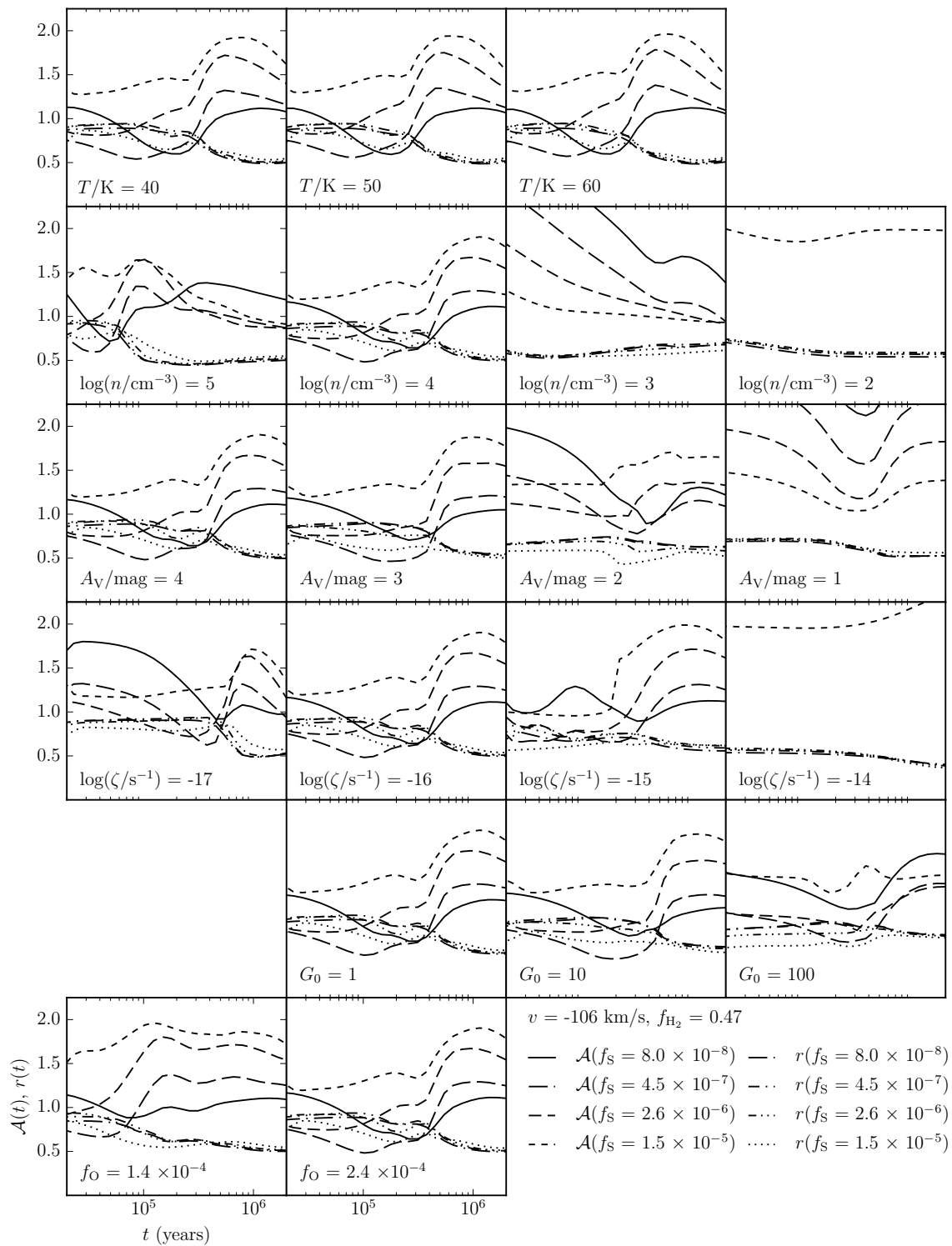


Figure 3.10: Same as Figure 3.8 but for $v = -73 \text{ km/s}$.

Figure 3.11: Same as Figure 3.8 but for $v = -106 \text{ km/s}$.

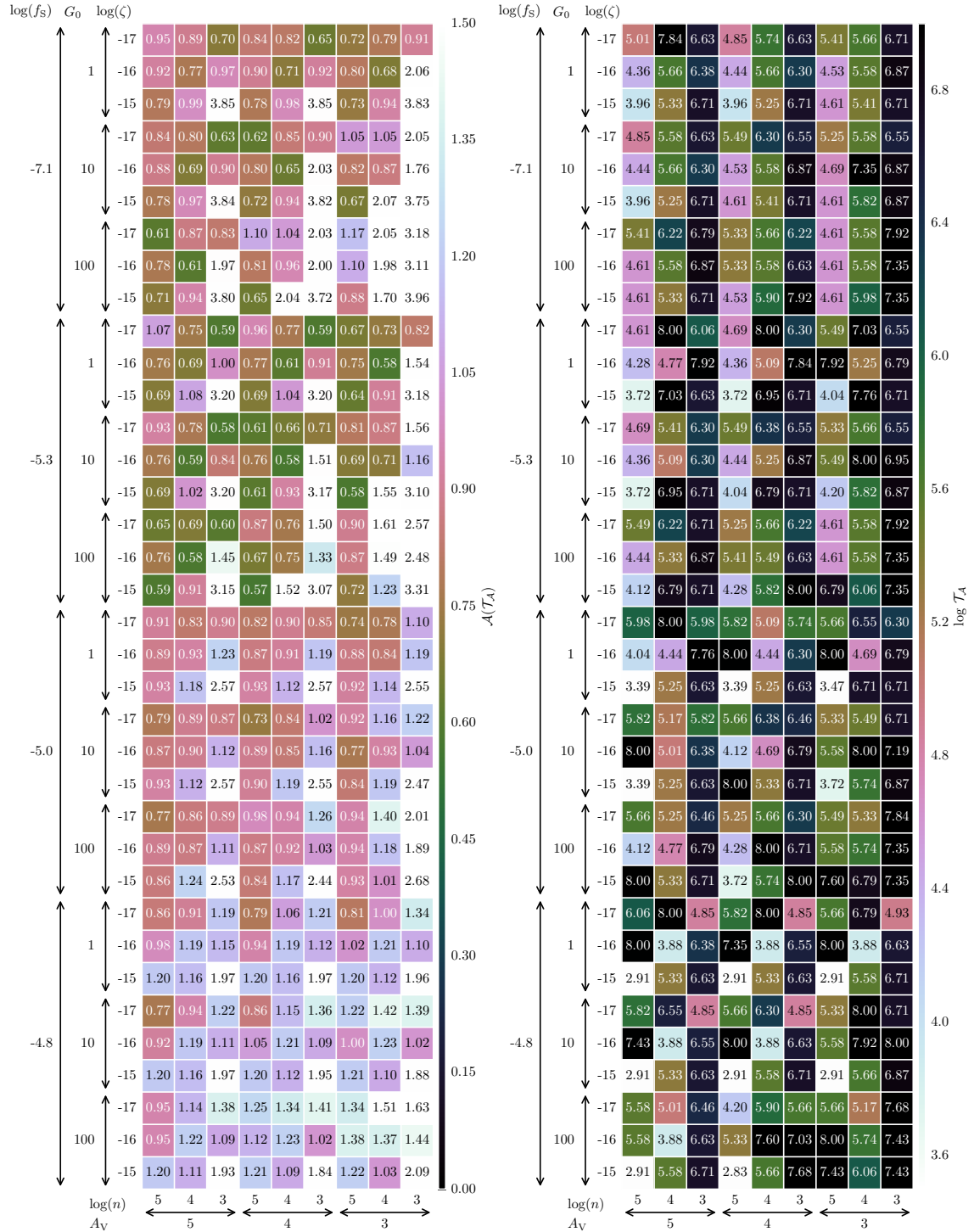
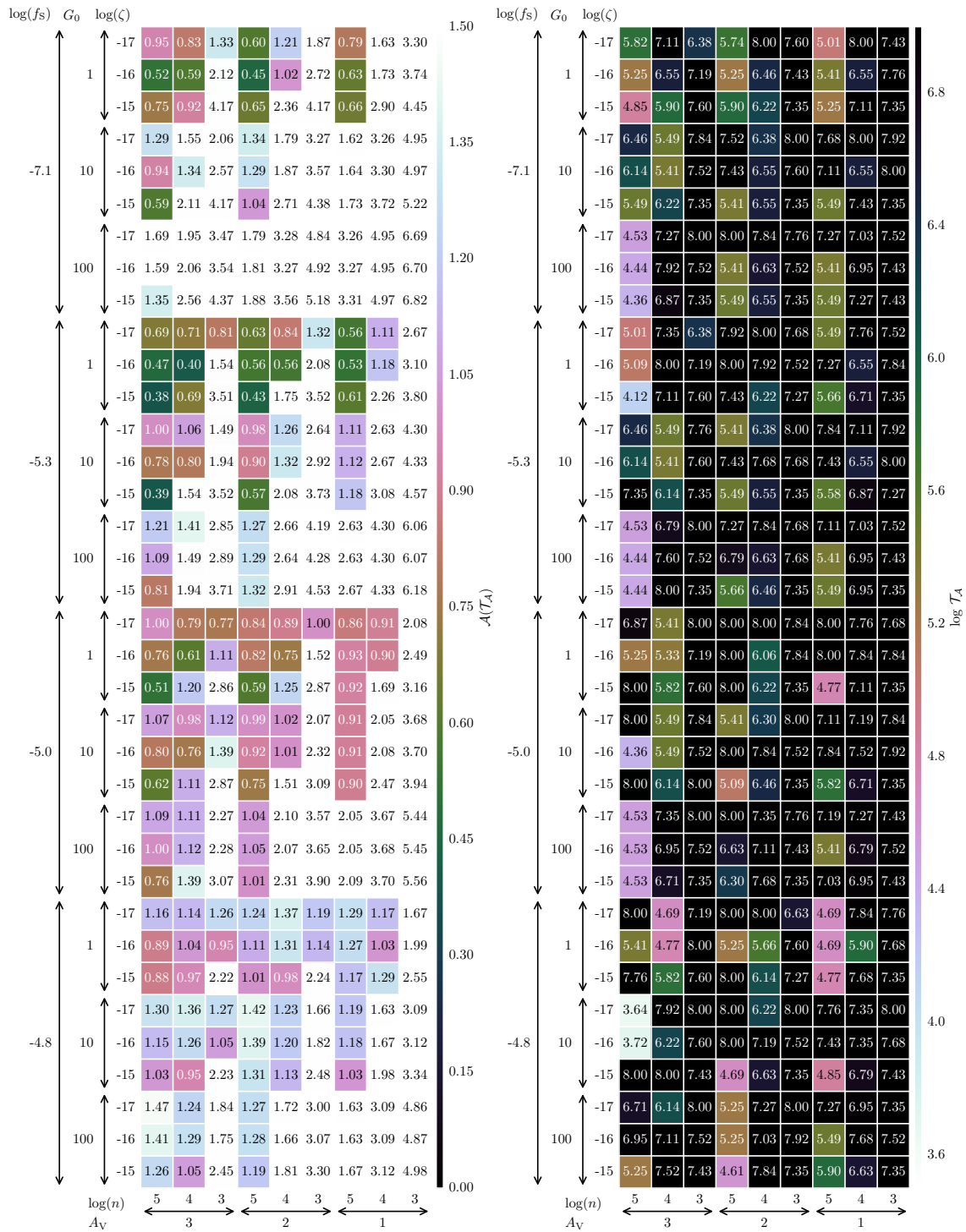


Figure 3.12: Minimum root-mean-square log differences $\mathcal{A}_{\min}(\mathcal{T}_A, p)$ (left) and best fit times $\log(\mathcal{T}_A)$ (right) between modeled abundances X_{mod} and observed abundances X_{obs} for kinematic component $v = -23$ km/s at temperature $T = 20$ K and fractional elemental abundance of oxygen $f_{\text{O}} = 2.4 \times 10^{-4}$.

Figure 3.13: Same as Figure 3.12 but for $v = -40$ km/s at temperature $T = 10$ K.

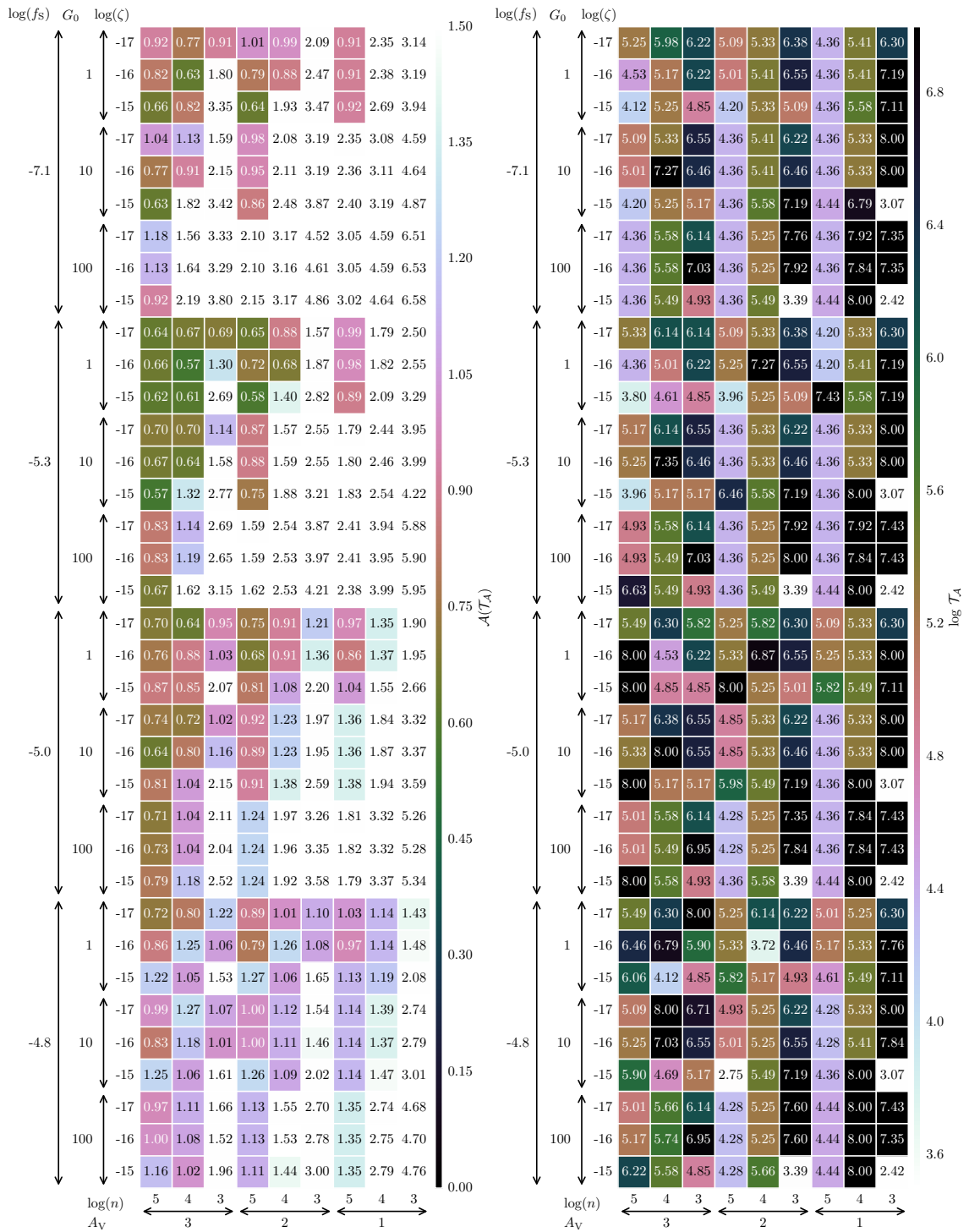
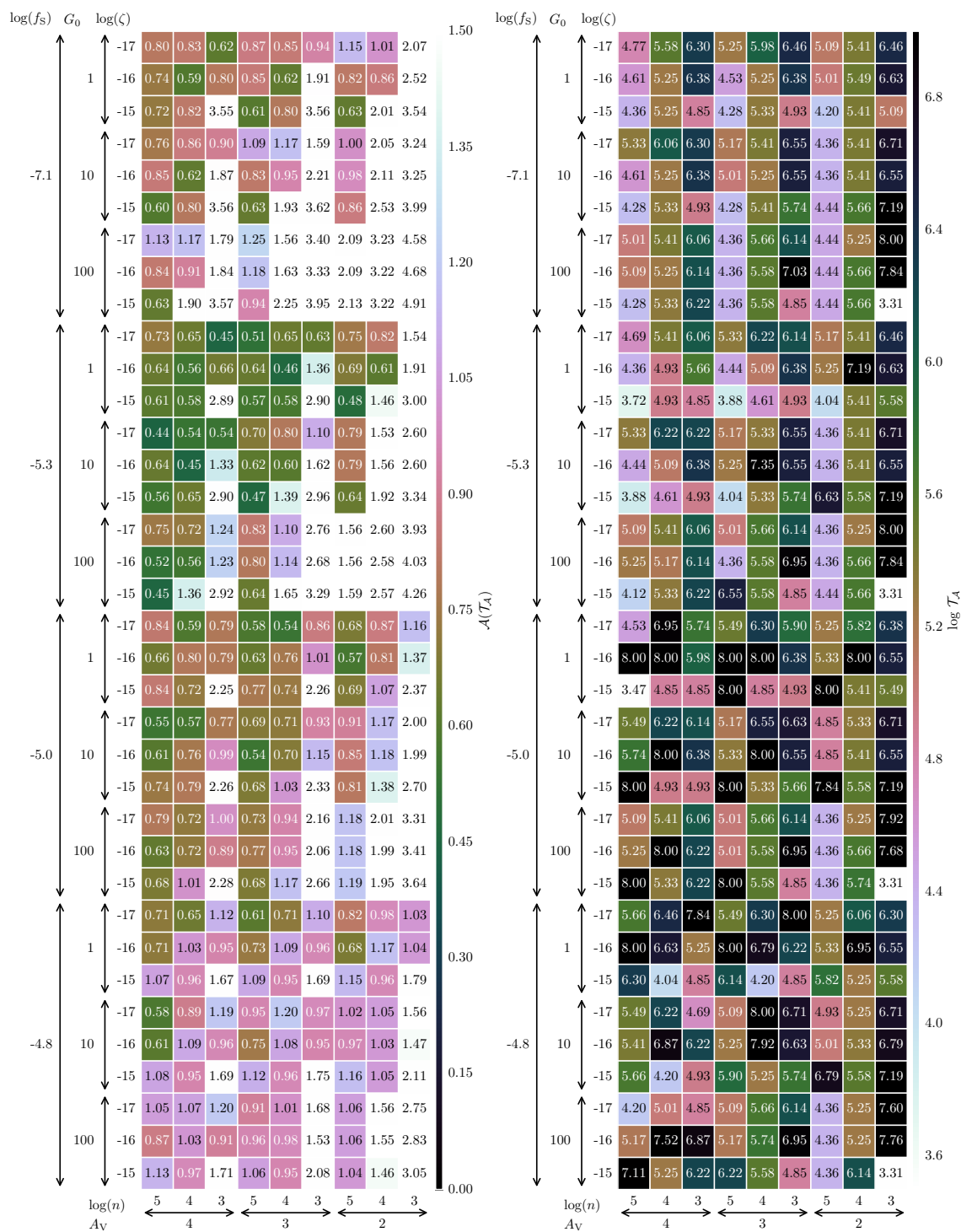


Figure 3.14: Same as Figure 3.12 but for $v = -73$ km/s.

Figure 3.15: Same as Figure 3.12 but for $v = -106$ km/s.

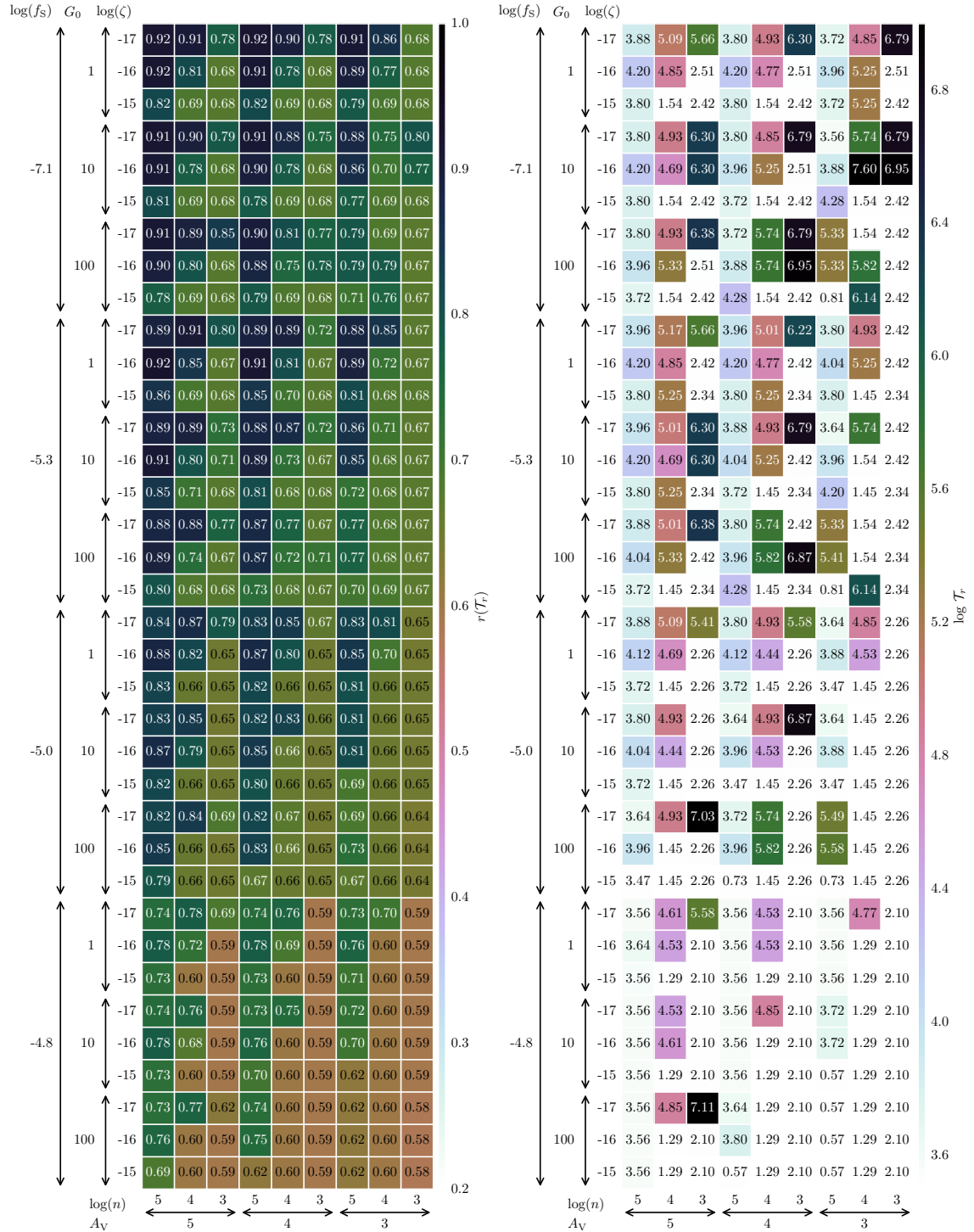
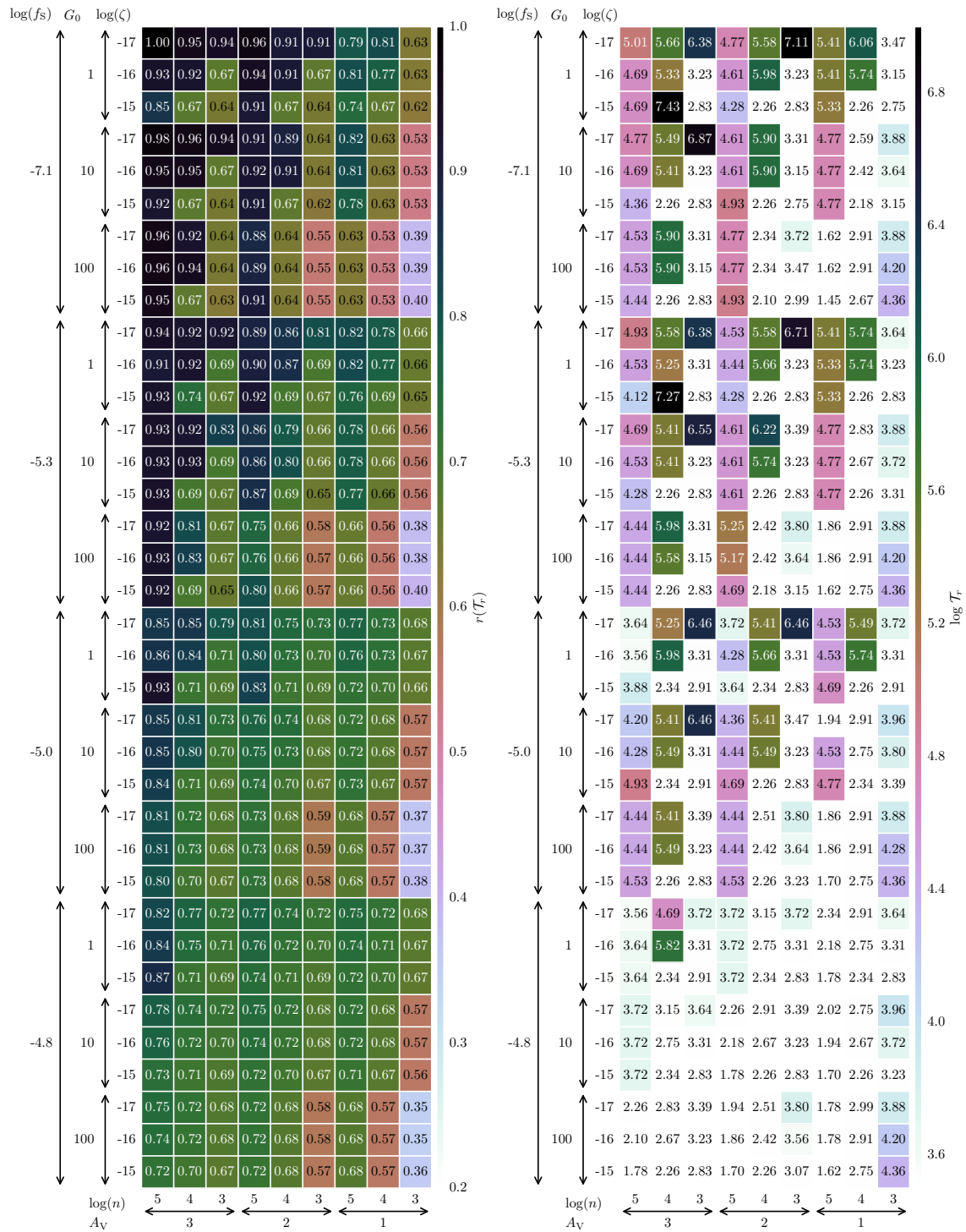


Figure 3.16: Maximum correlation coefficients $r_{\min}(\mathcal{T}_r, p)$ (left) and best fit times $\log(\mathcal{T}_r)$ (right) between modeled abundances X_{mod} and observed abundances X_{obs} for kinematic component $v = -23$ km/s at temperature $T = 20$ K and fractional elemental abundance of oxygen $f_{\text{O}} = 2.4 \times 10^{-4}$.

Figure 3.17: Same as Figure 3.16 but for $v = -40$ km/s at temperature $T = 10$ K.

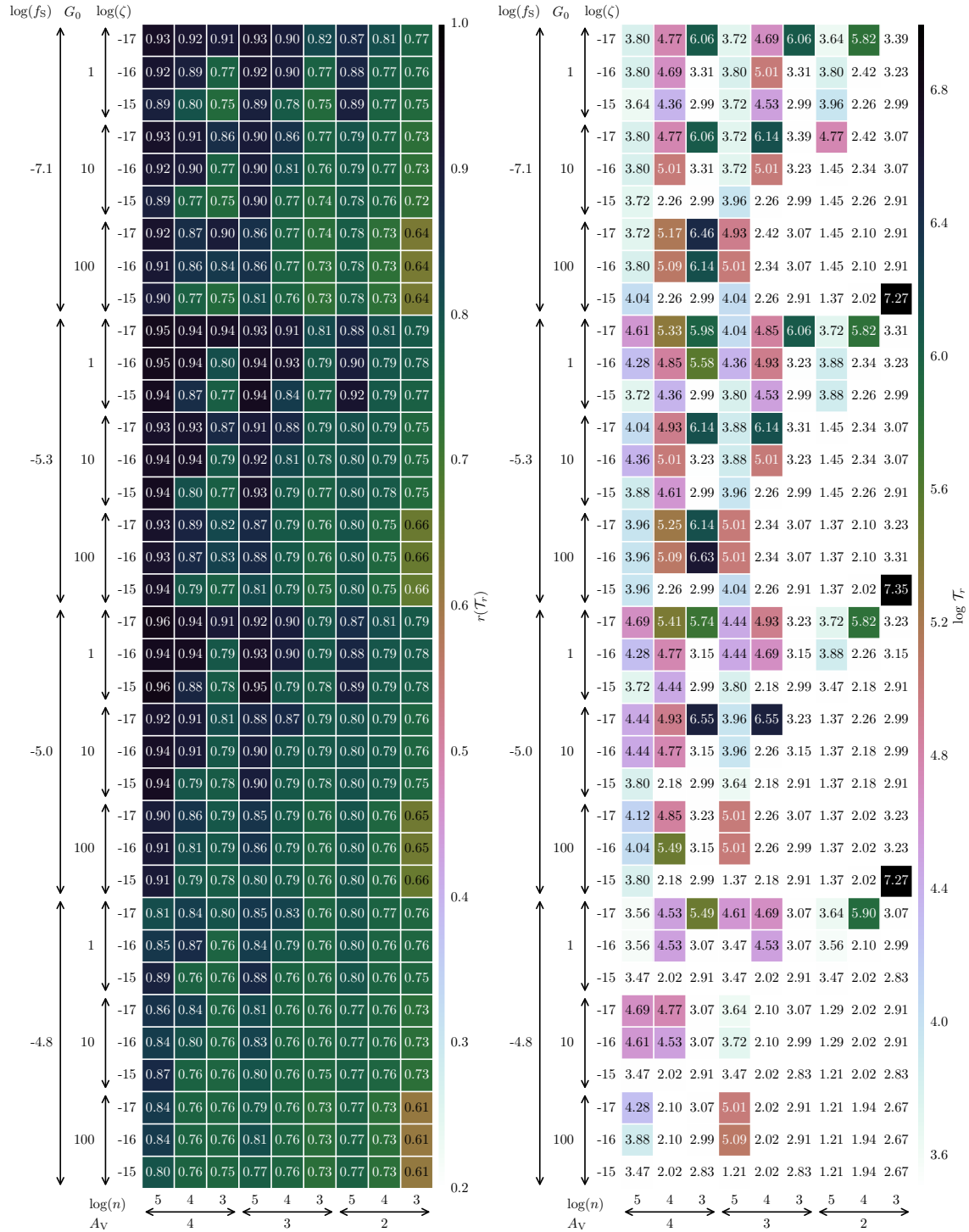


Figure 3.19: Same as Figure 3.16 but for kinematic component $v = -106$ km/s at temperature $T = 50$ K.



Figure 3.21: Same as Figure 3.20 but for $v = -40$ km/s at time $\log t = 6.46$, temperature $T = 10$ K.

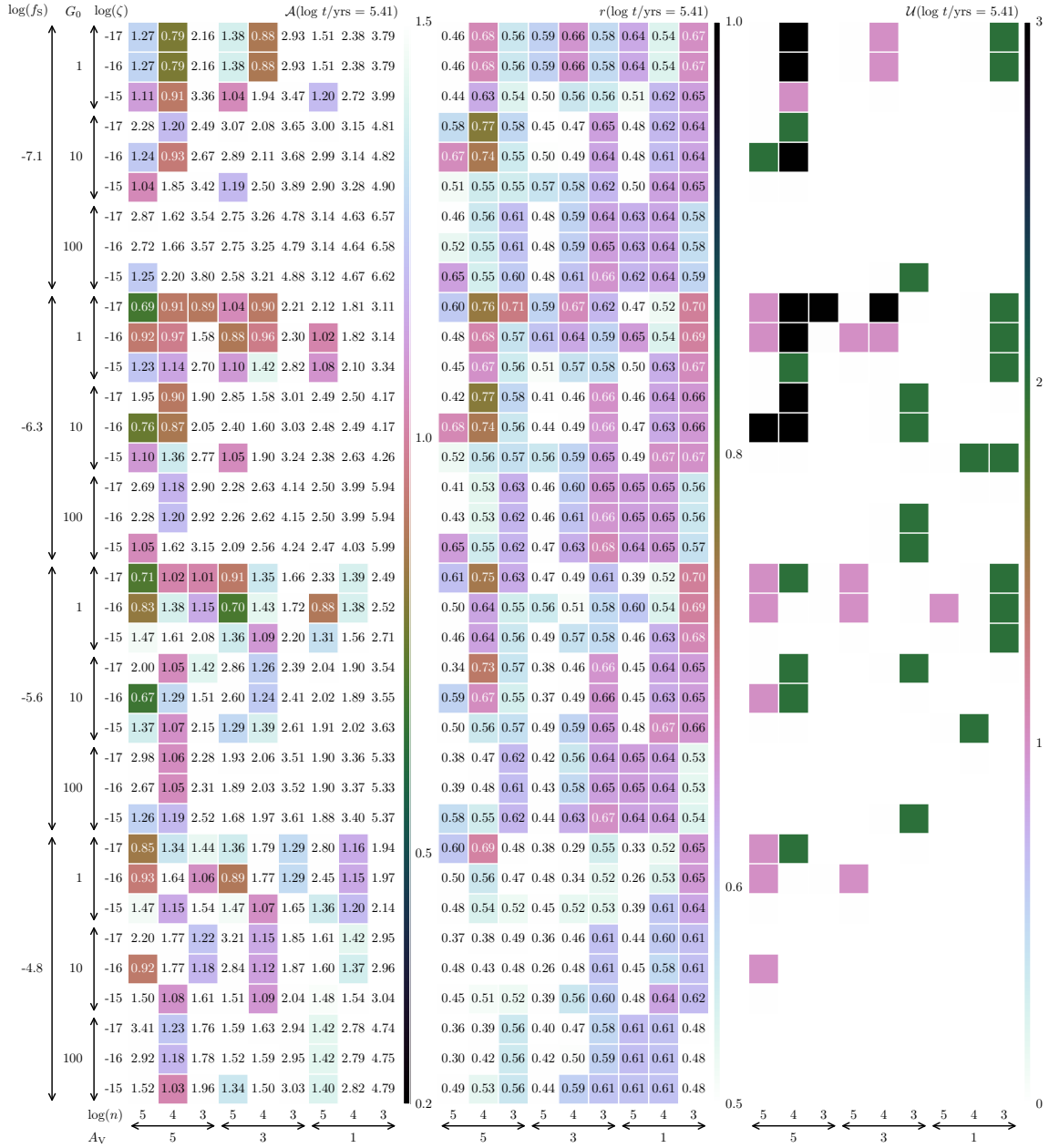


Figure 3.22: Same as Figure 3.20 but for $v = -73$ km/s at time $\log t = 5.41$, temperature $T = 60$ K.

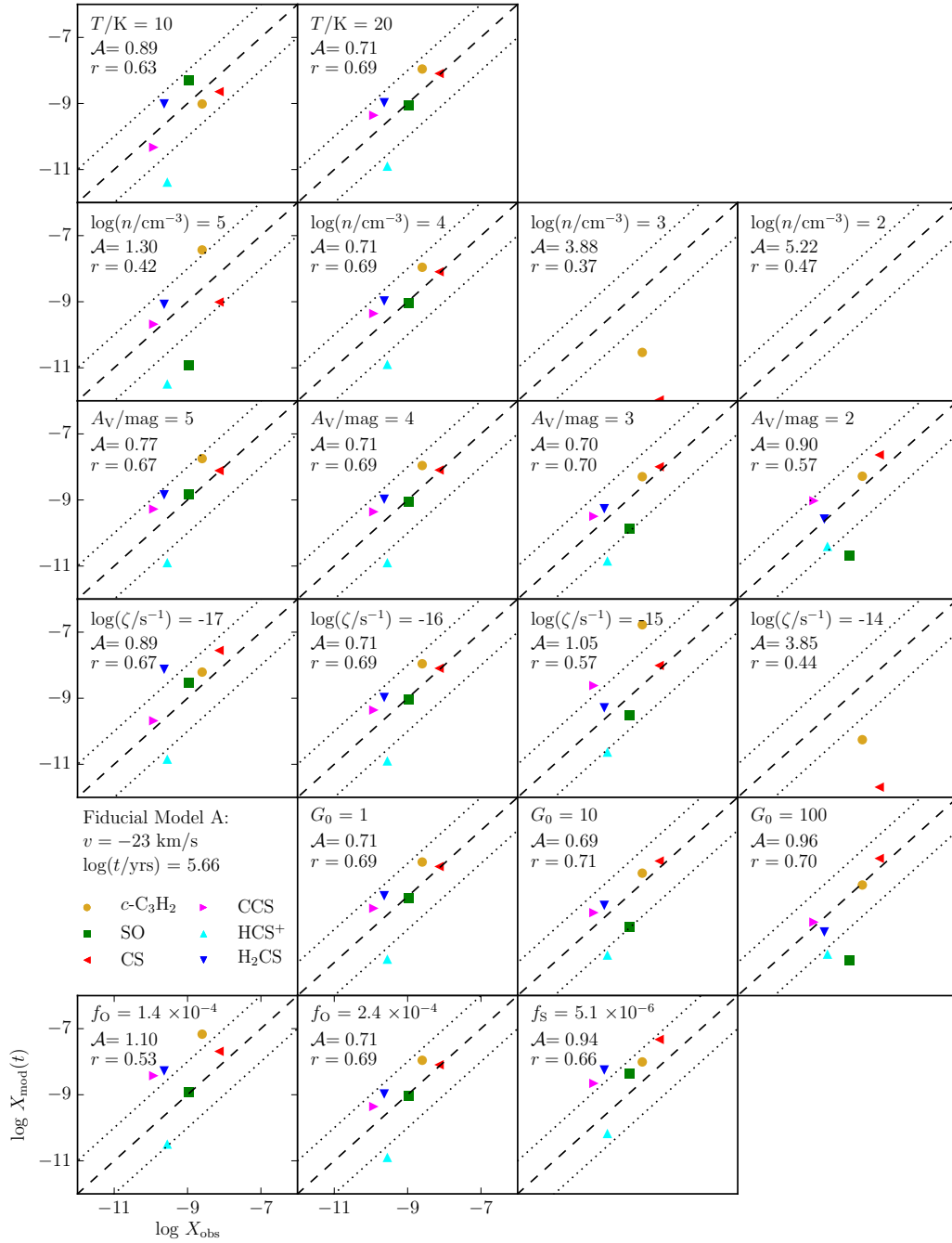


Figure 3.24: Scatter plots of modeled versus observed abundances, $\log(X_{\text{mod}}(t))$ and $\log(X_{\text{obs}}(v))$, for kinematic component $v = -23$ km/s at the best fit time $\log t = \log \mathcal{T}_{\mathcal{A}} = 5.66$ in the fiducial model. Each row varies a single free parameter in the chemical model, and panels in the second column contain the same image to emphasize the fiducial model as the intersection around which each row expands. Each panel displays the parameter varied from the fiducial model, the rms log abundance difference $\mathcal{A}(\mathcal{T}_{\mathcal{A}})$ and the correlation coefficient $r(\mathcal{T}_{\mathcal{A}})$. Diagonals represent the lines $\log X_{\text{mod}} = \log X_{\text{obs}}$ (dashed) and $\log X_{\text{mod}} = \pm \log X_{\text{obs}}$ (dotted).

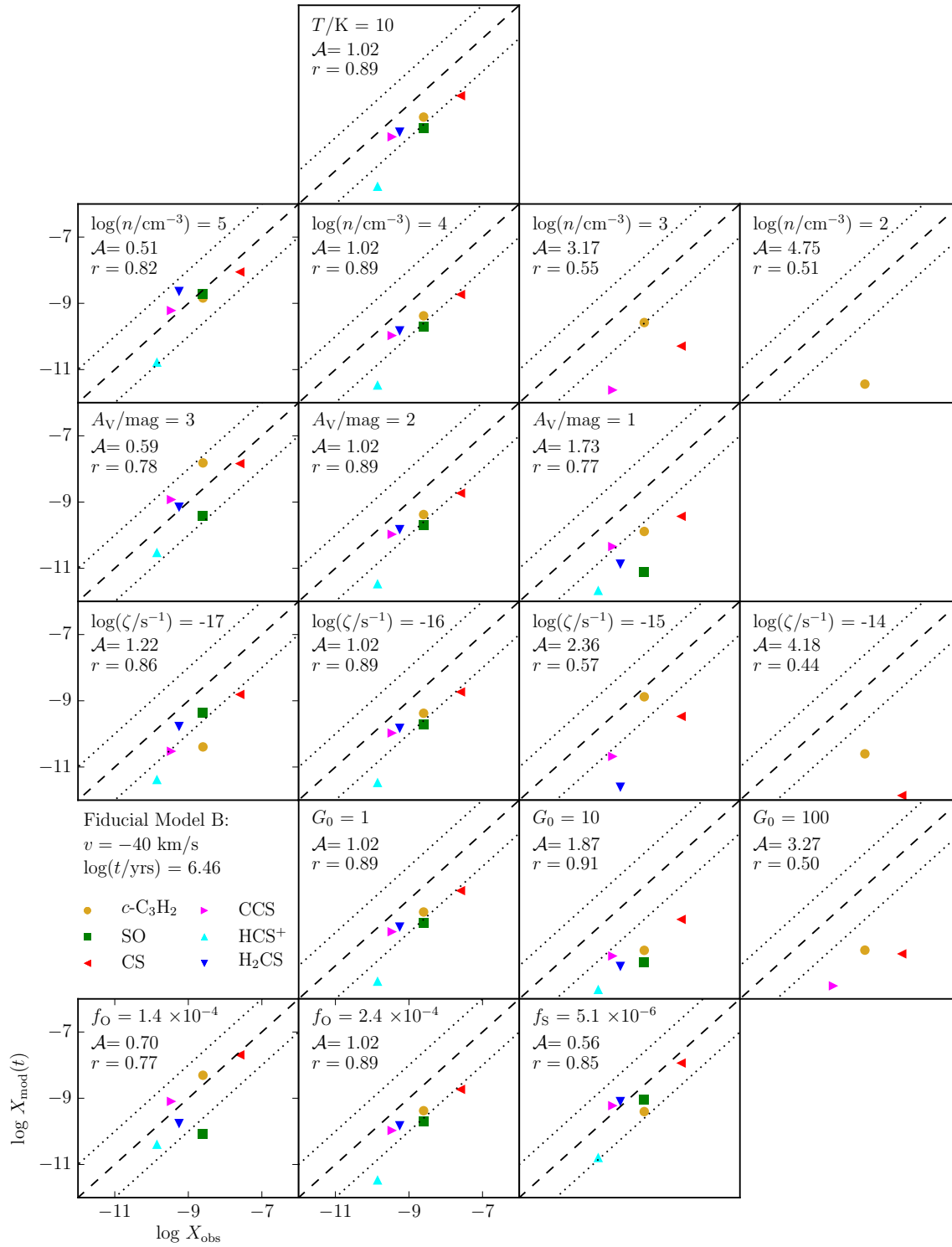


Figure 3.25: Same as Figure 3.24 but for kinematic component $v = -40$ km/s at the best fit time $\log t = \log \mathcal{T}_A = 6.46$.

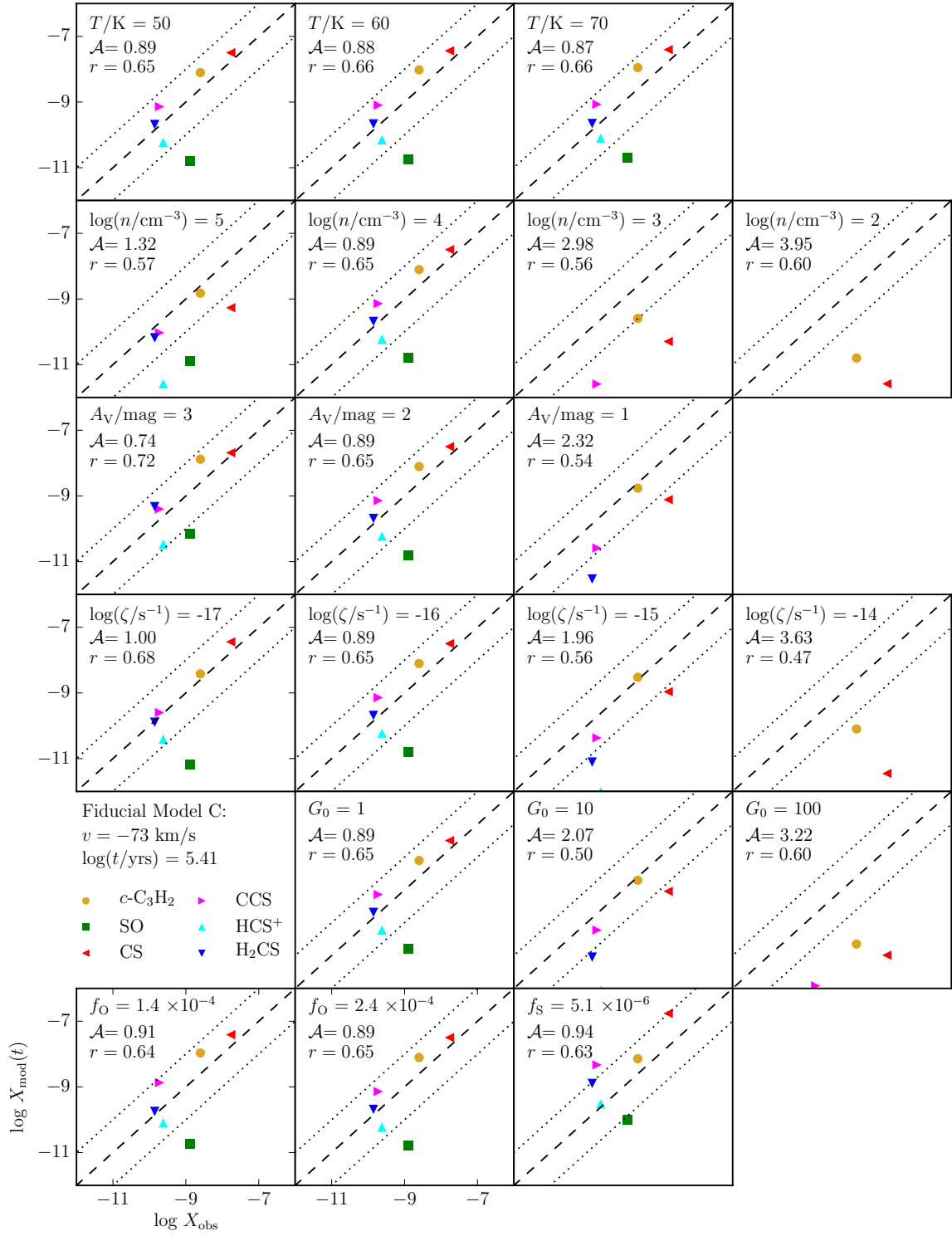


Figure 3.26: Same as Figure 3.24 but for kinematic component $v = -73$ km/s at the best fit time $\log t = \log \mathcal{T}_A = 5.41$.

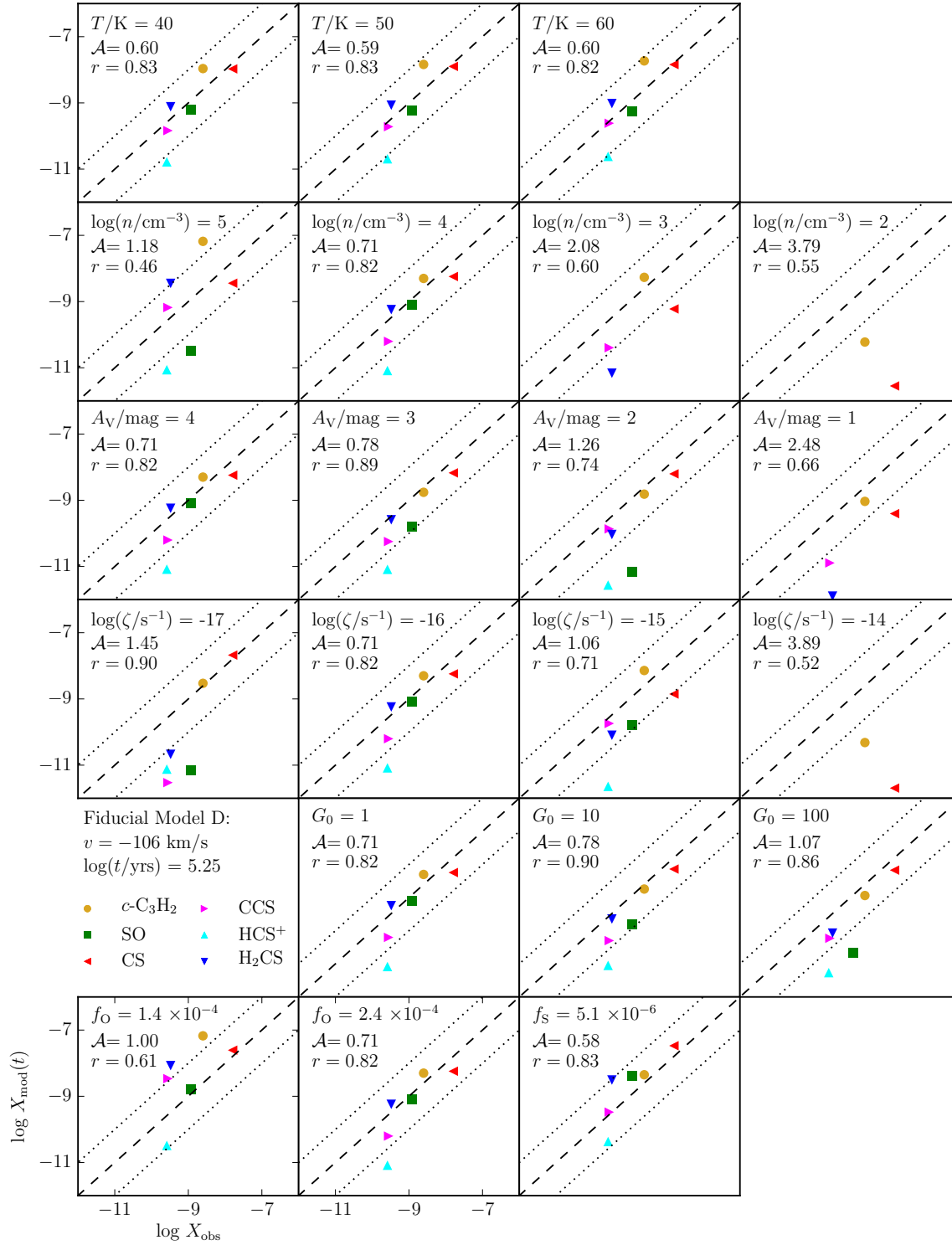


Figure 3.27: Same as Figure 3.24 but for kinematic component $v = -106 \text{ km/s}$ at the best fit time $\log t = \log \mathcal{T}_A = 5.25$.

Table 3.1: Calculated quantities from absorption line surveys of kinematic components toward Sagittarius B2 and fiducial model parameters

v (km s ⁻¹)	-23	-40	-73	-106
T_{kin} (K) ⁽¹⁾	15 ± 5	11 ± 2	58 ± 10	45 ± 7
N_{H} (× 10 ²¹ cm ⁻³) ⁽²⁾	8.36	3.74	3.96	5.72
A_{V} (mag)	3.8	1.7	1.8	2.6
d (kpc) ⁽³⁾	3.8	5.2	8.3	8.3
$s_{1\text{GHz}}$ (pc)	14	20	31	31
$s_{50\text{GHz}}$ (pc)	0.28	0.38	0.60	0.60

References — (1) Tieftrunk et al. (1994); (2) Corby et al. (2018); (3) Indriolo et al. (2015);

Table 3.2: Parameter Space for Grid Model

Parameter	Values
T_{gas} (K)	10, 20, 30, 40, 50, 60, 70
n_{T} (cm^{-3})	10^5 , 10^4 , 10^3 , 10^2
A_{V} (mag)	5, 4, 3, 2, 1
ζ (s^{-1})	10^{-17} , 10^{-16} , 10^{-15} , 10^{-14} , 10^{-13}
T_{dust} (K)	10, 20
G_0	1, 10, 100

Table 3.3: Fractional Elemental Abundances with Respect to Hydrogen Nuclei

Species	Value	Reference
H ₂	0.325, 0.42, 0.47	*
H	0.45, 0.16, 0.06	*
O	1.4(-4), 2.4(-4)	2
N	6.2(-5)	3
C	1.7(-4)	3
S	8.0(-8), 5.0(-7), 2.5(-6), 1.5(-5)	*
Si	8.0(-9)	4
Fe	3.0(-9)	4
Na	2.0(-9)	4
Mg	7.0(-9)	4
P	2.0(-10)	4
Cl	1.0(-9)	4
F	6.68(-9)	5

Table 3.4: Observed Relative Molecular Abundances with Respect to Molecular Hydrogen and Time-dependent Abundance Characters \mathcal{C}

Species	v (km/s)	$\log(X_o)$	\mathcal{C}
<i>c</i> -C ₃ H ₂	-23	-8.60	2
	-40	-8.60	1
	-73	-8.60	1, 3
	-106	-8.60	1, 3
SO	-23	-9.0 ± 0.1	2
	-40	-8.60 ± 0.05	3
	-73	-8.89 ± 0.03	2, 3
	-106	-8.92 ± 0.04	2
CS	-23	-8.14 ± 0.05	1, 4
	-40	-7.60 ± 0.05	2, 3
	-73	-7.77 ± 0.03	1, 4
	-106	-7.80 ± 0.03	1, 4
CCS	-23	-9.9 ± 0.1	3, 4
	-40	-9.46 ± 0.05	2, 3
	-73	-9.72 ± 0.09	2, 3
	-106	-9.55 ± 0.05	3
HCS ⁺	-23	-9.55^*	1, 4
	-40	-9.9 ± 0.1	1, 3
	-73	-9.6 ± 0.1	1, 3
	-106	-9.59 ± 0.07	1, 3
H ₂ CS	-23	-9.64^*	2, 3, 4
	-40	-9.25 ± 0.06	1, 3
	-73	-9.85^*	1, 2
	-106	-9.48 ± 0.08	1, 2

Table 3.5: Calculated quantities from absorption line surveys of kinematic components toward Sagittarius B2 and fiducial model parameters

v (km s ⁻¹)	-23	-40	-73	-106
T_{kin} (K)	20	10	60	50
$\log(n/\text{cm}^{-3})$	4	4	4	4
A_V (mag)	4	2	2	3
$\log(\zeta/\text{s}^{-1})$	-16	-16	-16	-16
G_0	1	1	1	1
$\log(f_O)$	-3.6	-3.6	-3.6	-3.6
$\log(f_S)$	-7.1	-7.1	-7.1	-7.1
\mathcal{A}_{min}	0.705	1.024	0.875	0.623
$\log(\mathcal{T}_A)$	5.657	6.465	5.414	5.253
$r(\mathcal{T}_A)$	0.691	0.892	0.659	0.864
r_{max}	0.783	0.909	0.750	0.899
$\log(\mathcal{T}_r)$	4.768	5.980	2.101	5.010
$\mathcal{A}(\mathcal{T}_r)$	0.903	1.152	3.813	0.746
T_{kin} (K)	20	10	50	40
$\log(n/\text{cm}^{-3})$	4	4	4	3
A_V (mag)	4	3	3	4
$\log(\zeta/\text{s}^{-1})$	-16	-17	-16	-17
G_0	10	1	1	1
$\log(f_O)$	-3.6	-3.9	-3.6	-3.6
$\log(f_S)$	-4.8	-7.1	-6.3	-6.3
\mathcal{A}_{min}	0.577	0.391	0.554	0.433
$\log(\mathcal{T}_A)$	5.253	7.030	5.010	6.141
$r(\mathcal{T}_A)$	0.727	0.877	0.858	0.920
T_{kin} (K)	10	10	60	50
$\log(n/\text{cm}^{-3})$	2	4	2	3
A_V (mag)	5	3	3	4
$\log(\zeta/\text{s}^{-1})$	-13	-17	-14	-13
G_0	1	10	10	1
$\log(f_O)$	-3.6	-3.6	-3.6	-3.6
$\log(f_S)$	-7.1	-7.1	-7.1	-7.1
r_{max}	0.913	0.962	0.991	0.967
$\log(\mathcal{T}_r)$	2.747	5.495	4.929	4.202
$\mathcal{A}(\mathcal{T}_r)$	7.011	1.554	6.363	6.677

CHAPTER 4

SULFUR AND CHLORINE CHEMISTRY
IN THE VENUSIAN ATMOSPHERE

4.1 INTRODUCTION

While the Venusian atmosphere is primarily composed of carbon dioxide and molecular oxygen, clouds of sulfuric acid H_2SO_4 obscure the surface of Venus (Hansen and Hovenier, 1974; Gao et al., 2013), and many sulfur-containing compounds like sulfur dioxide SO_2 (Barker, 1979; Stewart et al., 1979), sulfur monoxide SO (Na et al., 1990), and carbonyl sulfide OCS (Bézard et al., 1990) as well as two chlorine-containing compounds hydrochloric acid HCl (Connes et al., 1967) and chlorine monoxide ClO (Sandor and Clancy, 2013) suggest a complex chemical composition exists in the Venusian atmosphere. Chemical models of the Venusian atmosphere include these molecules as well as other sulfur and chlorine-containing species that likely exist in the atmosphere (Krasnopolsky, 2007; Mills and Allen, 2007; Zhang et al., 2012). In this study, we consider reactions involving sulfur monochloride SCl , sulfur dichloride SCl_2 , and sulfanyl chloride HSCl that are likely to occur in the Venusian atmosphere (see Table 4.1) in an effort to complete existing chemical networks and to help guide observational efforts in the future by determining kinetic data that can help predict the chemical composition of undiscovered compounds in the Venusian atmosphere.

Potential energy surfaces for nine reactions involving the species listed above have been determined using the RCCSD(T) level of coupled cluster theory that correlates the Hartree-Fock wavefunction with single and double excitations as well as a perturbative approach for triple excitations (Purvis and Bartlett, 1982; Watts, Gauss, and Bartlett, 1993). The correlation consistent basis sets aug-cc-PVTZ for hydrogen and oxygen and aug-cc-PV(T+d)Z for sulfur and chlorine have been used to account for size variation, anisotropic variation, and diffusivity that occurs in molecular bonds (Dunning, 1989; Kendall, Dunning, and Harrison, 1992; Woon and Dunning, 1993; Dunning, Peterson, and Wilson, 2001). For all stationary points identified along the reaction coordinates, the harmonic frequencies, which are required to calculate the

transition-state-theory reaction rate coefficients, were calculated by displacement of the internal coordinates, while the dipole moments and dipole polarizabilities, which are parameters for the capture theory rate coefficients, were calculated using the finite field approach (Woon and Herbst, 2009; Müller and Woon, 2013). Additionally, the first ionization energies of the reactant species are parameters in the capture theory rate coefficient expression, so we implemented the reported values in the National Institute of Standards and Technology (NIST) at the RCCSD(T)/aug-cc-PVTZ/aug-cc-PV(T+d)Z levels of theory.

4.2 CHEMICAL DYNAMICS

4.2.1 Exothermic Reactions with a Barrier

For reactants A and B and transition state ‡, the transition state theory reaction rate coefficient (Woon and Herbst, 1996) is

$$k^{\text{TST}}(T) = \frac{k_B T}{h} \frac{Q^\ddagger}{Q_A Q_B} e^{-E_0/k_B T} \quad (4.1)$$

where E_0 is the difference between the reactant system and the transition state zero-point energies, and the molecular partition functions

$$Q = Q_{\text{rot}} Q_{\text{vib}} Q_{\text{trans}} Q_{\text{elec}} \quad (4.2)$$

for the reactants and transition state are the products of the contributions from the rotational, vibrational, translational, and electronic degrees of freedom.

We parameterize the partition functions by equivalent temperatures to observe by inspection the relative contributions of each rotational and vibrational mode to the molecular partition function over the temperature range $T = 10 - 800$ K, which includes the range of temperatures used in chemical models of the Venusian atmosphere. In terms of the rotational constants $\tilde{B} = B/hc$, where $B = h/8\pi^2 cI$ and I is the moment of inertia, the rotational temperature for a linear molecule becomes $\theta_r = hc\tilde{B}/k_B$. When energy levels are closely spaced, the partition function for linear molecules can be integrated

$$Q_{\text{rot}} = \frac{g_I^{\text{ns}}}{\sigma} \sum_J (2J+1) e^{-BJ(J+1)/k_B T} \approx \frac{g_I^{\text{ns}}}{\sigma} \frac{k_B T}{B} = \frac{g_I^{\text{ns}}}{\sigma} \frac{k_B T}{hc\tilde{B}} = \frac{T}{\theta_r} \quad (4.3)$$

and written in terms of the rotational temperature θ_r . The symmetry number σ accounts for indistinguishable configurations of identical nuclei (Fernández-Ramos et al., 2007) and is equal to 2 for homonuclear diatomic species such as Cl_2 , and 1 for heteronuclear diatomic species such as SCl and OH . In general, the symmetry number σ for a molecule in a given point group is equal to the ratio of the number of permutations of equivalent nuclei to the number of configurations unique under rotation. The rotational symmetry places constraints on the allowed symmetries of the total molec-

ular wavefunction, so the nuclear degeneracies and symmetries must be considered and appropriately coupled to rotational states such that the total molecular nuclear spin wavefunction exhibits appropriate behavior under the parity operator. For heteronuclear diatomic species, the nuclear spin degeneracy factor $g_I^{\text{ns}} = (2I_a + 1)(2I_b + 1)$ accounts for all possible nuclear spin states where I_a and I_b are the nuclear spins of the two nuclei and add vectorially. Because the nuclei are different, no nuclear exchange symmetry constraints are placed on the total molecular wave function. In homonuclear diatomic species, the identical nuclei do place nuclear exchange symmetry constraints on the allowed symmetry of the total molecular wavefunction (Hougen and Oka, 2005). For the system of identical $I = 3/2$ chlorine nuclei of Cl_2 , where both dominant isotopes ^{35}Cl and ^{37}Cl exhibit nuclear spin $I = 3/2$, in the totally symmetric ground electronic state $^1\Sigma_g^+$, there are a total of $(2I + 1)I = 6$ antisymmetric and $(2I + 1)(I + 1) = 10$ symmetric wavefunctions which must combine with rotational level wavefunctions that are even ($J = 0, 2, 4, \dots$) and odd ($J = 1, 3, 5, \dots$) so that the total molecular wavefunction remains antisymmetric under exchange of the fermion nuclei of the chlorine atoms. The sum over rotational levels in the previous equation then is expressed as two sums for J even ($g_{\text{odd}}^{\text{ns}} = 6$) and J odd ($g_{\text{even}}^{\text{ns}} = 10$), and because each rotational level of increasing energy alternates between even and odd symmetry, in the integral approximation of the rotational partition function each sum over even and odd rotational levels contributes equally resulting in a total nuclear spin degeneracy factor of $g_I^{\text{ns}} = 16$ for the Cl_2 molecule.

For nonlinear molecules the rotational partition function becomes

$$Q_{\text{rot}}^{\text{nonlin}} = \frac{g_I^{\text{ns}}}{\sigma} \left(\frac{k_B T}{hc} \right)^{3/2} \left(\frac{\pi}{\tilde{A}\tilde{B}\tilde{C}} \right)^{1/2} \quad (4.4)$$

in the integral approximation for rotational constants \tilde{A} , \tilde{B} , and \tilde{C} corresponding to the three calculated moments of inertia and symmetry number σ . Because the rotational temperatures are much lower ($\theta_r < 0.1$ K) than the temperature range ($T = 10\text{-}800$ K) for all reactant species involved in reactions exhibiting barriers in this study (see Table 4.2) the integration of the rotational partition function is justified. The rotational symmetry number σ for nonlinear molecules depends on the point group of each species; in this study, all nonlinear molecules lacking symmetry have rotational symmetry number $\sigma = 1$, and SCl_2 , which belongs to the C_{2v} point group has $\sigma = 2$. Additionally, each nonlinear species has a nuclear spin degeneracy $g_I^{\text{ns}} = \prod_j (2I_j + 1)$ contribution to the total molecular partition function. The SCl_2 molecule differs from the other nonlinear species in this study by having nuclear spin representation $\Gamma_{\text{ns}}^{\text{rot}} = 10A_1 \otimes 6B_2$ in the C_{2v} point group resulting in nuclear exchange symmetry considerations for the $g_I^{\text{ns}} = 16$ states. To determine the statistical weights of the nuclear spin states and how they couple to the rotational states, we follow the method outlined in Jensen and Bunker (1979). Table 4.3 contains possible

spin functions for two $I = 3/2$ particles and shows the reducible representation for the molecular symmetry group C_{2v} . The statistical weights for coupling to different internal molecular wave function symmetries are shown in Table 4.4, and the application of this method to rotational states of Cl_2 and SCl_2 are shown in Table 4.5. When coupled to states in an asymmetric top basis each state of increasing energy exhibits alternating symmetric/antisymmetric character, and in the high temperature limit where all states contribute equally, we use $g_I^{\text{ns}} = 16$ for the nuclear spin statistical weight to the total molecular partition function.

The partition function for each normal mode of vibration with frequency $\tilde{\nu}$ for the quantum mechanical harmonic oscillator can be written in terms of the vibration temperature $\theta_\nu = hc\tilde{\nu}/k_B$ and evaluated as a geometric series in vibrational quantum number v

$$q_\nu = \sum_v e^{-(hc\tilde{\nu}/k_B T)v} \quad (4.5)$$

$$= \frac{1}{1 - e^{-\theta_\nu/T}} \quad (4.6)$$

where the total vibrational contribution to the molecular partition function is the product from the normal modes i

$$Q_{\text{vib}} = \prod_i \frac{1}{1 - e^{-\theta_i/T}} \quad (4.7)$$

Many of the vibrational temperatures of the normal modes of reactants and transition states considered in this work fall within the temperature range of the calculations, suggesting the significance of their vibrational contribution to the molecular partition functions as the temperature increases from 10 to 800 K (see Table 4.6).

The molecular partition function ratio $Q = \frac{Q^\ddagger}{Q_A Q_B}$ can be factorized approximately as

$$Q = \prod_i \left(\frac{Q_i^\ddagger}{Q_{A_i} Q_{B_i}} \right) \quad (4.8)$$

$$= \prod_i Q_i \quad (4.9)$$

into the product of the ratios of the contributions from each type of separable motion - rotation (including nuclear spin), vibration, translation, and electronic - to observe the effect each type of contribution has on the total molecular partition function ratio. We assume all reactant and transition state molecules populate only the ground electronic states, and the electronic partition function ratio Q_{elec} reduces to the ratio of the

degeneracies of the lowest energy ground electronic states (see Table 4.7), excluding fine structure. Because atomic species have no rotational structure and therefore no rotational contribution to the molecular partition function, we account for the nuclear spin degeneracy of the atomic species g_I^{ns} as an explicit factor in the total atomic partition functions. The temperature dependences of the other partition function ratios Q_i depend on the number and type of degrees of freedom available to the reactants and transition state and contributions to the average energy of the system. The temperature-dependent reaction rate coefficient obeys Arrhenius-like behavior only when $Q \propto T^{-1}$, in which case the pre-exponential factor is $\frac{k_B T}{h} \frac{Q^\ddagger}{Q_A Q_B} \propto T^0$ and independent of temperature.

Finally, we apply a tunneling correction factor

$$\Gamma \approx 1 - \frac{(\hbar\nu_i)^2}{24(k_B T)^2} + \dots \quad (4.10)$$

in terms of the temperature T and imaginary harmonic frequency $\tilde{\nu}_i$ of the transition state structure to reaction rate coefficients for R1 - R5, those reactions with barriers along the minimum energy path (Woon and Herbst, 1996). The value of the correction factor is always greater than unity, competes with the Boltzmann factor of the transition state theory reaction rate coefficient, and can deviate far above unity at low temperatures (Bell, 1959).

4.2.2 Barrierless Reactions

In the absence of a barrier along the reaction coordinate, the collision between two neutral species occurs as a result of a general effective potential

$$V_{\text{eff}}(r) = \frac{L^2}{2\mu r^2} - \frac{C_n}{r^n} \quad (4.11)$$

where some long-range attraction competes with the orbital angular momentum associated with the reactant systems. By defining the total energy E to be greater than or equal to the maximum in the effective potential energy, the maximum impact parameter b_{max} and orbiting condition are found, and the geometric reaction cross-section

$$\sigma_r = \pi b_{\text{max}}^2 = \frac{\pi n}{n-2} \left[\frac{C(n-2)}{2E} \right]^{\frac{2}{n}} \quad (4.12)$$

is written in terms of b_{max} and describes the likelihood of a reaction event in terms of the power and coefficient of the attractive potential n and C , respectively, and the energy of the system E . Integrating the reaction cross section σ_r over a Maxwell-Boltzmann distribution of energies produces the temperature-dependent, thermally

averaged reaction rate coefficient

$$k_C(n, T) = \Gamma \left(\frac{2(n-1)}{n} \right) \sqrt{\frac{8k_B T}{\pi \mu}} (k_B T)^{-\frac{2}{n}} \left[\frac{C_n(n-2)}{2} \right]^{\frac{2}{n}} \quad (4.13)$$

in terms of the attractive potential $-\frac{C}{r^n}$.

At long range, the induced dipoles of two neutral species obey a Lennard-Jones attraction, which varies inversely as the sixth power ($n = 6$) of the distance between the reactant species. The coefficient of the Lennard-Jones attractive potential

$$C_{\text{LJ}} = \frac{3}{2} \frac{I_a I_b}{I_a + I_b} \alpha_a \alpha_b \quad (4.14)$$

depends on the ionization energies I and isotropic dipole polarizabilities α of the neutral reactants (see Table 4.7), while the induction term, which also varies inversely as the sixth power of the internuclear distance, has the coefficient

$$C_{\text{dip-ind}} = \mu_a^2 \alpha_b + \mu_b^2 \alpha_a \quad (4.15)$$

which depends on the permanent dipole moment μ and α values of the reactants (Clary et al., 1994; Herbst and Woon, 1997). The general temperature-dependent reaction rate coefficient for the potential consisting of these two interactions becomes

$$k_6(T) = \Gamma(5) \sqrt{\frac{8k_B T}{\pi \mu}} (k_B T)^{-1/3} (2C_6)^{1/3} \quad (4.16)$$

where $C_6 = C_{\text{LJ}} + C_{\text{dip-ind}}$ and $k_6(T) \propto T^{1/6} C_6^{1/3} \mu^{-1/2}$ (Georgievskii and Klippenstein, 2005). This calculation neglects the complex structure of the identified minimum energy paths as well as nuclear spin statistics and approximates the reaction rate coefficients as a function of temperature for reactions that proceed on every collision with maximum impact parameter determined by the orbiting condition. Other terms, namely the dipole-induced-dipole and dispersion terms in the potential yield reaction rate coefficients that are generally smaller than those governed by charge-dipole and dipole-dipole interactions (Georgievskii and Klippenstein, 2005), and the capture theory reaction rate coefficients for neutral-neutral species depends more strongly on the physical conditions of the reactant system than for ion-molecule reactions (Smith, Herbst, and Chang, 2004).

4.3 RESULTS AND DISCUSSION

4.3.1 Partition Function Contributions and Competition

Fig. 4.1 shows the temperature-dependent partition function ratios $Q_i(T)$ for each type of motion - translation, rotational, and vibrational - and for the total molecular

partition function for each of the reactions R1-R5, each of which exhibits a barrier along the minimum energy reaction coordinate. The panels in Figure 4.1 show the competing effects of each contribution to the total partition function ratio as a function of temperature as well as the temperature-dependent contributions of the exponential and tunneling correction factors to the overall reaction rate coefficients to illustrate which factors dominate at which temperatures. For reaction pathways with identical reactants (e.g. R3 and R4) or very similar reactants (e.g. R1, R2, and R2-D), the translational (R3/R4 and R1/R2/R2-D) and rotational (R3/R4 and R2/R2-D) partition function ratios can be so similar to one another that they essentially overlap at the scale plotted (see Fig. 4.1, top left and middle left). All translational partition function ratios exhibit the same temperature dependence, $Q_{\text{trans}} \propto T^{-3/2}$, reflecting the three translational degrees of freedom available to each reactant and transition state. The temperature dependence of the rotational contribution to the total partition function ratio depends on the geometry of the reactant species and transition states. The rotational partition function ratio for R1 between atomic S and homonuclear diatomic Cl_2 is $Q_{\text{rot}} \propto T^{1/2}$, while the rotational partition function ratio for R2 and R5 between heteronuclear diatomic molecules SH and SCl and homonuclear diatomic Cl_2 is $Q_{\text{rot}} \propto T^{-1/2}$. Because the sum of the rotational degrees of freedom of the reactant species H and SCl_2 are equal to the number of rotational degrees of freedom of the transition state in R3 and R4, the total rotational partition function ratios Q_{rot} remain constant as a function of temperature. All vibrational partition function ratios increase over the temperature range for R1-R5 (see Fig. 4.1, top right), and this trend appears as a result of the lower equivalent vibrational temperatures of the normal modes of the transition states compared with the equivalent vibrational temperatures of the normal modes of the reactant species. Minima in the total partition function ratios Q_{total} (see Fig 4.1. middle left) appear where the ratios of the transition state partition function and the product of the reactant partition functions to their respective first derivatives are equal and opposite. Reactions R3 and R4, which share common reactants ($\text{H} + \text{SCl}_2$), exhibit very similar translational and rotational partition function ratios (Fig. 4.1, top left and top center), but a greater difference between the vibrational partition function ratios for these reactions solely accounts for the larger difference in the total partition function ratios for these reactions. Fig. 4.1 also shows the logarithm of the tunneling correction factor (middle right) and temperature-dependent reaction rate coefficients (bottom left) for reactions R1-R5.

4.3.2 Temperature-dependent rate coefficients for reactions with barriers

For reactions with barriers (R1-R5), Fig. 4.2 shows the calculated temperature-dependent transition state theory reaction rate coefficients, $k_{\text{TST}}(T)$, as dotted lines with color that corresponds to the reaction number.

Chemical kinetic models of the Venusian atmosphere utilize the Arrhenius-Kooij

formula

$$k(T) = \alpha \left(\frac{T}{300 \text{ K}} \right)^\beta e^{-\gamma/T} \quad (4.17)$$

for tabulating reaction rate coefficient data, so we fit the Arrhenius-Kooij parameters α (not to be confused with the dipole polarizability) and β to our calculations so these reactions can be included in future kinetic models of the Venusian atmosphere. We determine the parameters α and β by minimizing the sum of the squares of the residuals between the calculated $k_{\text{TST}}(T)$ pre-exponential factors and the Arrhenius-Kooij reaction rate coefficient pre-exponential factors $\ln(A) = \ln(\alpha) + \beta \ln(T/300\text{K})$, while γ has been determined from the electronic structure calculations and is excluded from the least-squares fitting procedure. Table 4.1 contains the Arrhenius-Kooij parameters α , β , and γ as well as the coefficient of determination R2 for each reaction, and these optimized $k_{\text{AK}}(T)$ appear as solid lines in Fig. 4.2.

Because the partition functions and partition function ratios do not exhibit a simple power-law dependence on the temperature due to the vibrational contribution at low temperatures $T < \theta_\nu$, the pre-exponential factors of R1-R5 are not well fit by the power law expression of the Arrhenius-Kooij formula over the entire temperature range (see Table 4.1). To find better fit representations for atmospheric kinetic models, we fit Arrhenius-Kooij parameters α and β to the calculated reaction rate coefficients $k_{\text{TST}}(T)$ piecewise (piecewise Arrhenius-Kooij, or PAK in our notation) over three reduced temperature ranges, low ($T < 50$ K, type 1), medium ($50 \text{ K} < T < 150$ K, type 2), and high ($T > 150$ K, type 3), and record them in Table 4.1. Substantial increases in the coefficients of determination R2 emerge for $k_{\text{PAK}}(T)$ when compared with those R2 for $k_{\text{AK}}(T)$, indicating better fits over the piecewise temperature ranges, the boundaries of which appear in black in Fig. 4.2. These boundaries are motivated by the temperature ranges of models of the lower and middle atmosphere of Venus, and in Fig. 4.2, these modeled temperature ranges appear as different background colors (see Fig. 4.2 caption for references).

Reaction R1 between atomic sulfur and diatomic chlorine, $\text{S} + \text{Cl}_2 \rightarrow \text{Cl} + \text{SCl}$, is represented in several models of the middle and lower atmosphere of Venus (Mills and Allen, 2007; Krasnopolsky, 2007, 2012; Zhang et al., 2012) with an Arrhenius equation $k(T) = 2.8 \times 10^{-11} e^{-290/T} \text{ cm}^3 \text{ s}^{-1}$. Our calculated rate coefficients $k_{\text{TST}}(T)$ for R1 are several orders of magnitude smaller than the existing Arrhenius values for all temperatures and exhibit non-Arrhenius behavior as a result of the lack of a simple power-law temperature dependence of the vibrational partition functions. The large discrepancy between the older value and ours is due to large differences in both the pre-exponential factor and the exponent. Our calculated reaction rate coefficients for the reaction between SH and Cl_2 , R2, are several orders of magnitude lower than the literature value $k(T) = 1.4 \times 10^{-11} e^{-690/T} \text{ cm}^3 \text{ s}^{-1}$ (Sander et al., 2006; Krasnopolsky, 2012), which also exhibits slightly less variation over middle

atmosphere temperatures, for all temperatures in our range. Once again, the large discrepancy between the older value and ours is due both to differences in the pre-exponential and exponential factors. The calculated reaction rate coefficients for R3 and R4, reactions between H and SCl₂, are roughly within an order of magnitude of each other, $\log(k_{R3}) \sim \log(k_{R4})$, at higher temperatures $T > 300$ K but quickly diminish and diverge as the temperature falls below 300 K. Because reactions R3 and R4 are absent in existing chemical kinetic models of the lower and middle atmosphere of Venus, our calculated values provide new constraints on the coupled kinetics of sulfur and chlorine chemistry in atmospheric models. At temperatures below 800 K, our calculated temperature-dependent reaction rate coefficients for R5, the reaction between SCl and Cl₂, fall several orders of magnitude below the reported temperature-independent value $k = 7 \times 10^{-14} \text{ cm}^3 \text{ s}^{-1}$ (Murrells, 1987), which has been incorporated in chemical models of the middle atmosphere ($\sim 50 - 112$ km) of Venus (Mills and Allen, 2007; Krasnopolsky, 2012), and this difference could impact existing chemical models of the middle atmosphere due to the decreased rate coefficient values at the middle atmosphere temperatures ($T \sim 150 - 375$ K).

4.3.3 Temperature-dependent rate coefficients for reactions without barriers

Fig. 4.3 shows the temperature-dependent capture theory reaction rate coefficients $k_C(T)$ for the reactions without barriers R6-R9 in dot-dashed line style. All rate coefficients vary with a power law temperature dependence $k(T) \propto T^{1/6}$ as a result of the Lennard-Jones attraction and induction terms included in the effective potential and therefore do not warrant a least-squares method to fit the Arrhenius-Kooij formula for implementation into existing chemical networks for kinetic models of the Venusian atmosphere, in contrast to the TST calculations. Because these reaction rate coefficients depend only on the reactant electronic structures, and R7 exhibit identical temperature-dependent reaction rate coefficients $k_C(T)$ as they increase slightly over the temperature range $T = 10-800$ K. The reactions R6 and R7 do not appear in current chemical models of the lower and middle Venusian atmosphere, and our calculations provide data for the rate coefficients of the reactions $\text{OH} + \text{HSCl} \rightarrow \text{SCl} + \text{H}_2\text{O}$ (R6) and $\text{OH} + \text{HSCl} \rightarrow \text{Cl} + \text{HSOH}$ (R7) that can be included in existing chemical networks. Some chemical models of the lower and middle atmosphere of Venus (Mills and Allen, 2007; Zhang et al., 2012) include reaction R8, $\text{S} + \text{SCl} \rightarrow \text{Cl} + \text{S}_2$, R8, in their chemical network with a constant rate coefficient $k(295 \text{ K}) = 1 \times 10^{-11} \text{ cm}^3 \text{ s}^{-1}$ (see Fig. 4.3 black “+”, Murrells (1987)) and $k(295 \text{ K}) = 1 \times 10^{-12} \text{ cm}^3 \text{ s}^{-1}$ used in an earlier model (see Fig. 4.3 black “×”, Krasnopolsky (2007)), slightly lower than our calculated temperature dependent reaction rate coefficients. The reaction between two sulfur monochloride molecules, $\text{SCl} + \text{SCl} \rightarrow \text{Cl} + \text{SSCl}$ (R9), is present in chemical networks used to model the middle atmosphere of Venus (Mills and Allen, 2007; Zhang et al., 2012) with a constant rate coefficient $k(295 \text{ K}) = 5.4 \times 10^{-11} \text{ cm}^3 \text{ s}^{-1}$ (see Fig. 4.3 violet “+”, Murrells (1987)),

and this value is slightly greater than our calculated values. Our calculated reaction rate coefficients, however, are temperature-dependent, albeit weakly, and can be used in chemical networks to model the chemistry of the Venusian atmosphere over the appropriate temperature ranges.

4.4 CONCLUSIONS

Using the updated structural parameters of reactant species and identified transition states, we have calculated the temperature-dependent reaction rate coefficients for a set of nine reactions of possible importance in kinetic models of the atmosphere of Venus. For reactions R1-R5 with identified barriers along the minimum energy path, we calculated the transition state theory reaction rate coefficients $k_{\text{TST}}(T)$, corrected for tunneling, and nuclear spin statistics when calculating the molecular partition functions when appropriate. For reactions without barriers, R6-R9, we have calculated the reaction rate coefficients $k_{\text{C}}(T)$ using a capture model and an effective potential including terms for orbital angular momentum, a Lennard-Jones attraction, and dipole-induced dispersion. To provide data that can be integrated into existing chemical networks and kinetic models of various layers of the atmosphere of Venus, we fit Arrhenius-Kooij parameters to reaction rate coefficients $k_{\text{PAK}}(T)$ for reactions with barriers over three temperature ranges characteristic of a low temperature limit and the middle and lower Venusian atmospheres. Our calculated reaction rate coefficients are generally lower than adopted values in existing models of the Venusian atmosphere. Expanding the kinetic model to consider Venus-like pressures and possible collisional stabilization will, in the future, provide stronger constraints on the reaction rate coefficients for the nine systems in this study. Additionally, our study can supplement chemical networks with reactions involving deuterated species, which can guide observations of these isotopologues in future molecular line surveys. The Arrhenius-Kooij parameters we report for each of the reactions reflect the updated geometries and new transition state energies identified in this study and can be readily incorporated into existing chemical networks and compared with future experimental and theoretical efforts over a broad temperature range.

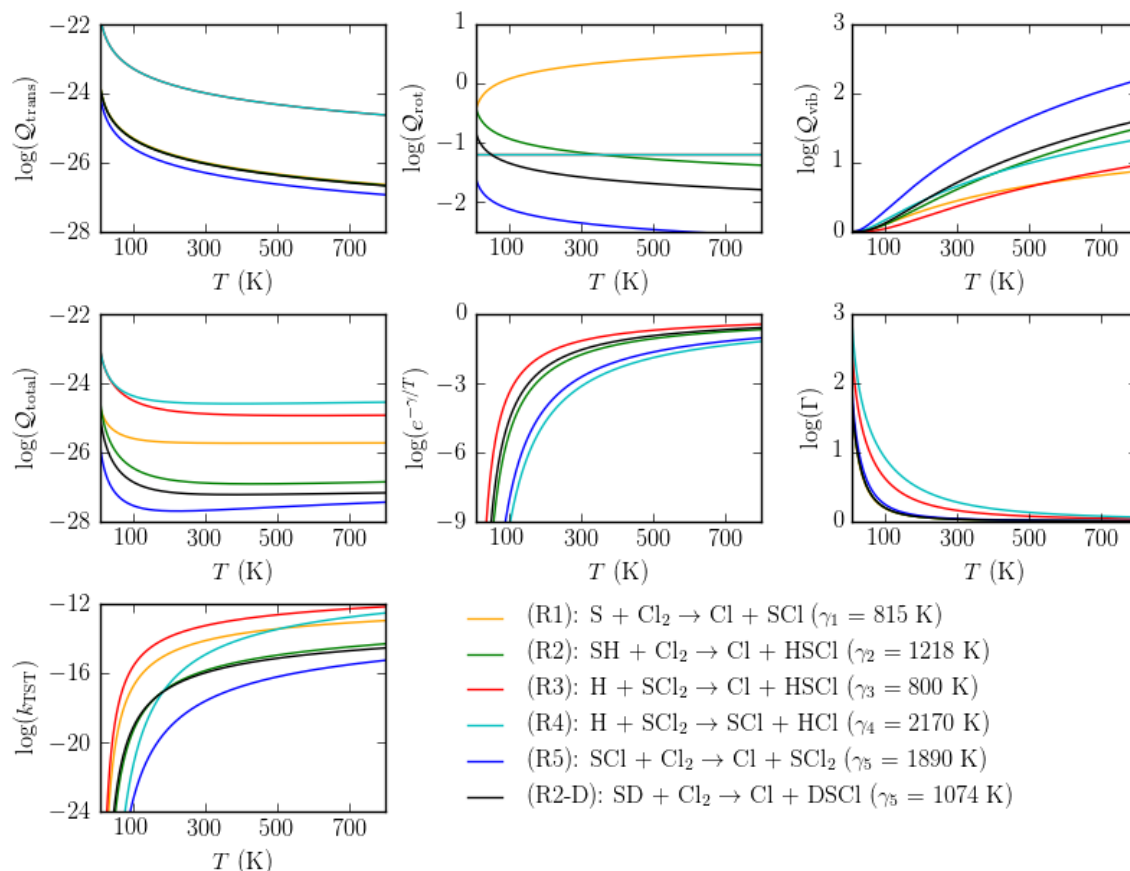


Figure 4.1: Ratios of the logarithms of the temperature-dependent partition function contributions for various degrees of freedom: translational (top left), rotational (top center), vibrational (top right), the total molecular partition (middle left), the Boltzmann factor (middle center) the tunneling correction (middle right), and the transition-state-theory reaction rate coefficients $k_{\text{TST}}(T)$ (bottom left) for reactions R1-R5 where color corresponds to reaction number.

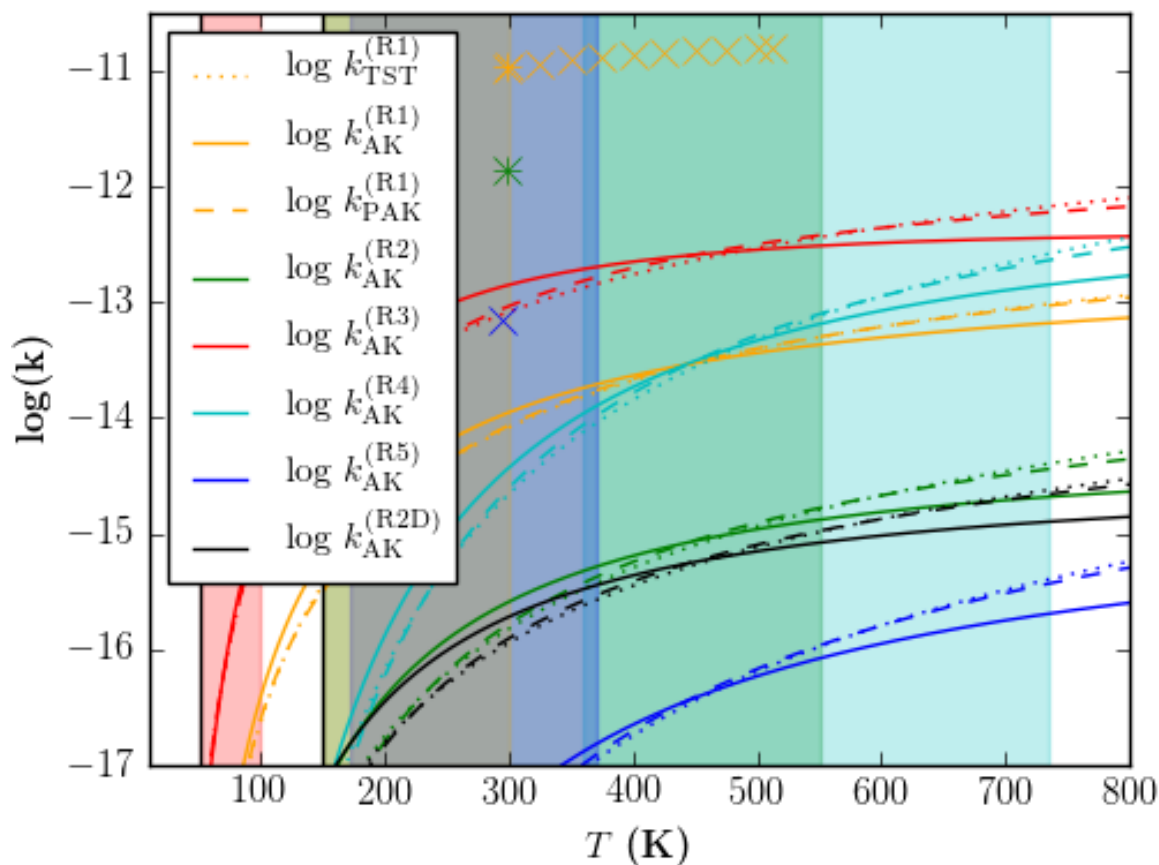


Figure 4.2: Temperature-dependent reaction rate coefficients $k(T)$ for reactions R1 - R5. Colors correspond to reaction number, while line styles correspond to formula fit by least-squares method: transition state theory calculations (TST, dotted), Arrhenius-Kooij fits to the TST calculations (AK, solid), and modified piecewise Arrhenius-Kooij fits over the temperature range fragments (PAK, dashed). Points marked with “ \times ” and “ $+$ ” refer to values determined from previous studies (see text). Solid black vertical lines appear at the temperature range fragment boundaries for the PAK fits, and background color corresponds to the temperature and altitude ranges of existing atmospheric kinetic models of the Venusian atmosphere: red, 50-100 K (112-58 km); goldenrod, 150-300 K (112-58 km); green, 150-550 K (130-80 km); blue, 172.2-370.2 K (112-47 km); and cyan, 360-735 K (47-0 km) (see text for references).

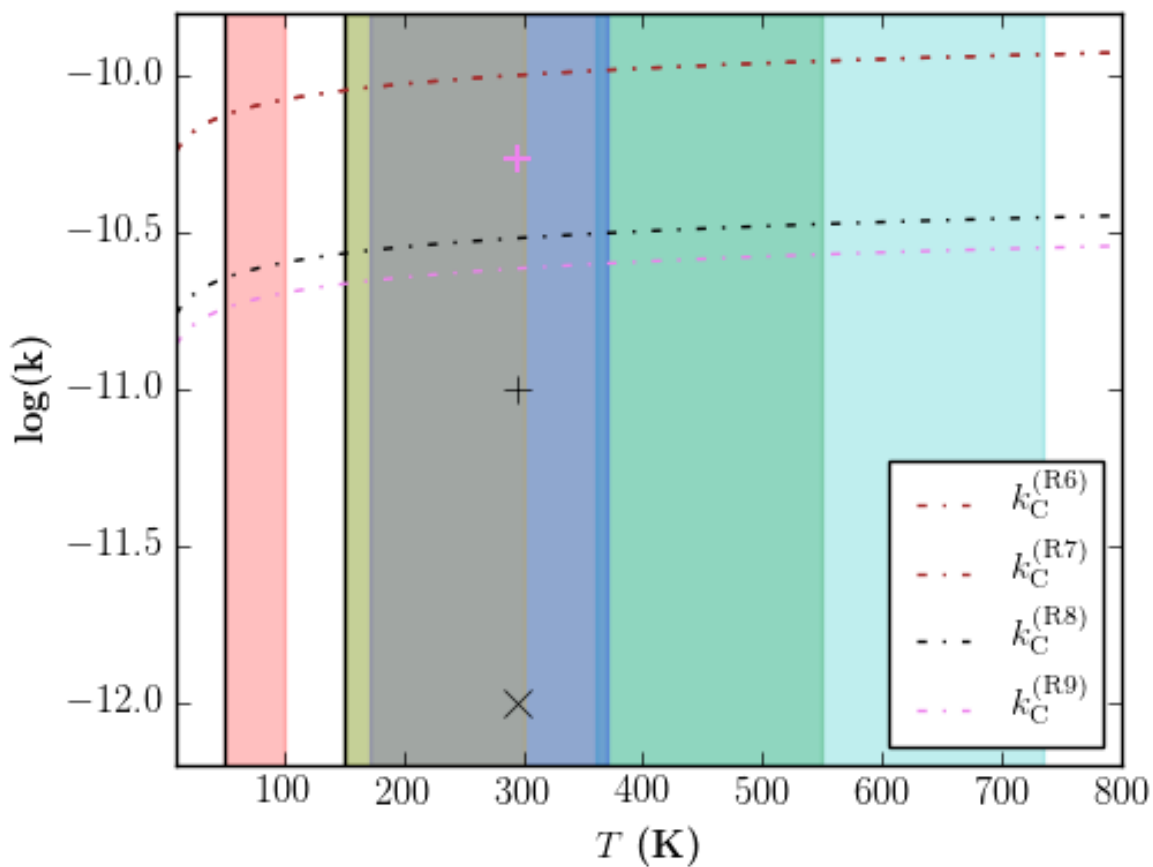


Figure 4.3: Temperature-dependent capture theory reaction rate coefficients $k(T)$ for reactions R6-R9. Colors correspond to reaction number. Points marked with “ \times ” and “ $+$ ” refer to literature values (see text); see Fig. 4.2 for key to background colors.

Table 4.1: Arrhenius-Kooij Parameters

ID	Reaction	Type	α (cm ³ s ⁻¹)	β	γ (K)	R ²
(R1)	S + Cl ₂ → Cl + SCl	AK	1.691e-13	1.861e-01	8.150e+02	0.110
		1	5.784e-15	-1.715e+00	8.150e+02	0.997
		2	5.740e-14	-3.921e-01	8.150e+02	0.800
		3	1.305e-13	8.646e-01	8.150e+02	1.000
(R2)	SH + Cl ₂ → Cl + HSCl	AK	1.497e-14	-3.549e-01	1.218e+03	0.169
		1	2.714e-16	-2.745e+00	1.218e+03	0.999
		2	2.877e-15	-1.365e+00	1.218e+03	0.971
		3	9.657e-15	7.521e-01	1.218e+03	1.000
(R2D)	SD + Cl ₂ → Cl + DSCl	AK	6.873e-15	-2.556e-01	1.074e+03	0.094
		1	1.028e-16	-2.740e+00	1.074e+03	0.999
		2	1.255e-15	-1.274e+00	1.074e+03	0.961
		3	4.474e-15	8.391e-01	1.074e+03	1.000
(R3)	H + SCl ₂ → Cl + HSCl	AK	2.029e-12	-7.195e-01	7.999e+02	0.520
		1	1.498e-13	-2.421e+00	7.999e+02	1.000
		2	4.376e-13	-1.767e+00	7.999e+02	0.991
		3	1.330e-12	3.200e-01	7.999e+02	0.999
(R4)	H + SCl ₂ → SCl + HCl	AK	5.222e-12	-7.271e-01	2.173e+03	0.546
		1	3.636e-13	-2.424e+00	2.173e+03	1.000
		2	1.294e-12	-1.670e+00	2.173e+03	0.992
		3	3.484e-12	2.680e-01	2.173e+03	0.999
(R5)	SCl + Cl ₂ → Cl + SCl ₂	AK	2.482e-15	8.109e-02	1.892e+03	0.009
		1	2.121e-17	-2.707e+00	1.892e+03	0.998
		2	3.923e-16	-1.008e+00	1.892e+03	0.926
		3	1.561e-15	1.267e+00	1.892e+03	1.000
(R6)	OH + HSCl → SCl + H ₂ O	C	3.880e-11	1.667e-01	–	–
(R7)	OH + HSCl → Cl + HSOH	C	3.880e-11	1.667e-01	–	–
(R8)	S + SCl → Cl + S ₂	C	1.173e-11	1.667e-01	–	–
(R9)	SCl + SCl → Cl + SScI	C	9.384e-12	1.667e-01	–	–

NOTE — Fit type C corresponds to the capture theory formula $k_C = \alpha(T/300 \text{ K})^\beta$ where $\beta = 1/6$ for neutral-neutral reactions, fit type AK corresponds to fits of the Arrhenius-Kooij pre-exponential factor $\log(A) = \log(\alpha) + \beta \log(T/300 \text{ K})$ for all temperatures ($10 \leq T \leq 800 \text{ K}$), while fit types 1, 2, and 3 correspond to fits of the piecewise Arrhenius-Kooij pre-exponential factor $\log(A_{\text{PAK}}) = \log(\alpha) + \beta \log(T/300 \text{ K})$ for low ($T < 50 \text{ K}$), medium ($50 \leq T \leq 150 \text{ K}$), and high ($T > 150 \text{ K}$) temperature ranges.

Table 4.2: Rotational
Parameters^a

Molecule	\tilde{B} (cm ⁻¹)	θ_r (K)
Cl ₂	0.23895	0.3
SH	9.5701	13.8
SCl	0.25366	0.4
SCl ₂	0.07988	0.1
	0.09597	0.1
	0.47648	0.7
TS1	0.05071	0.1
	0.05132	0.1
	4.2551	6.1
TS2	0.05049	0.1
	0.05123	0.1
	2.0531	3.0
TS2-D	0.04966	0.07
	0.05022	0.07
	1.68908	2.4
TS3	0.077	0.1
	0.09491	0.1
	0.39417	0.6
TS4	0.07342	0.1
	0.08844	0.1
	0.43083	0.6
TS5	0.02711	0.04
	0.0296	0.04

Table 4.3: Reducible Representation of Nuclear Spin States of Molecules with Two $I = 3/2$ Atoms

				E	(12)	E^*	(12)*
$(m_I = 3):$	$\gamma\gamma = \Phi_{\text{ns}}^{(1)}$			1	1	1	1
$(m_I = 2):$	$\gamma\alpha = \Phi_{\text{ns}}^{(2)}$	$\alpha\gamma = \Phi_{\text{ns}}^{(3)}$		2	0	2	0
$(m_I = 1):$	$\gamma\beta = \Phi_{\text{ns}}^{(4)}$	$\beta\gamma = \Phi_{\text{ns}}^{(5)}$	$\alpha\alpha = \Phi_{\text{ns}}^{(6)}$	3	1	3	1
$(m_I = 0):$	$\gamma\delta = \Phi_{\text{ns}}^{(7)}$	$\delta\gamma = \Phi_{\text{ns}}^{(8)}$	$\alpha\beta = \Phi_{\text{ns}}^{(9)}$	4	0	4	0
$(m_I = -1):$	$\delta\alpha = \Phi_{\text{ns}}^{(11)}$	$\alpha\delta = \Phi_{\text{ns}}^{(12)}$	$\beta\beta = \Phi_{\text{ns}}^{(13)}$	3	1	3	1
$(m_I = -2):$	$\delta\beta = \Phi_{\text{ns}}^{(14)}$	$\beta\delta = \Phi_{\text{ns}}^{(15)}$	$\beta\alpha = \Phi_{\text{ns}}^{(10)}$	2	0	2	0
$(m_I = -3):$	$\delta\delta = \Phi_{\text{ns}}^{(16)}$			1	1	1	1
$\Gamma_{\text{nspin}}^{\text{red}} =$				16	4	16	4

Table 4.4: Nuclear Spin State Degeneracies and Symmetry Considerations for Molecules with Two $I = 3/2$ Atoms

Γ_{rve}	Γ_{nspin}	Γ_{int}	g_n
A_1	$6B_2$	B_2	6
A_2	$6B_2$	B_1	6
B_1	$10A_1$	B_1	10
B_2	$10A_1$	B_2	10

Table 4.5: Degeneracies for Possible Nuclear Spin States of Even and Odd Symmetry for Molecules with Two $I = 3/2$ Chlorine Atoms

Molecule	ψ_{elec}	ψ_{rot}	Γ_{nspin}	g_n
Cl_2	${}^1\Sigma_g^+$	$J = \text{even}$	$6B_2$	6
		$J = \text{odd}$	$10A_1$	10
SCl_2	A_1	$J = \text{even}$	$6B_2$	6
		$J = \text{odd}$	$10A_1$	10

Table 4.6: Vibrational
Parameters^a

Molecule	$\tilde{\nu}$ (cm ⁻¹)	θ_v (K)
Cl ₂	546	786
SH	2700	3886
SCl	567	816
SCl ₂	205	295
	522	751
	523	753
TS1	111	160
	347	500
	241 [‡]	347
TS2	125	180
	233	335
	349	502
	549	790
	2701	3888
	251 [‡]	361
TS2-D	124	178
	183	263
	347	499
	399	574
	1940	2792
	251 [‡]	361
TS3	192	276
	199	286
	283	407
	498	717
	521	750
	581 [‡]	836
TS4	92	132
	171	246
	254	366
	493	710
	530	763
	911 [‡]	1311
TS5	66	95
	140	202
	247	356
	341	491
	553	796
	294 [‡]	423

Table 4.7: Ground State Electronic Data

Molecule	Term	g_e	g_n	I (eV) ^a	α (Å ³) ^b	μ (D)
H	² S	2	2	13.60	0.279	–
S	³ P	9	1	10.36	2.144	–
OH	² Π	4	2	13.02	1.075	1.639
SH	² Π	4	2	10.42	3.264	0.749
SCl	² Π	4	4	9.52	5.253	0.097
HSCl	<i>A'</i>	1	8	9.83 ^b	5.509	1.155
SCl ₂	<i>A</i> ₁	1	16	9.47 ^b	7.642	0.401
Cl ₂	¹ Σ _g ⁺	1	16	11.48	4.536	–
TS1	³ <i>A''</i>	3	16	–	–	–
TS2	² <i>A</i>	2	32	–	–	–
TS3	² <i>A</i>	2	32	–	–	–
TS4	² <i>A</i>	2	32	–	–	–
TS5	² <i>A</i>	2	64	–	–	–

NOTE — ^a From Lias 2016, NIST Standard Reference Database 69; ^bFor RCCSD(T)/aug-cc-PVTZ method/basis set from this work

CHAPTER 5

CONCLUSIONS AND FUTURE WORK

5.1 MAJOR CONCLUSIONS

Grid modeling techniques reveal sensitivities in chemical kinetic models and will serve as a paradigm for interferometric observations as images of molecular line emission and absorption become more widely available. In the previous chapters, the chemical composition of the dark cloud conditions of TMC-1 as well as the diffuse and translucent cloud conditions of the absorption components observed along the line of sight to Sgr B2 are shown to be well reproduced by homogeneous chemical kinetic models. Some major results of our studies include:

- Type I grid models (variation of parameters) break degeneracies in the solution space of the rate law equations when modeling observed chemical compositions with chemical kinetic models
- Type I grid models identify regions in the free-parameter space where bistabilities on the rate-law solutions may exist by revealing values of free parameters between which large difference in the solution to the rate law equations emerge and explicitly separate the effects of varying each free parameter on the time-dependent chemical evolution
- The root-mean-square log difference \mathcal{A} between modeled and observed abundances is a good measure of model validity as it quantifies absolute agreement
- The mean deviation σ provides a method of determining agreement with weighted contributions from each molecule in a group, and the fit character reflects these weights
- The correlation coefficient r in combination with \mathcal{A} can reveal systematic errors in a set of abundances when good correlation exists with poor absolute agreement, but alone large r is not a strong criterion for good agreement between observed abundances and those produced from kinetic models

- The density and cosmic ray ionization rate change the chemical timescale for most species considered in the previous chapters
- Strong radiation fields emulated by low visual extinctions and large radiation field strength factors inhibit the production of species sensitive to photo reactions to the extent that homogeneous conditions cannot reproduce observed abundances
- Changing the fractional elemental abundance of sulfur for sulfur-containing species can mitigate detrimental effects of photochemistry, though overproduction can also occur as a result of enhanced sulfur
- Large barriers along the reaction coordinate result in slow temperature-dependent reaction rate coefficients without any additional mitigating factors

5.2 DATA REPOSITORIES

Grid models produce large sets of abundance data for all species represented in the chemical network, and these repositories naturally benchmark the network and the model to promote transparency and reproducibility within the field of theoretical astrochemistry. Furthermore, the robust repositories provide extensive data that can fuel future studies of the chemistry of compounds in similar conditions though not included in the focuses of the studies contained in this work. Model data and visualization tools can be found at <https://github.com/dmaff17>.

5.3 FUTURE ENDEAVORS

Contemporary models of the 2D physical structure of PPDs fit parametric equations to measured mm and sub-mm continuum images of molecular lines and the thermal dust continuum to constrain the temperature and density distributions of the gas and dust as well as the relative radiation field strength. Using the reported best fit parameters (disk mass M_d , characteristic surface density Σ_c , critical radius R_c , scale height H , flaring parameter ψ , gas surface density power γ , relative mm-grain scale height χ , and the mass fraction of large grains f) for a survey of 13 PPDs (Andrews et al., 2010; Öberg et al., 2015; Cleeves et al., 2016) grids of the physical structures $p(r, z) = [T_{\text{gas}}(r, z), T_{\text{grain}}(r, z), n_{\text{gas}}(r, z), \rho_s(r, z), \rho_l(r, z), A_V(r, z)]$ of each PPD have been generated that incorporate both small ρ_s and large ρ_l grain distributions for input into our chemical model and obtain the 2D time-dependent chemical structures using Type II grid models. The abundance profile of CO has been reproduced using this type of 2D kinetic model (Cleeves et al., 2016) but for larger species like CH₃CN, the formation and destruction pathways are often understudied making it difficult for the incomplete chemical networks and kinetic models to reproduce the observed abundance ratios (Öberg et al., 2015). Figure 5.1 shows a subspace of the parametric physical structure of MWC 480 (Öberg et al., 2015) exemplifying

the utility of Type II grid models and the solution $X_{\text{CH}_3\text{CN}}(t)/X_{\text{HCN}}(t) > 0.01$, which appears in my disk model in the warm molecular zone on the surface of the disk around $t = 0.1$ Myr. These models will be further studied in the future to determine the effect of disk structure on the chemical evolution as well as to help guide future investigations into molecular line surveys for the disks contained in this sample. Figures 5.2 - 5.7 show the physical structure of the disks contained in the sample. The parameters represented in the chemical model (temperature, particle density, and visual extinction) have been used to simulate the chemical evolution of the disks using Type II grid models, and the preliminary models will serve as a baseline for models that incorporate more detailed physical structure in the future.

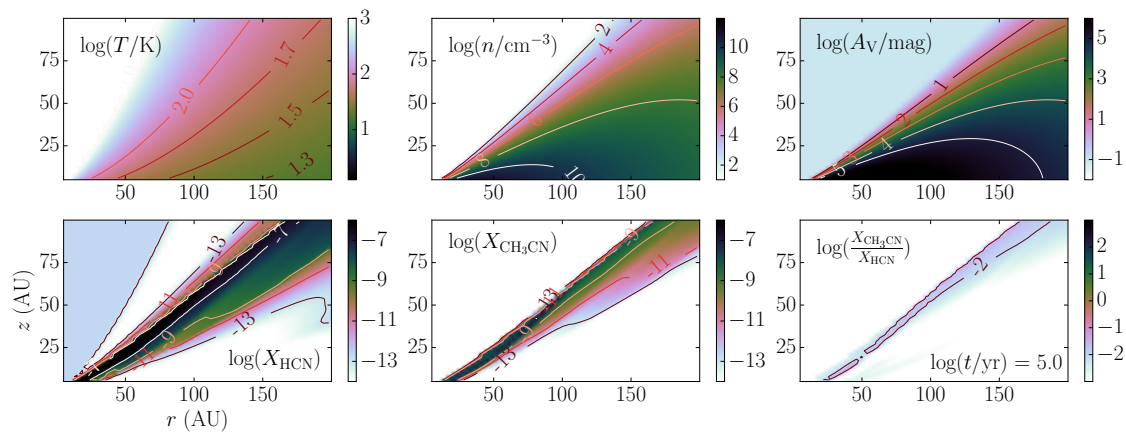


Figure 5.1: Model of disk around MWC 480 exemplifying Type II grid models.

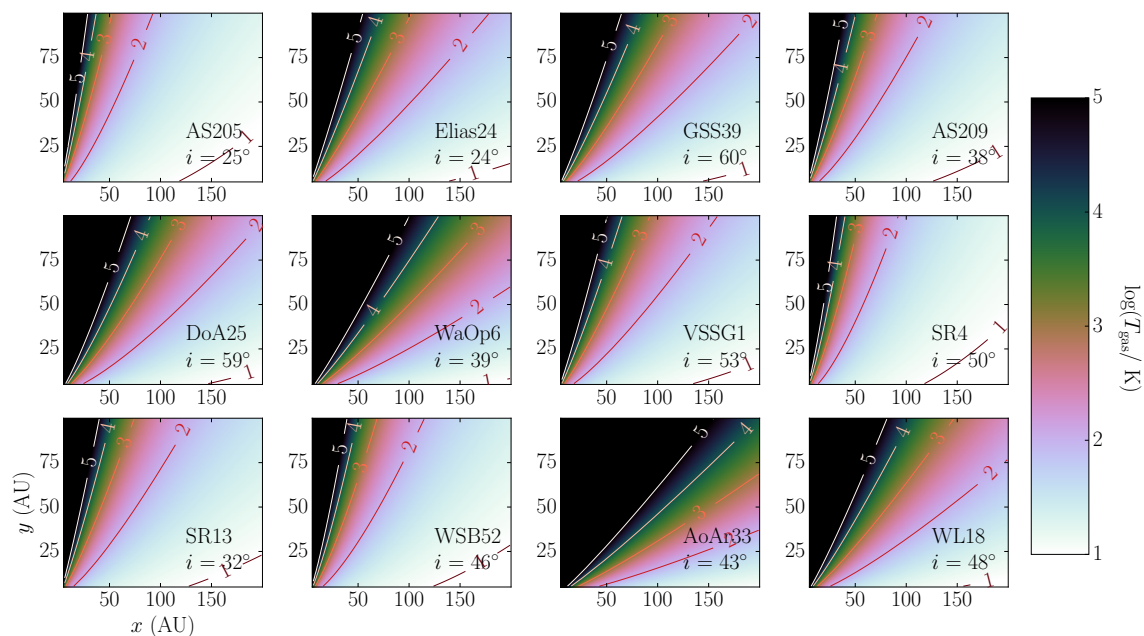


Figure 5.2: Gas temperatures for disks in Andrews et al. (2010) survey.

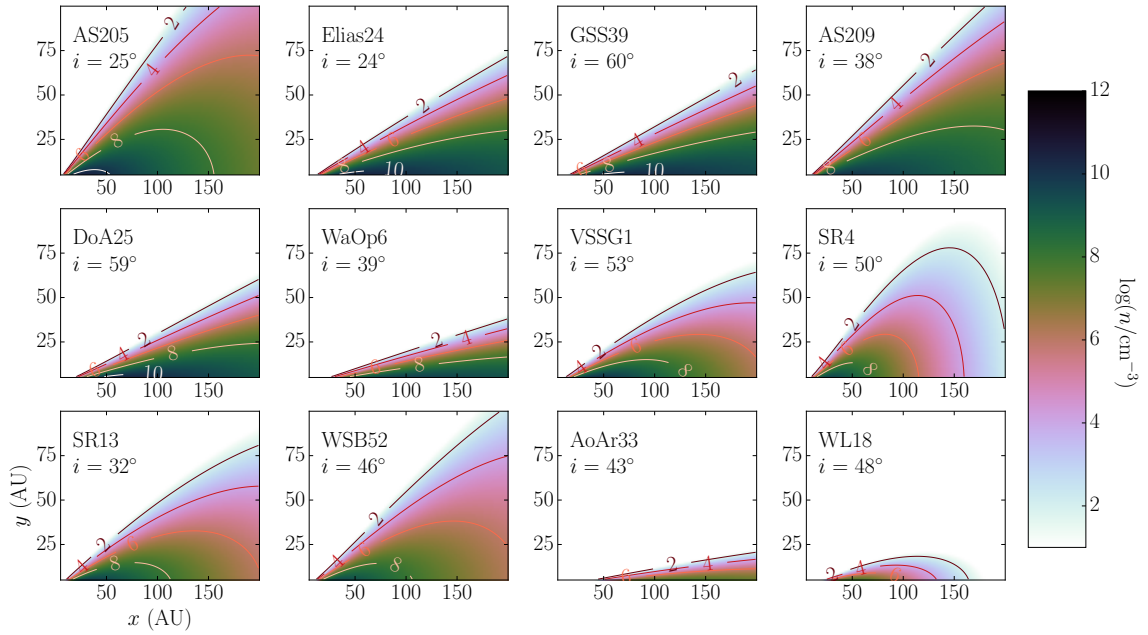


Figure 5.3: Particle densities for disks in Andrews et al. (2010) survey.

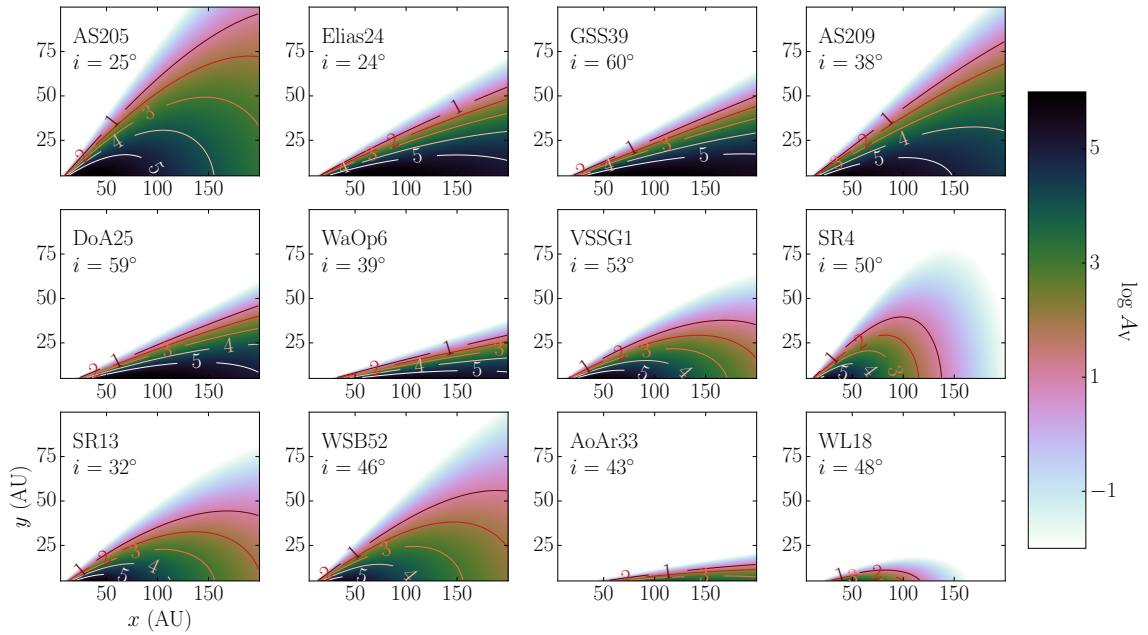


Figure 5.4: Visual extinctions for disks in Andrews et al. (2010) survey.

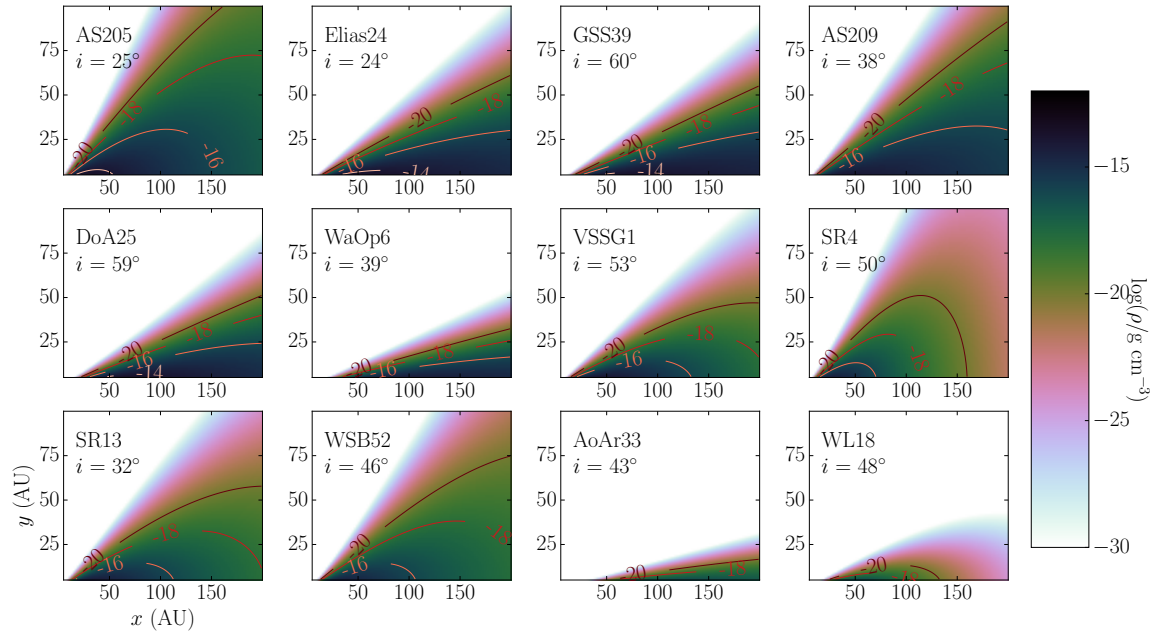


Figure 5.5: Mass densities for disks in Andrews et al. (2010) survey.

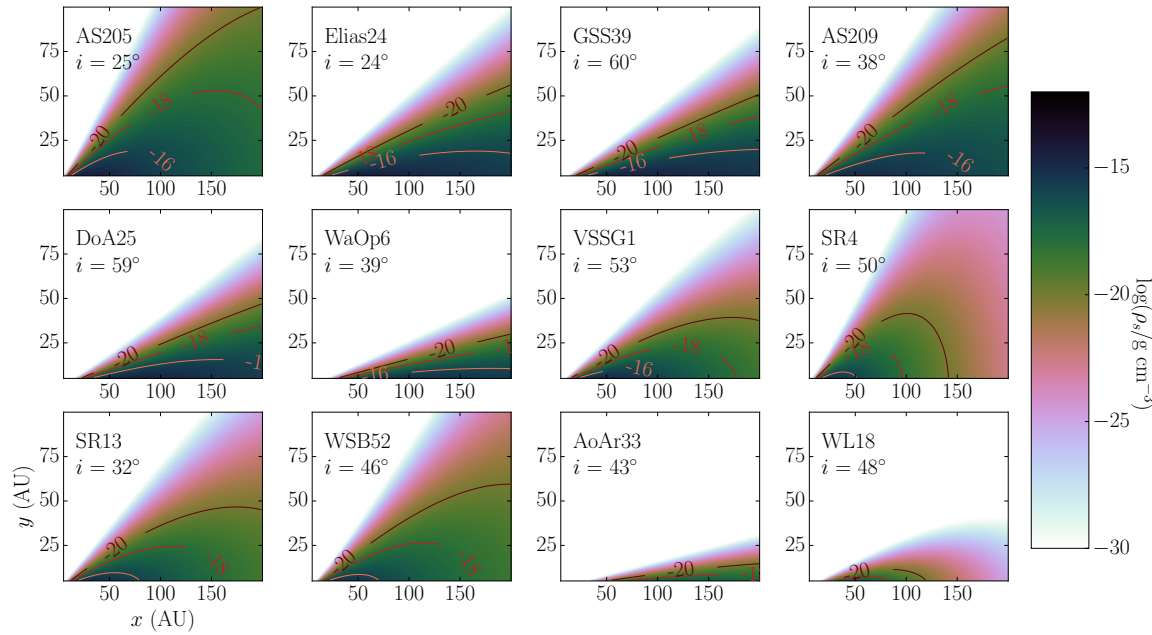


Figure 5.6: Small dust grain densities for disks in Andrews et al. (2010) survey.

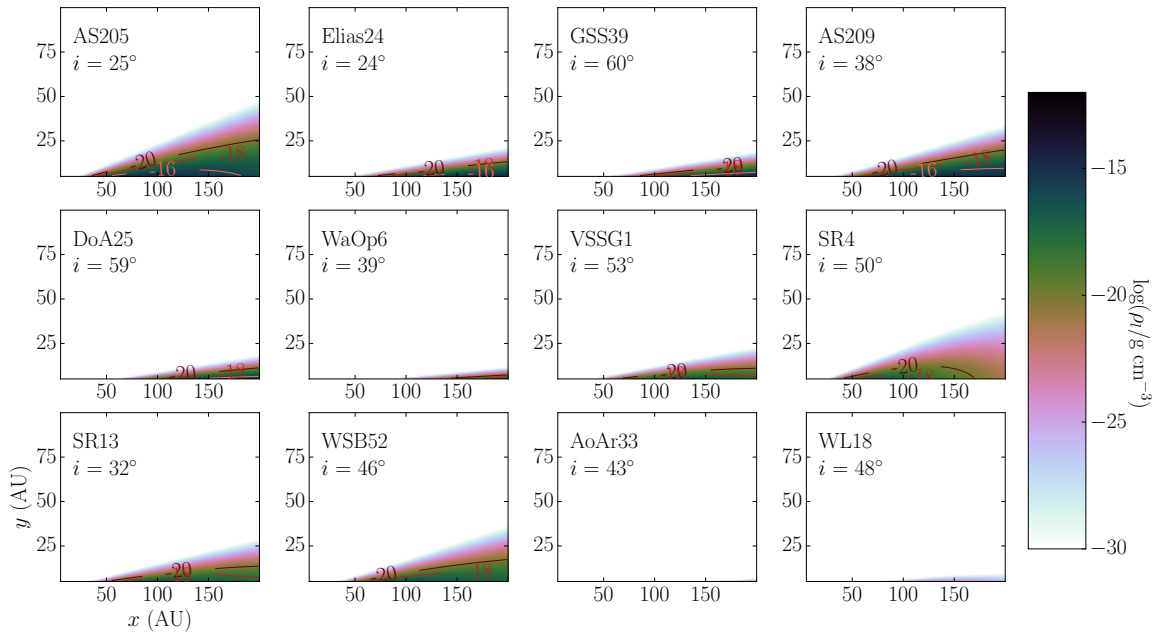


Figure 5.7: Large dust grain densities for disks in Andrews et al. (2010) survey.

REFERENCES

- Agundez, M. and Wakelam V. 2013, *ChRv*, 113, 8710
- Andrews, S., M., Wilner, D., H., Hughes, A., M., et al. 2010, *The Astrophysical Journal*, 723, 1241
- Barker, E., S. 1979, *Geophys. Res. Lett.*, 6, 117
- Barone, V., Latouche, C., Skouteris, D., et al. 2015, *Monthly Notices of the Royal Astronomical Society*, 453, L31
- Bell, R., P. 1959, *T. Faraday Soc.*, 55, 1
- Belloche, A., Müller, H. S., P., Menten, K., M., et al. 2013, *Astronomy and Astrophysics*, 559, 187
- Belloche, A., Müller, H. S., P., Menten, K., M., et al. 2014, *Astronomy and Astrophysics*, 561, 1
- Belloche, A., Müller, H. S., P., Garrod, R., T., et al. 2016, *The Astrophysical Journal*, 587, 66
- Bergin, E. A., Goldsmith, P., F., Snell, R., L., et al. 1994, *The Astrophysical Journal*, 431, 674
- Bézar, B., de Bergh, C., Crisp, D., et al. 1990, *Nature*, 345, 508
- Boger, G., I. and Sternberg, A. 2006, *The Astrophysical Journal*, 645, 314
- Burkhardt, A., M., Herbst, E., Kalenskii, S., V., et al. 2017, *Monthly Notices of the Royal Astronomical Society*, 474, 5068
- Cernicharo, J., Lim, T., Cox, P., et al. 1997, *Astronomy and Astrophysics*, 323, L25
- Clary, D., C., Haider, N., Husain, D., et al. 1994, *The Astrophysical Journal*, 422, 416

- Cleeves, L., I., Öberg, K., I., and Wilner, D., J., et al. 2016, *The Astrophysical Journal*, 832, 110
- Connes, P., Connes, J., Benedict W., S., et al. 1967, *The Astrophysical Journal*, 146, 1230
- Corby, J., F., Jones, P., A., Cunningham, M., R., et al. 2015, *Monthly Notices of the Royal Astronomical Society*, 452, 3969
- Corby, J., F. 2016, UVA Libra
- Corby, J., F., McGuire, B., A., Herbst, E., et al. 2018, *Astronomy and Astrophysics*, 610, A10
- Dunning, T., H. 1989, *J. Chem. Phys.*, 90, 1007
- Dunning, T., H., Peterson, K., A., and Wilson, A., K. 2001, *J. Chem. Phys.*, 114, 9244
- Fernández-Ramos, A., Ellingson, B., A., Meana-Pañeda, R., et al. 2007, *Theor. Chem. Account.* 118, 813.
- Gao, P., Zhang, X., Crisp, D., et al. 2013, *Icarus*, 231, 83
- Garrod, R., T. and Herbst, E. 2006, *Astronomy and Astrophysics*, 457, 927
- Garrod, R., T., Wakelam, V., and Herbst, E. 2007, *Astronomy and Astrophysics*, 467, 1103
- Garrod, R., T. and Pauly, T. 2011, *The Astrophysical Journal*, 735, 15
- Garrod, R., T. 2013, *The Astrophysical Journal*, 765, 60
- Garrod, R., T. and Widicus Weaver, S., L. 2013, *Chem. Rev.*, 113, 8939
- Georgievskii, Y. and Klippenstein, S. 2005, *J. Chem. Phys.*, 122, 194103
- Graedel, T., E., Langer, W., D., and Frerking, M., A. 1982, *The Astrophysical Journal Supplement Series*, 48, 321
- Gratier, P., Majumdar, L., Ohishi, M., et al. 2016, *The Astrophysical Journal Supplement Series*, 225, 25
- Greaves, J., S. and Nyman, L., A. 1996, *Astronomy and Astrophysics*, 305, 950
- Güver, T. and Özel, F. 2009, *Monthly Notices of the Royal Astronomical Society*, 400, 2050

- Hansen, J., E. and Hovenier, J., W. 1974, *J. Atmos. Sci.*, 31, 1137
- Harada, N., Herbst, E., and Wakelam, V. 2010, *The Astrophysical Journal*, 721, 1570
- Harada, N., Thompson, T., A., and Herbst, E. 2013, *The Astrophysical Journal*, 765, 108
- Harada, N., Nishimura, Y., Watanabe, Y., et al. 2019, *The Astrophysical Journal*, 871, 238
- Hasegawa, T., I., Herbst, E. and Leung, C., M. 1992, *The Astrophysical Journal Supplement Series*, 82, 167
- Hasegawa, T., I. and Herbst, E. 1993, *Monthly Notices of the Royal Astronomical Society*, 261, 83
- Hasegawa, T., I. and Herbst, E. 1993, 263, 589
- Herbst, E. and Klemperer, W. 1973, *The Astrophysical Journal*, 185, 505
- Herbst, E. and van Dishoeck, E., F. 2009, *Annual Review of Astronomy and Astrophysics*, 47, 427
- Herbst, E. and Woon, D., E. 1997, *The Astrophysical Journal*, 489, 109
- Hersant, F., Wakelam, V., Dutrey, A., et al. 2009, *Astronomy and Astrophysics*, 493, L49
- Hincelin, U., Wakelam, V., Hersant, F., et al. 2011, *Astronomy and Astrophysics*, 530, 6
- Hincelin, U., Wakelam, V., Commerçon, B., et al. 2013, *The Astrophysical Journal*, 775, 11
- Hincelin, U., Commerçon, B., Wakelam, V., et al. 2016, *The Astrophysical Journal*, 822, 31
- Hougen, J., T. and Oka, T. 2005, *Science*, 310, 1913
- Immer, K., Kauffmann, J., Pillai, T., et al. 2016, *Astronomy and Astrophysics*, 595, A94
- Indriolo, N. and McCall, B., J. 2012, *The Astrophysical Journal*, 745, 17
- Indriolo, N., Neufeld, D., A., Gerin, M., et al. 2015, *The Astrophysical Journal*, 800, 26

- Irvine, W., M., Goldsmith, P., F., Hjalmarson, Å. 1987, in: Hollenbach D.J., Thronson H.A. Jr. (eds.) Proceedings of the Symposium on Interstellar Processes. Reidel, Dordrecht, p. 561
- Jenkins, E., B. 2009, *The Astrophysical Journal*, 700, 1299
- Jensen, P. and Bunker, P., R. 1979, Academic Press Inc. New York, NY
- Kaifu, N., Ohishi, M., Kawaguchi, K., et al. 2004, *Publications of the Astronomical Society of Japan*, 56, 69
- Kendall, R., A., Dunning, T., H., and Harrison, R., J. 1992, *J. Chem. Phys.*, 86, 6797
- Krasnopolsky, V. 2007, *Icarus*, 19, 25
- Krasnopolsky, V. 2012, *Icarus*, 218, 230
- Le Bourlot, J., Pineau des Forets, G., Roueff, E., et al. 1993, *The Astrophysical Journal Letters*, 416, L87
- Le Bourlot, J., Pineau des Forets, G., Roueff, E., et al. 1995, *Astronomy and Astrophysics*, 302, 870
- Le Gal, R., Herbst, E., Dufour, G., et al. 2017, *Astronomy and Astrophysics*, 605, 88
- Le Petit, F., Nehmé, C., Le Bourlot, J., et al. 2006, *The Astrophysical Journal Supplement Series*, 164, 506L
- Lepp, S., and Dalgarno, A. 1996, *Astronomy and Astrophysics*, 306, L21
- Levshakov, S., A., Kozlov, M., G., and Reimers, D. 2011, *The Astrophysical Journal*, 738, 26
- Lis, D., C. and Goldsmith, P., F. 1990, *The Astrophysical Journal*, 356, 195
- Liszt, H. and Lucas, R. 2000, *Astronomy and Astrophysics*, 358, 1069
- Liszt, H., Sonnentrucker, P., Cordiner, M., et al. 2012, *The Astrophysical Journal Letters*, 753, L28
- Liu, S., Y. and Snyder, L., E. 1999, *The Astrophysical Journal*, 523, 683
- Loison, J., C., Wakelam, V., Hickson, K., M., et al. 2014, *Monthly Notices of the Royal Astronomical Society*, 437, 930
- Loomis, R., A. 2013, *The Astrophysical Journal Letters*, 765, 7

- Maffucci D., M., Wenger, T., V., Le Gal, R., et al. 2018, *The Astrophysical Journal*, 868, 41
- Markwick, A. J., Millar, T., J., and Charnley, S., B. 2000, *The Astrophysical Journal*, 535, 256
- Markwick, A. J., Millar, T., J., H. M., Butner, et al. 2005, *The Astrophysical Journal*, 627, L117
- Millar, T., J. and Herbst E. 1990, *Astronomy and Astrophysics*, 231, 466
- Mills, F., P. and Allen, M. 2007, *Planet. Space Sci.*, 55, 1729
- Minissale, M., Dulieu, F., Cazaux, S., et al. 2016, *Astronomy and Astrophysics*, 585, 24
- Morton, D., C. 1974, *The Astrophysical Journal Letters*, 193, 35
- McGuire, B., A., Carroll, P., B., Loomis, R., A., et al. 2013, *The Astrophysical Journal*, 774, 56
- Müller, H., S., P. and Woon, D., E. 2013, *J. Phys. Chem. A*, 117, 13868
- Murrells, T., P. 1987, *J. Chem. Soc, Faraday Trans. 2*, 84(1), 85
- Na, C., Y., Esposito, L., W., Skinner, T., E., et al. 1990, *J. Geophys. Res.*, 95, 7485
- Neill, J., L., Muckle, M., T., Zaleski, D., P., et al. 2012, 755, 153
- Neill, J., L., Begin, E., A., Lis, D., C., et al. 2014, *The Astrophysical Journal*, 789, 29
- Neufeld, D., A., Wolfire, M., G., and Shilke, P. 2005, *The Astrophysical Journal*, 628, 260
- Öberg, K., I., Guzmán, V., V., Furuya, K., et al. 2015, *Nature*, 520, 198
- Ohishi, M. and Kaifu, N. 1998, *FaDi*, 109, 205
- Prasad S., S. and Huntress, W., T. 1982, *The Astrophysical Journal* 260, 590
- Pratap, P., Dickens, J., E., Snell, R., L., et al. 1997, *The Astrophysical Journal*, 486, 862
- Purvis, G., D. and Bartlett R., J. 1982, *J. Chem. Phys.*, 76, 1910
- Rabli, D., and Flower, D., R. 2011, *Monthly Notices of the Royal Astronomical Society*, 403, 2033

- Rabli, D., and Flower, D., R. 2011, *Monthly Notices of the Royal Astronomical Society*, 406, 95
- Reid, M., J., Menten, K., M., Brunthaler, A., et al. 2014, *The Astrophysical Journal*, 783, 130
- Ruaud, M., Loison, J., C., Hickson, K., M., et al. 2015, *Monthly Notices of the Royal Astronomical Society*, 447, 4004
- Ruaud, M., Wakelam, V., and Hersant, F. 2016, *Monthly Notices of the Royal Astronomical Society*, 459, 3756
- Ruffle, D., p., Hartquist, T., W., Caselli, P., et al. 1999, *Monthly Notices of the Royal Astronomical Society*, 306, 691
- Sander, S., P., Golden, D., M., Kurylo, M., J., et al. 2006, *Chemical Kinetics and Photochemical Data for Use in Atmospheric Studies. Evaluation 15*. JPL Publication 06-2. Pasadena, CA
- Sandor, B., J. and Clancy, R. 2013, *DPS Meeting #45*, id.202.02
- Semenov, D., Hersant, F., Wakelam, V., et al. 2010, *Astronomy and Astrophysics*, 522, 12
- Schmiedeke, A., Schilke, P., Möller, Th., et al. 2016, *Astronomy and Astrophysics*, 588, A143
- Smith, I., W., Herbst, E., and Chang, Q. 2004, *Monthly Notices of the Royal Astronomical Society*, 350, 323
- Snow, T., P. and McCall, B., J. 2006, *Annual Review of Astronomy and Astrophysics*, 44, 367
- Soma, T., Sakai, M., Watanabe, Y., et al. 2015, *The Astrophysical Journal*, 802, 74
- Stewart, A., I., Anderson, D., E., Esposito, L., W., et al. 1979, *Science*, 203, 777
- Sutton, E., C., and Herbst, E. 1988, *The Astrophysical Journal*, 333, 359
- Taniguchi, K., Herbst, E., Paola, C. 2019, *The Astrophysical Journal*, 881, 57
- Thiel, V., Belloche, A., Menten, K., M., et al. 2017, *Astronomy and Astrophysics*, 605, L6
- Thiel, V., Belloche, A., Menten, K., M., et al. 2019, *Astronomy and Astrophysics*, 623, A68

- Tieftrunk, A., Pineau des Forets, G., Schilke, P., et al. 1994, *Astronomy and Astrophysics*, 289, 579
- Tiné, S., Lepp, S., Gredel, R., et al. 1997, *The Astrophysical Journal*, 481, 282
- van Dishoeck, E., F., and Black, J., H. 1986, *The Astrophysical Journal Supplement Series*, 62, 109
- Vasyunin, A., I., and Herbst, E. 2013, *The Astrophysical Journal*, 769, 34
- Vidal, T., Loison, J., C., Yassin Jaziri, A., et al. 2017, *Monthly Notices of the Royal Astronomical Society*, 469, 435
- Viti, S. 2017, *Astronomy and Astrophysics*, 607, 118
- Watts, J., D., Gauss, J., Bartlett, R., J. 1993, *J. Chem. Phys.*, 98, 8718
- Wakelam, V. and Herbst, E. 2006, *Astronomy and Astrophysics*, 451, 551
- Wakelam, V. and Herbst, E. 2008, *The Astrophysical Journal*, 680, 371
- Wakelam, V., Herbst, E., Le Bourlot, J., et al. 2010, *The Astrophysical Journal*, 517, 21
- Wakelam, V., Herbst, E., Loison, J., C., et al. 2012, *The Astrophysical Journal Supplement Series*, 199, 10
- Wakelam, V., Loison, J., C., Herbst, E., et al. 2015, *The Astrophysical Journal Supplement Series*, 217, 7
- Wakelam, V., Chapillon, E., Dutrey, A., et al. 2019, *Monthly Notices of the Royal Astronomical Society*, 484, 1563
- Whiteoak, J., B., and Gardner, F., F. 1979, *Monthly Notices of the Royal Astronomical Society*, 188, 445
- Wirström, E., S., Bergman, P., Black, J., H., et al. 2010, *Astronomy and Astrophysics*, 522, A19
- Woon, D., E. and Dunning, T., H. 1993, *J. Chem. Phys.*, 98, 1358
- Woon, D., E. and Herbst, E. 1996, *The Astrophysical Journal*, 465, 795
- Woon, D., E., and Herbst, E. 2009, *The Astrophysical Journal Supplement Series*, 185, 273
- Zaleski, D., P., Seifert, N. A., Steber, A., L., et al. 2013, *The Astrophysical Journal Letters*, 765, 6
- Zhang, X., Liang, M., C., Mills, F., P., et al. 2012, *Icarus*, 217, 714